OUTLIER AWARENESS AND MITIGATION FOR GNSS/INS INTEGRATED SYSTEMS FOR POST-PROCESSING APPLICATIONS

YIHAN ZHONG

PhD

The Hong Kong Polytechnic University

2026

The Hong Kong Polytechnic University

Department of Aeronautical and Aviation Engineering

Outlier Awareness and Mitigation for GNSS/INS Integrated Systems for Post-processing Applications

Yihan Zhong

A thesis submitted in partial fulfilment of the requirements for the degree of Doctor of Philosophy

July 2025

CERTIFICATE OF ORIGINALITY

I hereby declare that this thesis is my own work and that, to the best of my knowledge and belief, it reproduces no material previously published or written, nor material that has been accepted for the award of any other degree or diploma, except where due acknowledgement has been made in the text.

___________________________(Signed)

Yihan Zhong (Name of student)

ABSTRACT

The Global Navigation Satellite System (GNSS) post-processing applications hold a pivotal position in modern smart cities. Post-processing GNSS technology has been widely applied in applications such as structural health monitoring and pedestrian motion health in open-sky environments. However, GNSS signals are affected by multipath effects and non-line-of-sight received signals under high-rise buildings in urban areas. The positioning results can differ greatly from the real position, and the positioning error can reach tens of meters. To explore better positioning results in urban environments, in this thesis, we develop and publish several new methods to improve the positioning accuracy of navigation using low-cost sensors in urban areas. First, we integrate GNSS and inertial measurement unit (IMU) in smartphones to provide more robust results for smoothing pedestrian trajectories in urban areas. The post-processing results show that our proposed method can provide better positioning results by integrating the IMU from smartphones into the novel factor graph optimization (FGO) framework. Secondly, urban areas typically have pre-built 2D maps where vehicles and pedestrians are navigated within designated lanes or walkways. Considering this constraint, we proposed a GNSS/Map integration with FGO to achieve better positioning performance for urban navigation with multi-epoch map constraints. Crucially, it was observed that the precision of the map serves as a limiting factor for the reliability of the positioning outcome. However, the accuracy of the map can also be affected by the absolute positioning provided by the mapping algorithm. Existing mapping algorithms require extremely expensive hardware, and to overcome the high-cost drawback, we propose an algorithm based on a Micro-Electro-Mechanical Systems (MEMS) IMU and a low-cost GNSS receiver to provide reliable lane-level localization

in urban canyons. This cost-effective GNSS/IMU post-processing system achieves an accuracy of approximately 20 centimeters in normal urban environments when utilizing the FGO framework. Furthermore, it demonstrates an approximate 50% improvement in accuracy within highly obstructed urban areas. All the methods have been tested in real-world data. In the future, we want to further investigate collaborative positioning based on multi-source messages, to achieve high-accuracy urban positioning.

PUBLICATIONS

JOURNAL PAPERS

1. **Zhong, Y**., Hu, R., Bai, X., Li, X., Hsu, L.T. and Wen, W., (2024). Enhancing GNSS Positioning Accuracy for Road Monitoring Systems: A Factor Graph Optimization Approach Aided by Geospatial Information. *IEEE Transactions on Instrumentation and* Measurement.
2. Hu, R., Xu, P., **Zhong, Y.** and Wen, W., 2024. pyrtklib: An open-source package for tightly coupled deep learning and GNSS integration for positioning in urban canyons. *IEEE Transactions on Intelligent* Transportation *Systems*.
3. Xu, P., Zhang, G., **Zhong, Y.**, Yang, B., & Hsu, L. T. (2024). A Framework for Graphical GNSS Multipath and NLOS Mitigation. *IEEE Transactions on Intelligent* Transportation *Systems*.
4. Yan, P., **Zhong, Y**., Hsu, L. T. (2024). Principal Gaussian Overbound for Heavy-tailed Error Bounding. *IEEE Transactions on Aerospace and Electronic Systems.*
5. **Zhong, Y**., Wen, W*., & Hsu, L. T. (2024). Trajectory Smoothing Using GNSS/PDR Integration Via Factor Graph Optimization in Urban Canyons. *IEEE Internet of Things Journal*.
6. Chen, P., Guan, W., Huang, F., Zhong, Y., Wen, W., Hsu, L. T., & Lu, P. (2023). ECMD: An Event-Centric Multisensory Driving Dataset for SLAM. *IEEE Transactions on Intelligent Vehicles*.
7. Zhang, L., Ng, H.F., Zhong, Y., Zhang, G. and Hsu, L.T., 2024. GNSS Doppler Velocity Estimation Aided by 3D Mapping Database. *IEEE Transactions on Intelligent Transportation Systems*.
8. Hsu, L. T., Huang, F., Ng, H. F., Zhang, G., Zhong, Y., Bai, X., & Wen, W. (2023). Hong Kong UrbanNav: An open-source multisensory dataset for benchmarking urban navigation algorithms. *NAVIGATION: Journal of the Institute of Navigation*, 70(4).
9. **Zhong, Y.**, Huang, F., Zhang, J., Wen, W., & Hsu, L. T. (2023). Low-cost solid-state LiDAR/inertial-based localization with prior map for autonomous systems in urban scenarios. *IET Intelligent Transport Systems*, 17(3), 474-486

.INTERNATIONAL CONFERENCE PAPERS

1. **Zhong, Y.**, Wen, W., and Hsu, L.T. 2023, September. Towards Accurate Vehicle-to-pedestrian Relative Positioning Aided by Inter-frame and Inter-agent GNSS Measurement Collaboration Using Factor Graph Optimization for Smart Summon. In *Proceedings of the 36th International Technical Meeting of the Satellite Division of The Institute of Navigation (ION GNSS+ 2023, presented)*.

2. **Zhong, Y.**, Wen, W., Ng, H. F., Bai, X., & Hsu, L. T. (2022, September). Real-time Factor Graph Optimization Aided by Graduated Non-convexity Based Outlier Mitigation for Smartphone Decimeter Challenge. In *Proceedings of the 35th International Technical Meeting of the Satellite Division of The Institute of Navigation (ION GNSS+ 2022, presented)*.

3. Xu, P., Ng, H. F., **Zhong, Y.**, Zhang, G., Wen, W., Yang, B., & Hsu, L. T. (2023, September). Differentiable Factor Graph Optimization with Intelligent Covariance Adaptation for Accurate Smartphone Positioning. In *Proceedings of the 36th International Technical Meeting of the Satellite Division of The Institute of Navigation (ION GNSS+ 2023)*.

4. Ng, H.F., Xu, P., **Zhong, Y.**, Zhang, G., Wen, W. and Hsu, L.T., 2024, September. DGNSS Corrected Pseudorange and Time-Differenced Carrier Phase (TDCP) Measurements using Differentiable Factor Graph Optimization (DFGO). In *Proceedings of the 37th International Technical Meeting of the Satellite Division of The Institute of Navigation (ION GNSS+ 2024)*.

5. F. Huang†, **Zhong, Y**.†, et al., "Roadside GNSS Aided Multi-Sensor Integrated System for Vehicle Positioning in Urban Areas," *2025 IEEE/RSJ International Conference on Intelligent Robots and Systems (IROS)*, Hangzhou, China, 2025, pp. 2734-2741, doi: 10.1109/IROS60139.2025.11246475. (*IEEE/RSJ IROS 2025*, *presented*)

ACKNOWLEDGEMENTS

I would like to express my sincere gratitude to my supervisor, Dr. Weisong Wen, and my co-supervisor, Dr. Li-ta Hsu, for their invaluable guidance, patience, and continuous support throughout my postgraduate studies and research in the field of GNSS.

Dr. Wen guided me into this research area when I had little prior background and provided meticulous and dedicated supervision throughout the years. Under his mentorship, I gradually developed both technical competence and a broader academic perspective. In particular, his insights into robotics research significantly expanded my understanding beyond GNSS and profoundly shaped my research mindset. I am deeply grateful for his trust, encouragement, and long-term guidance. I am also sincerely thankful to Dr. Hsu for sharing his extensive expertise in GNSS research. His guidance, constructive feedback, and insightful discussions have greatly benefited my academic development and contributed substantially to this thesis.

I would like to extend my appreciation to my colleagues and fellow group members, including Dr. Feng Huang, Runzhi Hu, Liyuan Zhang, Dr. Penghui Xu, Dr. Penggao Yan, Dr. Jiachong Chang, Dr. Xikun Liu, Baoshan Song, Dr. Hoi-Fung Ng, Dr. Shiyu Bai, Xiao Xia, Ruijie Xu, Xin Wang, Yuan Li, and Liang Qian for their valuable discussions, collaboration, and support during my research.

Finally, I would like to express my deepest gratitude to my parents, Mr. Ainan Zhong and Ms. Zhou Yun, for their unwavering support, understanding, and encouragement throughout my life and academic journey. Their constant support has been fundamental to the completion of this work.

TABLE OF CONTENTS

1. INTRODUCTION

1.1 Background

As a crucial technological underpinning for modern smart city management [1-3], the Global Navigation Satellite System (GNSS) exhibits notable technical advantages in smart urban monitoring.

One previous study reveals that structural deformation monitoring systems, leveraging Real-Time Kinematic (RTK) technology [4], have been effectively implemented in bridge safety assessment. Engineering practice demonstrates that by deploying GNSS receiver arrays at critical nodes of bridge structures [5-8], in conjunction with observational data from short-baseline reference station networks, continuous three-dimensional displacement monitoring with sub-centimeter level accuracy can be achieved. This provides quantitative data support for the performance evaluation of in-service bridges.

In the context of urban traffic management, the synergistic analysis of multi-source GNSS trajectory data presents novel avenues for optimizing road network operational efficiency. Studies have demonstrated that acquiring location-based service (LBS) data from in-vehicle GNSS terminals and integrating it with spatial-temporal clustering algorithms [8, 9], offers a decision-making framework for the dynamic adjustment of traffic signal timing plans.

Of particular interest is the significant contribution of GNSS positioning technology to urban health promotion [10]. GNSS-based motion trajectory analysis systems integrated into smart devices, when combined with altitude variation and open-source map data, achieve a 60% reduction in overall calorie estimation error compared to alternative smartphone-dependent methodologies [11]. This enhanced accuracy offers a robust data foundation for the formulation of personalized exercise regimens.

Furthermore, deformation monitoring networks utilizing multi-frequency GNSS have achieved significant advancements in the domain of road maintenance [12-14]. By deploying centimeter-precision GNSS monitoring terminals, transportation authorities are enabled to establish comprehensive databases documenting road pavement distress evolution. The application of this technology holds the potential to expedite maintenance response times and reduce overall road maintenance expenditures.

Besides, the generation of high-precision maps relies on the precise location data provided by the GNSS [15-19], which is crucial for applications such as autonomous driving, smart cities, and robotics. Through GNSS technologies like RTK and Precise Point Positioning (PPP), centimeter-level positioning accuracy can be achieved, providing high-resolution spatial information for roads, geographic features, and other environmental elements. When combined with multi-sensor fusion techniques (such as LiDAR, cameras, and Inertial Measurement Units (IMU), GNSS data enhances the detail and accuracy of maps, enabling them to better reflect the real world.

Current methods for generating high-precision maps heavily depend on costly combined positioning technologies using GNSS and Inertial Navigation Systems (INS) [15, 16, 18]. This reliance results in a significant cost burden. The high procurement and maintenance expenses of high-precision GNSS equipment and systems, coupled with performance limitations in complex environments, make frequent map updates difficult. Furthermore, to ensure the real-time nature and accuracy of map data, continuous and substantial investment in sensor calibration, data acquisition, and processing is required [20]. This poses a significant challenge for regions or businesses with limited resources. This high cost not only restricts the large-scale application of high-precision maps but also impacts their update frequency and coverage, consequently hindering their widespread application and development in fields like autonomous driving and smart cities.

It is widely acknowledged that GNSS technology experiences diminished performance within urban environments primarily due to the presence of tall buildings. These structures constitute obstructions that give rise to both the multipath effect and non-line-of-sight (NLOS) signal reception [21]. The occurrence of multipath and NLOS conditions has the potential to introduce substantial inaccuracies in GNSS-derived positioning solutions. In response to this challenge, a considerable body of research has been dedicated to devising methodologies aimed at alleviating the detrimental consequences of multipath and NLOS phenomena [22-25]. More recently, GNSS positioning techniques leveraging Factor Graph Optimization (FGO) [26] have demonstrated enhanced resilience to potential anomalies, notably NLOS and multipath signals. This improved robustness is attributed to the utilization of measurement redundancy across multiple preceding epochs through the factor graph paradigm. In contrast, conventional Extended Kalman Filtering (EKF) based approaches [27, 28] predominantly utilize information from only two successive epochs concurrently. A robust algorithmic model, developed by the Chemnitz University of Technology research group [29-31], has also employed FGO to effectively reduce the impact of outlier measurements on GNSS positioning accuracy. In their work, only the raw GNSS pseudorange measurements were exploited. Their investigations, however, were limited to the exclusive use of raw GNSS pseudorange measurements. Expanding upon this, our team has made publicly available a comprehensive FGO-based GNSS positioning framework [32] that incorporates both raw pseudorange and Doppler measurements from GNSS. The findings indicate a notable improvement in positioning performance compared to the established EKF-based method implemented in the widely recognized RTKLIB software [33]. Notably, recent advancements in FGO-based GNSS positioning by Dr. Suzuki [34] achieved top-tier accuracy in the Google Smartphone Challenge during both the ION GNSS+ 2021 [34] and ION GNSS+ 2022 [35] conferences. Dr. Suzuki's work integrates switchable constraints [36] in conjunction with batch optimization to ensure trajectory smoothness. The studies collectively suggest that FGO possesses the capability to mitigate the adverse effects of GNSS outliers by capitalizing on the increased redundancy of measurements derived from historical data. Nevertheless, it is important to acknowledge that FGO-based standalone GNSS positioning continues to face limitations, particularly within deep urban canyons, where positioning errors can still reach up to 20 meters in highly urbanized settings [32].

1.2 Research Objectives and Contribution

The primary objective of this research is to provide higher precision positioning solutions for users requiring post-processing positioning in urban environments. In this study, we will focus on exploring the following three key issues：

1.2.1 Enhancing Post-processing Positioning Accuracy for Pedestrians in Urban Environments Using MEMS IMU

In urban environments, pedestrians often walk close to buildings, which significantly degrades the satellite geometry precision (Dilution of Precision, DOP). Furthermore, GNSS measurements are replete with multipath and NLOS signals, while direct signals are extremely limited. This severely reduces the accuracy of GNSS positioning. In certain areas, there may even be an issue of insufficient redundancy in GNSS observations, leading to insufficient measurement redundancy for producing a stable solution in some segments., which is unacceptable for pedestrian positioning. To address this problem, we integrate smartphone MEMS-IMU/PDR with GNSS by adding PDR-derived relative-motion factors to connect consecutive epochs when GNSS measurements are degraded. Simultaneously, we introduce a factor graph optimization framework to maximize the utilization of historical redundancy information, providing more reliable relative constraints for continuous pedestrian positioning in urban environments. This method not only significantly improves pedestrian positioning accuracy but also lays a solid foundation for its application in fields such as sports and health.

1.2.2 Enhancing Post-processing Positioning Accuracy for Vehicles in Urban Environments Using Map Data

Unlike pedestrians, vehicles typically travel in the center of roads, thus benefiting from better satellite geometry precision, which is regarded as a lower DOP value. However, multipath effects and NLOS reception still exist in GNSS measurements, causing vehicle positioning to deviate from lane lines, which seriously affects post-event analysis based on vehicle positioning. To address this challenge, we propose a solution based on existing map information: by providing a confidence domain for vehicles (i.e., vehicles must travel on lane lines) and incorporating lane line information and GNSS measurements into a factor graph optimization framework, the optimal solution for vehicle position can be achieved. This research method fully utilizes redundant GNSS information and lane line constraints, significantly smoothing vehicle trajectories in urban environments and providing higher precision positioning results for urban road monitoring.

1.2.3 Enhancing Post-processing Positioning Accuracy of Low-Cost Vehicle Sensors in Urban Environments Using RTK Technology and IMU Pre-integration Technology

Although combining urban maps for positioning has been proven feasible, the rapid changes in urban environments (such as the emergence of new buildings in a short period) require mapping data to be continuously updated. The key to map updates lies in ensuring absolute positioning accuracy. Traditional mapping methods rely on high-precision INS and survey-grade GNSS receiving antennas to obtain Ground Truth (GT) positions, but their high cost (tens of thousands of US dollars) limits the possibility of widespread application. To address this issue, We use a MEMS IMU and a u-blox F9P receiver with a patch antenna to evaluate whether decimeter-level post-processing accuracy can be achieved. This method provides a new possibility for low-cost production of high-precision maps while maintaining high cost-effectiveness.

The in-depth exploration and resolution of the above three key issues will provide more precise positioning solutions for pedestrians, vehicles, and other users in urban environments, thereby promoting the application and development of related fields such as sports and health, road monitoring, and map updates.

1.3 Thesis Outline

The remainder of the thesis is structured as follows:

Chapter 2 systematically reviews Global Navigation Satellite System (GNSS) positioning technology in urban environments. Firstly, the key role of positioning technology in urban navigation is discussed, followed by an analysis of the research progress in enhancing the positioning accuracy of mobile phones based on pedestrian dead reckoning (PDR) technology, with a focus on the effectiveness of GNSS and PDR fusion algorithms. The current research status of incorporating map information into GNSS algorithms to improve positioning performance in urban environments is then examined. Finally, the importance of accurate absolute positioning in high-precision map production and its need for adaptability in urban environments is demonstrated, the limitations of existing algorithms are pointed out, and the research progress of GNSS and inertial measurement unit (IMU) fusion algorithms is reviewed.

Chapter 3 introduces a meticulously designed, tightly coupled integration system that synergistically combines Global Navigation Satellite System (GNSS) and Pedestrian Dead Reckoning (PDR) methodologies, leveraging Factor Graph Optimization (FGO). This system is specifically proposed for smartphone-based pedestrian navigation within challenging urban canyon environments. Specifically, the relative motion estimation capabilities inherent in PDR serve to enhance the system's resilience against potential GNSS outliers, thereby mitigating their adverse effects. Conversely, the incorporation of raw GNSS measurements provides a crucial mechanism for correcting the cumulative drift, a common limitation associated with PDR systems operating in isolation. Crucially, the utilization of global optimization, facilitated by the FGO framework, is strategically exploited to effectively mitigate the inherent limitations of both positioning modalities. This novel approach aims to yield a highly accurate and continuous trajectory, a feature of paramount importance for pedestrian navigation applications.

Chapter 4 employs an FGO-based approach to tightly couple the road information from Google Earth with raw GNSS measurements to solve for the receiver's position. To the best of the authors' knowledge, this research is the first research that combines map information with GNSS raw measurements using FGO.

In Chapter 4, a methodology predicated on Factor Graph Optimization (FGO) is implemented to achieve a robust integration of road network information, sourced from Google Earth, and raw Global Navigation Satellite System (GNSS) measurements. The objective of this integration is to accurately resolve the position of the receiver. To the best of the authors' knowledge, this study represents the first instance in the extant literature wherein map information is combined with raw GNSS measurements within an FGO framework..

Chapter 6 concludes the above parts and discusses potential future work.

2. LITERATURE REVIEW

Urban canyons represent a particularly crucial environment from an economic standpoint, simultaneously presenting a heightened demand for precise pedestrian navigation capabilities [37, 38]. Currently, GNSS receivers maintain their essential role in open environments, providing dependable global positioning services for users within urban settings. However, it is well-documented that GNSS performance is significantly degraded in urban areas due to the prevalence of tall buildings. These vertical obstructions frequently induce both the multipath effect and NLOS signal reception conditions [21].

2.1 Sports Health and Positioning: GNSS/PDR-Based Pedestrian Positioning Approach

Walking is an essential part of daily human life in urban settings and a fundamental activity for focusing on personal physical fitness and health [39]. Research indicates that integrating GNSS trajectory data can significantly improve the accuracy of energy expenditure estimation for athletes or pedestrians [11, 40]. Therefore, achieving high-precision pedestrian positioning technology in urban environments is of significant value for scientifically assessing daily physical activity levels and health management.

Despite the aforementioned advantages of GNSS in open areas, it is crucial to acknowledge that multipath effects and NLOS signal reception can still introduce considerable errors into GNSS positioning solutions. In response to this inherent limitation, a substantial body of scholarly work has focused on developing methodologies designed to mitigate the adverse consequences of both multipath and NLOS phenomena [22-25]. Recently, FGO-based GNSS positioning techniques [26] have emerged as a promising avenue, demonstrating enhanced resilience to potential outlier measurements, particularly those arising from NLOS and multipath interference. This improved robustness is largely attributed to the FGO approach's capacity to leverage redundant measurements across multiple historical epochs within the factor graph framework. This contrasts with conventional EKF-based methods [27, 28]. which typically rely on information from primarily two consecutive epochs processed concurrently. Furthermore, a robust algorithmic model, developed by the research group at Chemnitz University of Technology [29-31], has successfully employed FGO to reduce the impact of outlier measurements on GNSS positioning accuracy. It is important to note that their research primarily utilized raw GNSS pseudorange measurements. Expanding upon this foundation, our team has made publicly available a generalized FGO-based GNSS positioning framework [32]. The result shows that the positioning performance was improved compared to the conventional EKF-based approach from the famous RTKLIB [33]. Interestingly, the recent FGO-based GNSS positioning developed by Dr. Suzuki [34] obtained the best accuracy in the Google Smartphone Challenge in ION GNSS+ 2021 [34] and ION GNSS+ 2022 [35]. His research used switchable constraints [36] together with batch optimization to maintain the trajectory smoothness. The above research showed that the FGO can mitigate the GNSS outlier's adverse effect by using the increased measurement redundancy from historical information. However, the FGO-based GNSS standalone positioning is still challenged in deep urban canyons, resulting in 20 meters of positioning error in highly urbanized areas [32]. Utilizing the IMU in the positioning system is one of the possible ways to assist deep urban positioning [41-43]. With the widespread adoption of MEMS-IMU technology in smartphones, there is a growing idealization of its application as a supplement to urban navigation systems. The pedestrian dead reckoning (PDR) [44-49] exploits the context of pedestrian navigation, which can provide the relative position between two consecutive states by detecting the walking steps. Building on this foundation, Chen et al. [42] utilized electromyography signals for pedestrian navigation, significantly enhancing stride detection and distance estimation accuracy. Kang and Han [50] developed a novel system, which utilizes smartphone inertial sensors for indoor localization. Their system is distinctive for its ability to mitigate the effects of magnetic disturbances and sensor noise, common issues in urban indoor environments. Kuang et al. [51] developed a MEMS-IMU-based robust PDR algorithm tailored for smartphones, addressing diverse carrying positions and step detection failures. [42, 50, 52] proposed a novel zero-velocity detection algorithm for PDR, eliminating the dependence on predetermined thresholds and enhancing adaptability across varied walking patterns. Combining the MEMS sensor information in the mobile phone as well as the GNSS information may complement the smartphone positioning accuracy in urban areas [53, 54]. PDR demonstrates its role in urban navigation and a detailed review of PDR can be found at [55]. To enhance pedestrian navigation in urban areas, the integration of GNSS and PDR technologies has been developed [43, 56-58]. Angrisano et al. [59] enhanced urban pedestrian localization by fusing PDR with GNSS data using a loosely coupled integration architecture, showcasing improvements in scenarios with compromised GNSS signals. To address the limitations inherent in GNSS-denied environments, an integrated GNSS/PDR methodology has been developed, incorporating techniques such as peak detection, sliding window analysis, and zero-crossing methods for pedestrian step detection [56]. Furthermore, a real-time Kalman Filter-based GNSS/PDR positioning approach has been put forth, employing a multi-rate filter to mitigate instances of GNSS signal unavailability [43]. In addition, certain researchers have leveraged EKF-based GNSS/PDR integration to enhance the positioning accuracy of smartphone-based navigation systems operating in environments susceptible to multipath effects [57]. However, these EKF-based GNSS/PDR integration strategies do not adequately leverage the measurement redundancy available from historical data. This limitation prompts us to consider a novel inquiry: to what extent can PDR augment existing FGO-based GNSS positioning methodologies, as illustrated in Fig. 2.1. Interestingly, one study [58] has explored a loosely coupled GNSS/PDR integration framework utilizing FGO, wherein PDR is directly integrated with the position solution derived from GNSS. Regrettably, this loosely coupled integration within the FGO framework may not fully capitalize on the inherent temporal correlation present in raw GNSS pseudorange measurements, and, importantly, the high-accuracy Doppler measurements were not effectively utilized [28].

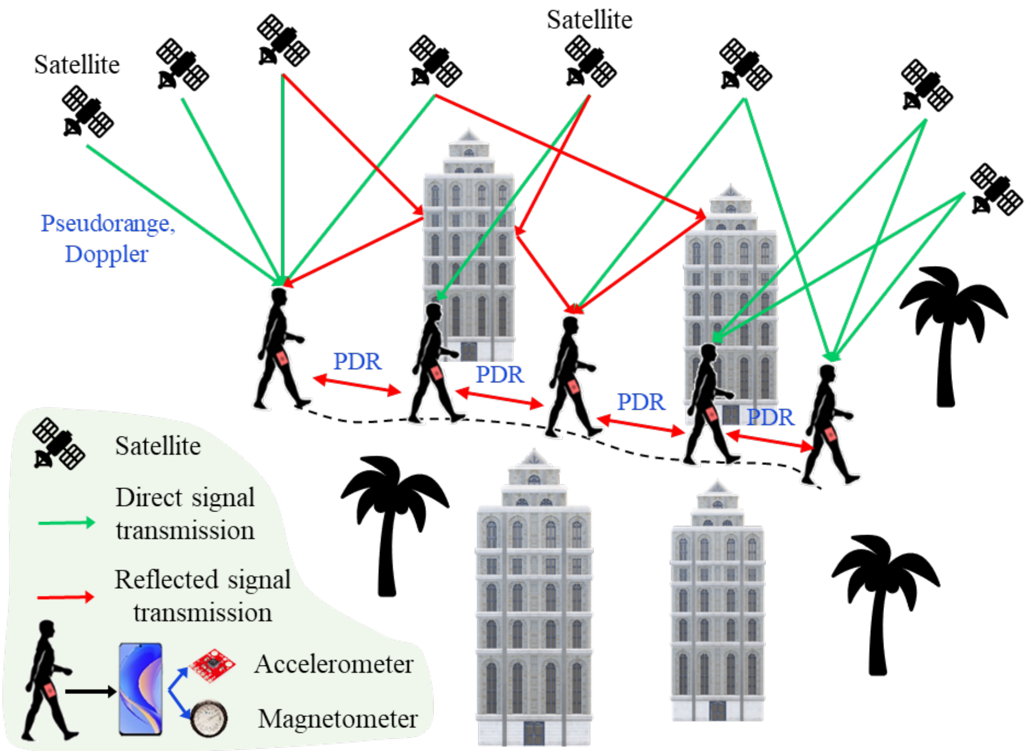

Fig. 2.1. Illustration of the challenges of pedestrian navigation in urban canyons with numerous GNSS signal reflections.

2.2 Enhancing GNSS Positioning Accuracy For Road Monitoring Systems: A Factor Graph Optimization Approach Aided By Geospatial Information

In contemporary urban environments, the escalating volume of traffic in conjunction with the rising fiscal burden of road and associated infrastructure upkeep underscores the critical importance of robust urban road health monitoring. Such monitoring is paramount for upholding traffic safety standards and ensuring the long-term viability of urban infrastructure [60, 61]. Concurrent with the expansion of the global urban population and heightened economic activity, road infrastructure is subjected to progressively intensified strain. This necessitates regular evaluation and maintenance protocols to uphold seamless traffic circulation and safeguard public well-being [62]. A notable disparity in road maintenance expenditures is discernible across various nations. For instance, in 2021, the United States government committed a considerable sum of $110 billion towards the rehabilitation and modernization of roads and bridges [63], while in mainland China, expenditure on road maintenance reached at least $15.1 billion [64]. Since 2015, the United Kingdom government has made substantial investments in road repair initiatives, encompassing a dedicated fund of $373 million allocated from fiscal year 2015/16 to 2020/21. Furthermore, in 2018, the UK government injected a one-time allocation of $529 million into highway maintenance initiatives across all road management divisions in England [65]. In Hong Kong, official data from the Highways Department indicates that road reconstruction expenditures over the preceding triennium have surpassed $89 million [66]. These considerable financial commitments underscore the exigency for efficacious and streamlined strategies for the identification and remediation of road deterioration, with sophisticated road monitoring systems emerging as a promising technological solution [67].

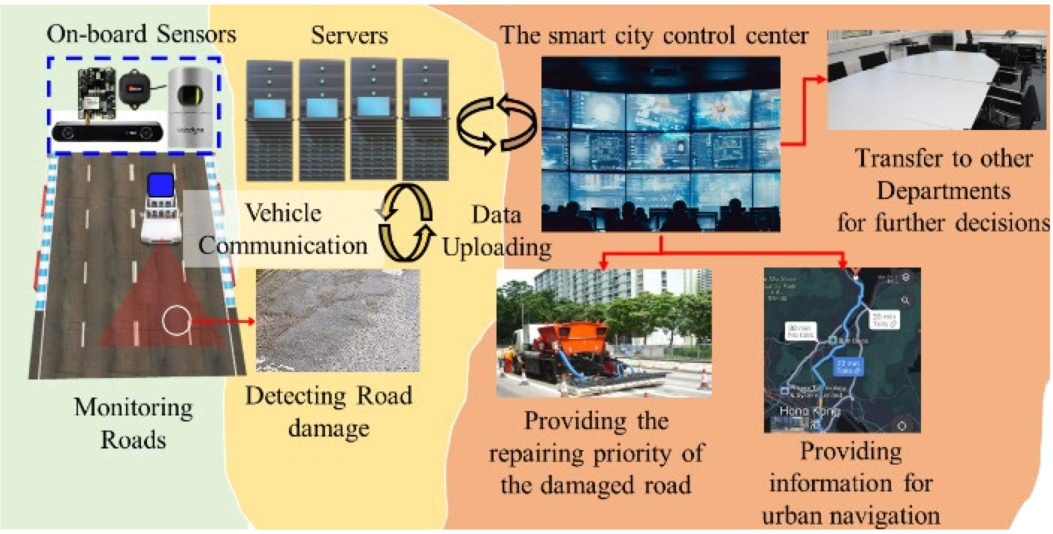

Fig. 2.2. Illustration of the road monitoring system in the context of smart cities.

Road monitoring assumes a position of paramount importance in contemporary smart city frameworks, as visually represented in Figure 2.2. A prototypical system architecture typically commences with a sensor-equipped vehicle, incorporating modalities such as cameras [68, 69] and Light Detection and Ranging (LiDAR) [70, 71] systems, specifically designed for comprehensive environmental perception. Furthermore, these systems are generally furnished with a Global Navigation Satellite System (GNSS) receiver, enabling the acquisition of the vehicle's positional data within a global coordinate framework. Upon the detection of road surface anomalies or damage, the integrated onboard computer system autonomously generates a report detailing the location of the identified defect and subsequently transmits this information to a remote cloud-based server. The central control facility then undertakes the processing of the received data, generating actionable intelligence and recommendations for relevant decision-making bodies, thereby informing prioritization of road repair interventions. Concurrently, map service providers, exemplified by platforms such as Google Maps, can disseminate real-time alerts to inform users of road conditions.

The operational efficacy of these sophisticated road monitoring systems is intrinsically linked to the attainment of high-fidelity global positioning coordinates, a task that presents considerable challenges within dense urban settings. As visually depicted in Figure 2.3, the prevalence of tall buildings in urban environments restricts the number of satellites within the line of sight, thereby precipitating multipath effects and non-line-of-sight (NLOS) signal receptions [72]. Moreover, the observable satellite constellation is often geometrically aligned along the street orientation, leading to an elevated DOP value, which serves as an indicator of suboptimal satellite geometry and consequently reduced positioning accuracy. Therefore, the contribution of robust GNSS positioning technology is unequivocally critical for effective urban road monitoring initiatives.

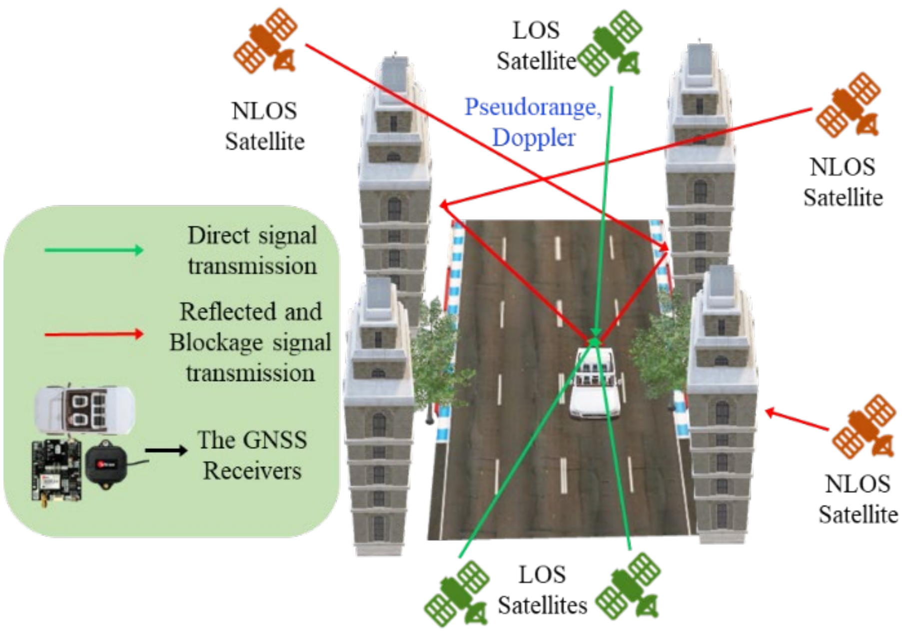

Fig. 2.3. The problem of urban GNSS positioning.

There is a burgeoning scholarly interest in the advancement of innovative Global Navigation Satellite System GNSS positioning technologies specifically engineered to exhibit resilience within the intricate and challenging conditions characteristic of urban environments. High-precision GNSS positioning technology possesses the potential to optimize resource allocation, thereby facilitating continuous enhancements in urban road infrastructure management and development. RTK positioning, a high-accuracy GNSS technique, leverages carrier phase measurements to achieve positioning accuracies at the centimeter level [4, 73]. However, the application of measurement differencing techniques within urban canyons is frequently impeded by signal obstruction, multipath propagation phenomena, and the prerequisite for a geographically proximate reference station to compute precise differential corrections.

Recent research endeavors have explored the integration of three-dimensional (3D) building models to augment GNSS positioning performance in urban canyon scenarios [74-76]. Notwithstanding the considerable computational burden imposed by 3D building models, the incorporation of computationally less demanding data streams into GNSS positioning systems is generally considered a more pragmatic strategy for urban road monitoring applications. Consequently, the majority of vehicular navigation systems incorporate map-matching algorithms [77]. One study has proposed a map-assisted GNSS positioning system specifically designed to improve positioning accuracy, taking into account diverse road typologies, such as extended straight roads, finite straight road segments, and curvilinear roads [78]. This body of research investigates two distinct use cases: aeronautical and vehicular applications [79]. In the context of vehicular positioning, a digital road map is employed to align the vehicle's traversed path with the road network, resulting in positional refinements down to meter-level accuracy. Another investigation integrated map information through the utilization of a priori approximate road network maps to construct a hybrid metric and topological road map representation [80]. The map information was subsequently fused to derive more robust localization outcomes. Furthermore, a separate study implemented map data as an ancillary measurement within the filtering process, specifically employing it as a heading observation within a Kalman filter architecture

[81]. OpenStreetMap (OSM), a collaborative, open-source project, provides freely accessible and modifiable map data, encompassing comprehensive road network datasets [82]. OSM was first integrated into autonomous robot navigation in 2010 [83]. It is noteworthy that this particular study did not utilize the OSM path for positioning purposes, instead exclusively leveraging building information contained within OSM datasets. Moreover, OSM exhibits potential for enhancing location tracking performance in indoor-outdoor transition scenarios for pedestrian mobility [84]. By effectively harnessing OSM data, GNSS positioning within urban canyons can be significantly improved without necessitating the deployment of expensive 3D building models or computationally intensive processing methodologies. In the contemporary landscape, Google Earth Engine (GEE) has gained widespread adoption as a valuable geological data resource [85]. Its utility extends across a diverse range of applications, including the estimation of daily blue ice fractions [86], monitoring temperate forest degradation [87], and assessing pasturelands and livestock dynamics [88]. GE can also aid in optimizing the path planning algorithm for minimal cost [89]. The accuracy and reliability of information provided within GEE have been rigorously validated [90, 91], thereby establishing it as a viable tool for high-precision GNSS positioning applications. With the increasing prevalence of openly accessible data resources, the utilization of road information extracted from GEE has become progressively more feasible.

Complementary to the integration of supplementary aided information, the algorithmic framework employed for processing measurements within the system is of paramount importance for urban navigation applications. Weighted Least Squares (WLS) and Kalman Filter methodologies [92-95] represent conventional approaches to GNSS positioning that have been extensively implemented across a wide spectrum of applications [96]. WLS is a linear estimation technique that operates by minimizing the residuals between observed measurements and predicted values, whereas KF constitutes a recursive filtering algorithm capable of estimating the state of a GNSS receiver based on noisy raw measurements. However, both of these methods exhibit inherent limitations, particularly when deployed in urban canyon environments. WLS demonstrates sensitivity to outlier data points and may yield biased estimations in the presence of multipath and NLOS signal reception conditions. Conversely, KF relies on linear approximations and assumptions of Gaussian noise distribution, which may not adequately represent the complex signal propagation environment characteristic of urban canyons [97]. EKF is an extension of the KF that addresses the nonlinearity issue by linearizing the system model around the current state estimate [73]. While EKF has been applied to enhance GNSS positioning in urban canyons and exhibits greater robustness compared to KF, its performance remains constrained by its recursive formulation and its reliance on Gaussian noise assumptions. To address these limitations and advance the state-of-the-art in GNSS positioning frameworks, Factor Graph Optimization (FGO) has garnered significant research attention recently, demonstrably showcasing its capabilities in the 2021 and 2022 Google Smartphone Decimeter Challenge (GSDC) [34, 35]. The winning methodology in these challenges employed time-differenced carrier phase measurements within an FGO framework to achieve accurate relative positioning between successive epochs. The FGO approach, by integrating all available historical information and circumventing the first-order Markov chain assumption, demonstrates enhanced performance and outperforms EKF methodologies [28]. By effectively incorporating comprehensive road information, FGO can globally consider vehicle motion constraints, thereby yielding more consistent positioning solutions throughout the trajectory. The incorporation of road information as an aiding source can contribute to mitigating the accumulation of positioning errors and improve overall positioning accuracy. Within urban canyon environments, multipath effects and NLOS signal reception frequently degrade GNSS signal quality, thereby reducing positioning precision. Through the integration of map information, these challenges can be more effectively addressed, and positioning outcomes can be rendered more robust to these detrimental influencing factors.

Conversely, it is crucial to acknowledge that misaligned map matching in map-aided GNSS positioning can introduce substantial positioning errors, a critical issue extensively documented in numerous review articles [98-100]. Early iterations of map-matching techniques predominantly employed rudimentary algorithms, such as point-to-curve proximity algorithms [101]. However, these initial strategies are notably susceptible to inaccuracies stemming from suboptimal GNSS solutions. In response to these limitations, significant advancements have been made in map-matching methodologies. For instance, one research group has pioneered a comprehensive approach that integrates data from multiple sensor modalities, including GNSS, Dead Reckoning (DR), and Digital Elevation Models (DEM). This sophisticated method employs the Extended Kalman Filter (EKF) to derive a more accurate estimation of the vehicle's position, which is subsequently utilized for enhanced map-matching processes [102]. Significantly, this approach facilitates the incorporation of supplementary attributes derived from road links and nodes, enabling a more refined and accurate mapping solution. Despite these notable advancements, it remains imperative to recognize that the persistent challenge of elevated GNSS noise levels within urban environments continues to pose a significant impediment to the effectiveness of these methodologies, potentially leading to erroneous map-matching results. In addition to errors introduced by GNSS outlier measurements, trajectory anomalies originating from prior map-matching operations can also contribute to inaccurate state estimation [98].

2.3 Factor Graph Optimized GNSS/IMU Integration for Low-Cost, High-Accuracy HD Map Generation in Urban Canyons

High-precision localization is paramount for generating high-definition (HD) maps, which are critical for advancing autonomous driving and smart city applications [16-18]. Centimeter-level accuracy is often required for HD mapping, necessitating sophisticated GNSS and INS integrated solutions. However, commercially available GNSS/INS systems that meet these accuracy demands typically come with a high price tag, often exceeding US$30,000 [103]. This significant cost barrier substantially impedes the widespread deployment of HD mapping and related location-based services, particularly in resource-constrained environments and large-scale urban areas.

While various methods have been explored for low cost GNSS/INS integration, Kalman filter-based approaches have been particularly prominent in addressing these challenges [104-108]. Falco *et al.* conducted comprehensive experiments to evaluate the performance of a GNSS/INS integrated system in challenging urban environments [104], including parking lots, narrow streets, and tree-lined avenues. By incorporating vehicle non-holonomic (NHC) constraints and addressing MEMS IMU temperature compensation, they demonstrated that their tightly coupled algorithm significantly improved vehicle position estimation accuracy compared to commercial loosely coupled systems. Subsequently, Wen *et al.* explored the FGO framework in their research, also validated the effectiveness of tightly coupled GNSS/INS integration using a similar system [109]. Furthermore, their study demonstrated that the FGO-based approach achieved higher positioning accuracy than traditional non-iterative, non-sliding window Kalman filter-based systems. However, Wen *et al.*'s work on tightly coupled GNSS/INS integration was preliminary. Their modeling of both GNSS and INS was relatively coarse, and they did not adequately consider GNSS RTK techniques or IMU pre-integration. Consequently, the positioning accuracy achieved was still insufficient for high-definition mapping applications. To improve INS modeling, a research team from Wuhan University investigated Earth rotation compensation [110]. By comparing loosely coupled integration results of GNSS with various grades of IMUs, they highlighted the degradation effect of Earth rotation on inertial navigation systems. Recently, Gici-lib [111] from Shanghai Jiao Tong University further advanced the field by tightly integrating GNSS RTK and IMU pre-integration within an FGO framework. Their approach achieved state-of-the-art (SOTA) accuracy on the publicly available UrbanNav dataset. Nevertheless, the Gici-Lib didn't incorporate SOTA methods for GNSS outliers mitigation. Therefore, investigating how to mitigate GNSS outliers in urban is crucial for such a tightly-coupled system. In urban positioning, while building a well-performing GNSS/INS integrated system is essential, properly accounting for the influence of GNSS outliers is of paramount importance for achieving accurate absolute positioning.

Various approaches exist for quality control in GNSS measurements. Generally, tightly coupled GNSS/INS systems, whether based on KF [57, 95, 112, 113] or FGO [34, 114-116], inherently possess a certain degree of outlier rejection capability. This is attributed to the fact that these methods typically leverage redundant information from GNSS, IMU, and potentially other sensors. Through the data fusion mechanism of state estimators, they exhibit a capacity to smooth out and discern measurements that are inconsistent or significantly biased. However, to further enhance positioning accuracy and robustness in complex environments, extensive research has been conducted on outlier detection and rejection methods, even upon the foundation of KF and FGO [117-122].

For instance, addressing potential gross errors and anomalies in GNSS observations, some research efforts have focused on introducing more stringent statistical tests and consistency checking mechanisms. Hsu et al. proposed an outlier rejection method based on residual consistency checks [123]. Two approaches were proposed for outlier exclusion: greedy search and exhaustive search. In the greedy search FDE method, biased satellites are iteratively excluded, one by one, until the test statistic satisfies the chi-squared threshold. This approach is computationally efficient and suitable for real-time implementation. In contrast, the exhaustive search FDE method tests all possible subsets of satellites to identify the most consistent satellite constellation. Exhaustive search can be considered theoretically optimal in terms of consistency checking. Beyond statistical test-based methods, some studies have explored outlier rejection strategies based on model prediction and multiple hypothesis testing [124, 125]. These methods typically establish more refined error models or construct multiple hypothetical models running in parallel, identifying and rejecting anomalous GNSS measurements by comparing model predictions with actual observations.

Despite their ability to improve outlier rejection to some extent, the aforementioned methods often exhibit certain limitations. On one hand, sophisticated statistical tests or model prediction methods can increase computational burden and reduce system real-time performance. On the other hand, over-reliance on residual statistical properties or model assumptions may, in complex and variable environments, make it difficult to accurately distinguish genuine phenomena from outliers, potentially leading to the erroneous removal of valid information or the failure to detect true outliers [126].

To more effectively utilize the quality information of GNSS signals, another significant category of outlier mitigation methods focuses on adaptive weighting of GNSS measurements. Among these, machine learning-based methods have garnered increasing attention in recent years [127-130]. These methods typically utilize large amounts of GNSS data to train machine learning models that predict GNSS signal quality and dynamically adjust measurement weights based on the predicted quality. For example, in paper [129], the deep learning model can be employed to learn the mapping relationships between features such as GNSS signal Carrier-to-Noise ratio (C/N0), Doppler shift, pseudorange residuals, and positioning errors, thereby achieving adaptive weight assignment.

Among various weighting strategies, C/N0-based and elevation angle-based approaches remain popular due to their simplicity and practical effectiveness [131, 132]. The C/N0 value directly reflects the strength and quality of GNSS signals; a higher value generally indicates better signal quality and less susceptibility to noise and interference. Therefore, the weights of GNSS measurements can be directly set according to their C/N0 values. For instance, signals with higher C/N0 values can be assigned larger weights, and vice versa. This method is simple to implement, computationally inexpensive, and effectively reduces the negative impact of low-quality GNSS signals on positioning results, demonstrating good performance in practical applications.

3. TRAJECTORY SMOOTHING USING GNSS/PDR INTEGRATION VIA FACTOR GRAPH OPTIMIZATION

To effectively exploit the complementariness of the recently developed FGO-based GNSS positioning and the PDR, this study investigates a tightly coupled FGO-based GNSS/PDR integration system for smartphone-based pedestrian navigation in urban canyons. On the one hand, the relative motion estimation of PDR can help resist the potential GNSS outliers. On the other hand, the GNSS raw measurements can help to correct the accumulated drift from PDR. More importantly, the global optimization from the FGO is exploited to relax the potential of both positioning sources to obtain an accurate and smooth trajectory which is of great significance for pedestrian navigation applications. Given the context of pedestrian navigation, this study proposes a smoothness-driven motion model (SMM) that can effectively capture the dynamics of the pedestrian. The main contributions of this study are summarized as follows:

(1) As an extension of our previous work in [32, 133], a tightly coupled FGO-based GNSS/PDR integrated positioning method is proposed in this study. Specifically, Doppler and pseudorange measurements are tightly-coupled (TC) to connect the state set of two consecutive epochs in the factor graph. The relative motion is derived from the PDR based on the raw measurements from IMU which helps to establish an additional relative connection between the consecutive states.

(2) To effectively capture the dynamics of pedestrian navigation, this study proposes a smoothness-driven motion model based on the context of pedestrian navigation with a small acceleration for trajectory smoothing which could also help to resist the potential GNSS outliers in GNSS standalone positioning.

(3) In this study, the SMM and PDR factors' validity are progressively verified using a challenging dataset collected in the Hong Kong urban canyon with detailed

discussion. Moreover, we compare the conventional EKF-based methods with several existing methods to our proposed GNSS/PDR integration method, again showing the proposed method's effectiveness.

To the best of the author’s knowledge, this work is the first research on the tightly-coupled GNSS pseudorange and Doppler measurements with PDR in FGO for a smoother trajectory of pedestrian navigation. The remainder of this study is arranged as follows. Firstly, Section II overviews the proposed GNSS/PDR integration method. Then, the details of the PDR model and modeling of GNSS measurements were proposed in Section III. Furthermore, two experimental results in urban canyons will be interpreted in Section IV. section V presented discussions. Finally, Section VI presented conclusions and further work about the proposed GNSS/PDR integration.

3.1 Methodology

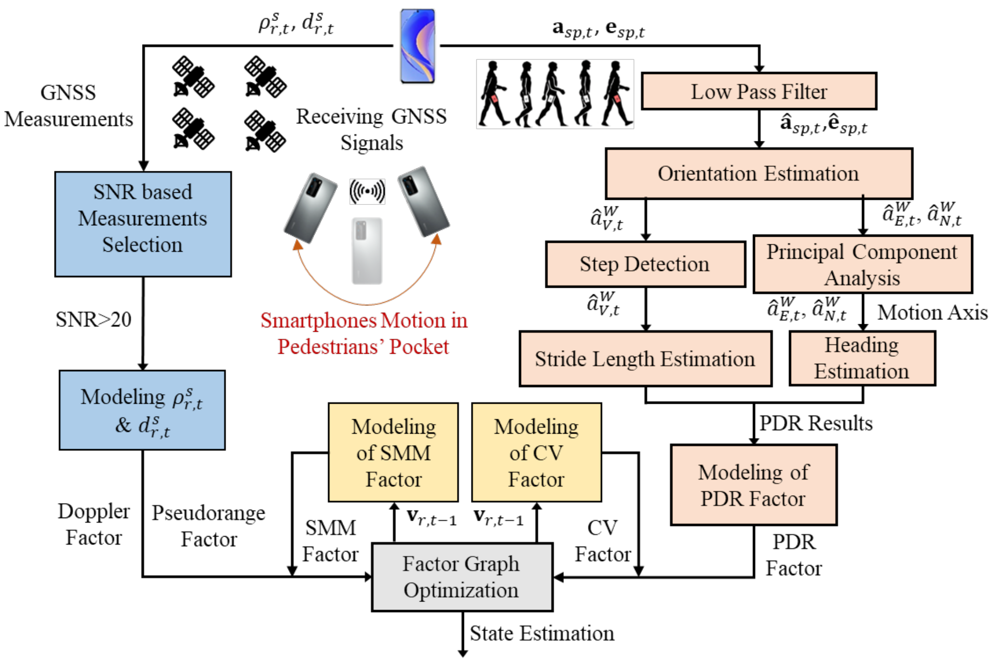

Fig. 3.1. Overview of the proposed FGO-based GNSS/PDR integration method.

The proposed FGO-based GNSS PDR positioning method is shown on Fig. 3.1. positioning methodology is graphically depicted in Figure 3.1. The input data to this integrated GNSS/PDR system is categorized into two distinct components. The first component encompasses raw pseudorange and Doppler measurements acquired from the Global Navigation Satellite System (GNSS) receiver embedded within the smartphone. Specifically, satellite signals are filtered out if their elevation angles (ELE) are below 15 degrees or their signal-to-noise ratios (SNR) are less than 20. The second input component comprises measurements from the magnetometer and accelerometer. The resultant output of the proposed GNSS/PDR integration process is the state estimation of the smartphone. The GNSS/PDR positioning solution is subsequently derived by resolving the formulated factor graph. This factor graph is constructed to incorporate a tightly-coupled configuration of the Doppler factor, the pseudorange factor, the relative motion estimation derived from PDR, a smoothness-driven motion model, and a constant velocity (CV) factor within the optimization framework.

Table 3.1. Symbols and their description in this study

Symbol	*Description*
r	The GNSS receiver
s	The index of the satellite
$\rho_{r,t}^{s}$	The pseudorange measurement received from a satellite s at a given epoch t.
$d_{r,t}^{s}$	The Doppler measurement received from satellite s at a given epoch t
$\mathbf{p}_{t}^{s}$	The position of the satellite s at a given epoch t. $\mathbf{p}_{t}^{s} = (p_{t,x}^{s}, p_{t,y}^{s}, p_{t,z}^{s})^{\mathrm{T}}$
$\mathbf{v}_{t}^{s}$	The velocity of the satellite s at a given epoch t. $\mathbf{v}_{t}^{s} = (v_{t,x}^{s}, v_{t,y}^{s}, v_{t,z}^{s})^{\mathrm{T}}$
$\mathbf{p}_{r,t}$	The position of the GNSS receiver at a given epoch t. $\mathbf{p}_{r,t} = (p_{r,t,x}, p_{r,t,y}, p_{r,t,z})^{\mathrm{T}}$
$\mathbf{v}_{r,t}$	The velocity of the GNSS receiver at a given epoch t. $\mathbf{v}_{r,t} = (v_{r,t,x}, v_{r,t,y}, v_{r,t,z})^{\mathrm{T}}$
$\mathbf{a}_{sp,t}$	The raw measurement from the smartphone accelerometers at a given epoch t. $\mathbf{a}_{sp,t} = (a_{sp,t,x}, a_{sp,t,y}, a_{sp,t,z})^{\mathrm{T}}$
$\mathbf{e}_{sp,t}$	The raw measurement from the smartphone magnetometers at a given epoch t. $\mathbf{e}_{sp,t} = (\mathrm{e}_{sp,t,x}, e_{sp,t,y}, e_{sp,t,z})^{\mathrm{T}}$
$\hat{\mathbf{a}}_{sp.t}$	The filtered measurement from the accelerometers at a given epoch t in the global coordinate system. $\hat{\mathbf{a}}_{sp.t} = (\hat{a}_{sp,t,x}, \hat{a}_{sp,t,y}, \hat{a}_{sp,t,z})^{\mathrm{T}}$
$\hat{\mathbf{e}}_{sp,t}$	The filtered measurement from the magnetometers at a given epoch t in the global coordinate system. $\hat{\mathbf{e}}_{sp,t} = (\hat{e}_{sp,t,x}, \hat{e}_{sp,t,y}, \hat{e}_{sp,t,z})^{\mathrm{T}}$
$\delta_{r,t}$	The clock bias of the GNSS receiver at a given epoch t
$\delta_{r,t}^{s}$	The satellite clock bias at a given epoch t

To make the presentation of this study clear, the notations in Table 3.1 are defined and are followed by the rest of this study. Matrices are denoted in uppercase with bold letters. Vectors are denoted in lowercase with bold letters. Variable scalars are denoted as lowercase italic letters. Constant scalars are denoted as lowercase letters. Note that this study expresses the GNSS receiver's state, the output from PDR, and the position of satellites in the earth-centered, earth-fixed (ECEF) frame.

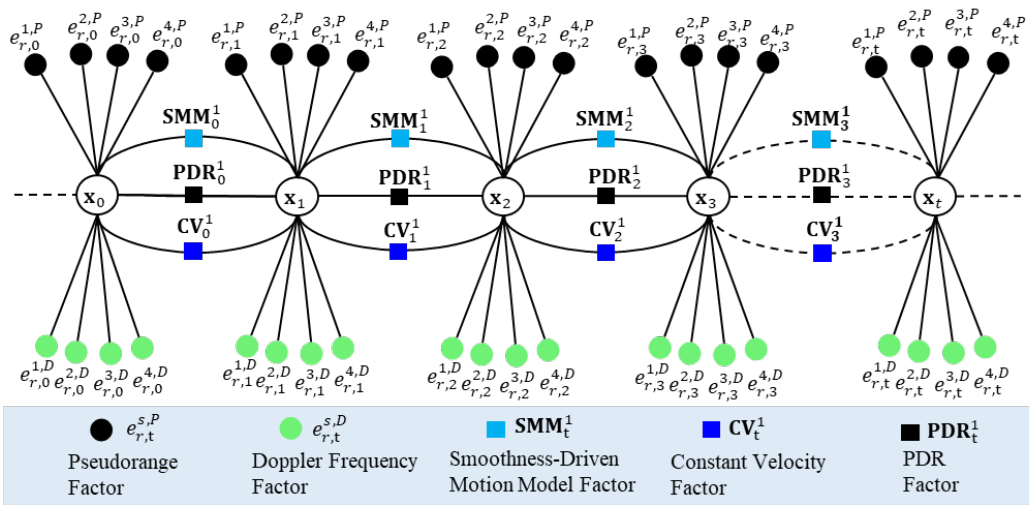

Fig. 3.2. The factor graph for proposed GNSS/PDR integration.

Fig.3.2 shows the factor graph of the proposed GNSS/PDR integrated positioning structure. The smartphone-level GNSS receiver state set is represented as follows:

$$\boldsymbol{\chi} = \left[\mathbf{x}_{\mathrm{r},1}, \mathbf{x}_{\mathrm{r},2}, \ldots, \mathbf{x}_{r,t}, \ldots, \mathbf{x}_{r,k}\right] \tag{3.1}$$

$$\boldsymbol{\chi} = \left[\mathbf{x}_{\mathrm{r},1}, \mathbf{x}_{\mathrm{r},2}, \ldots, \mathbf{x}_{r,t}, \ldots, \mathbf{x}_{r,k}\right] \tag{3.2}$$

Where the variable $\boldsymbol{\chi}$ denotes the state set of the smartphone-level GNSS receiver ranging from the first epoch to the current epoch k. $\mathbf{x}_{r,t}$ denotes the single state of the smartphone at epoch t which involves: the position ($\mathbf{p}_{r,t}$), velocity ($\mathbf{v}_{r,t}$), receiver clock bias ($\delta_{r,t}$) and clock drift ($\dot{\delta}_{r,t}$).

The CV and PDR factors are utilized to connect each state. To smooth the user's trajectories, the SMM factor is also included in our proposed factor graph, which is going to be elaborated in sub-section E. For a concise illustration, we briefly present the observation model and error function of pseudorange measurements which follow our previous work [32] but an explicit derivation of the Doppler factor which is tightly coupled in the system.

3.1.1 Pseudorange Measurement Modeling

The observation model for GNSS pseudorange measurement from a given satellite s is represented as follows:

$$\rho_{r,t}^{s} = h_{r,t}^{s}\left(\mathbf{p}_{r,t}, \mathbf{p}_{t}^{s}, \delta_{r,t}\right) + \omega_{r,t}^{s} \tag{3.3}$$

with $h_{r,t}^{s}\left(\mathbf{p}_{r,t}, \mathbf{p}_{t}^{s}, \delta_{r,t}\right) = ||\mathbf{p}_{t}^{s} - \mathbf{p}_{r,t}|| + \delta_{r,t}$

where the variable $\omega_{r,t}^{s}$ stands for the noise associated with the $\rho_{r,t}^{s}$. We can derive the error function ($\mathbf{e}_{r,t}^{s,P}$) in proposed GNSS/PDR integration for a given satellite measurement $\rho_{r,t}^{s}$ as follows:

$$\left|\left|\mathbf{e}_{r,t}^{s,P}\right|\right|_{\boldsymbol{\Sigma}_{r,t}^{s}}^{2} = \left|\left|\rho_{r,t}^{s} - h_{r,t}^{s}\left(\mathbf{p}_{r,t}, \mathbf{p}_{t}^{s}, \delta_{r,t}\right)\right|\right|_{\boldsymbol{\Sigma}_{r,t}^{s}}^{2} \tag{3.4}$$

where $\boldsymbol{\Sigma}_{r,t}^{s}$ denotes the covariance matrix, calculated following the GO-GPS work [134] with the satellite SNR and ELE.

3.1.2 Tightly-coupled Doppler frequency factor

The range rate measurement vector ($\mathbf{y}_{r,t}^{d}$) at an epoch t is expressed as follows:

$$\mathbf{y}_{r,t}^{d} = \left(\lambda d_{r,t}^{1}, \lambda d_{r,t}^{2}, \lambda d_{r,t}^{3}, \dots\right)^{T} \tag{3.5}$$

The $d_{r,t}^{s}$ and the λ represent the Doppler measurement and the carrier wavelength of the satellite signal, respectively. The expected range rate $rr_{r,t}^{s}$ for satellite s can also be calculated as follows:

$$rr_{r,t}^{s} = \mathbf{e}_{r,t}^{s,LOS}\left(\mathbf{v}_{t}^{s} - \mathbf{v}_{r,t}\right)$$

$$\frac{\omega_{earth}}{c_L}\left(v_{t,y}^{s}p_{r,t,x}+p_{t,y}^{s}v_{r,t,x}-p_{t,x}^{s}v_{r,t,y}-v_{t,x}^{s}p_{r,t,y}\right)+\dot{\delta}_{r,t} \tag{3.6}$$

where the variable ω_{earth} and c_L denote the angular velocity of the earth's rotation [135] and the speed of light, respectively. The variable $\mathbf{e}_{r,t}^{s,LOS}$ denotes the line-of-sight vector connecting the GNSS receiver and the satellite. Furthermore, we can derive the error function ($\mathbf{e}_{r,k}^{s,D}$) of the tightly-coupled Doppler measurement as follows:

$$\left\|\mathbf{e}_{r,k}^{s,D}\right\|_{\boldsymbol{\Sigma}_{r,t}^{D}}^{2}=\left\|\lambda d_{r,t}^{s}-rr_{r,t}^{s}\right\|_{\boldsymbol{\Sigma}_{r,t}^{D}}^{2} \tag{3.7}$$

where $\boldsymbol{\Sigma}_{r,t}^{D}$ denotes the covariance matrix corresponding to the Doppler measurement. And the $\boldsymbol{\Sigma}_{r,t}^{D}$ is also calculated based on the ELE and SNR [134]. Due to the Doppler measurements being less sensitive to the GNSS multipath effects, $\boldsymbol{\Sigma}_{r,t}^{D}$ is multiplied by a fixed coefficient valued at 10, which means larger weightings.

3.1.3 Pedestrian Dead Reckoning Factor Modeling

The PDR factor is modeled by following the work in [133]. In the scenario where the pedestrian placed the smartphone in the pants pocket, the measurements of the gyroscope will be very noisy. Thus, only magnetometers and accelerometers are used in the proposed system. Both the magnetometer and accelerometer in the smartphone output 3D measurements in local coordinates defined by the smartphone and the transformation of local coordinates to the global frame is necessary for global positioning. $\mathbf{a}_{r,t}$ and $\mathbf{e}_{r,t}$ are the accelerometer and the magnetometer measurements, respectively. Both are first used to determine the orientation of the device. The measured acceleration could be converted to the East-north-up frame with the Android API *getRotationMatrix* [136], which aims to match the tri-axis acceleration and detected gravity to get the transformation to the global coordinate. The transformed three acceleration components in the ENU frame are used to determine each step direction and step length. For attenuating the deterioration of dynamic pushes, a low-pass filtering is employed as shown below:

$$\hat{\boldsymbol{a}}_{sp,t} = (1 - \alpha^{acc})\boldsymbol{a}_{sp,t} + \alpha^{acc}(\hat{\boldsymbol{a}}_{sp,t-1}) \tag{3.8}$$

$$\hat{\boldsymbol{e}}_{sp,t} = (1 - \alpha^{mag})\boldsymbol{e}_{sp,t} + \alpha^{mag}(\hat{\boldsymbol{e}}_{sp,t-1}) \tag{3.9}$$

where the $\hat{\mathbf{a}}_{sp,i}$ denotes the filtered measurements of the accelerometer and $\hat{\mathbf{e}}_{sp,i}$ denotes the filtered measurements of the magnetometer. α^{acc} and α^{mag} denote the smoothing factor of the corresponding measurement field. Following the previous settings, we empirically set α^{acc} and α^{mag} as 0.6 and 0.84 [133], respectively. The filtered measurements of acceleration can be calculated. The following part will concisely illustrate the details of the PDR method.

(1) ***The step detection***: Under normal pedestrian walking conditions, the vertical acceleration $\hat{a}_{V,t}^{W}$ reflects a distinct peak and depression for every foot of impact. This feature makes detecting the drop in vertical acceleration as the stride rate feasible. This study empirically utilized a dip threshold at 7.5 m/s to ensure the correct detection.

(2) ***The stride length estimation***: We followed the method proposed by Weinberg [137] based on the peak-to-peak of vertical acceleration to estimate the stride length, and the model is shown as:

$$l = K_w\left(a_{V,max} - a_{V,min}\right)^{0.25} \tag{3.10}$$

where l denotes the estimated stride length, K_w denotes a constant for unit conversion which is empirically set as 0.713. $a_{V,max}$ and $a_{V,min}$ are the maximum and minimum vertical accelerations, respectively.

(3) ***Heading direction estimation***: The employed PDR method estimated the heading direction in two steps. The first step is to perform a principal component analysis on the 2D plane with $\hat{a}_{E,t}^{W}$ and $\hat{a}_{N,t}^{W}$, excluding the vertical direction [45]. Then, they are subjected to the covariance matrix of Eigenvalue decomposition after

smoothing the two sequences using a moving average. The largest eigenvalue result implies the direction estimation in the direction of parallel motion, which is the original forward direction. The second step of the heading direction estimation is to verify whether the original forward direction derived from the PCA is correct. According to [138], vertical and forward accelerations have a time relationship in the same cycle. Usually, the forward acceleration will be followed by a peak immediately after the step detection. By using this property, the forward direction could be decided.

In our approach, the PDR algorithm calculates the user's horizontal displacement within the ENU (East, North, Up) coordinate system. The initial position of the user is manually marked on Google Earth [139]. We then employ a rotation matrix $\mathbf{R}_{enu}^{ecef}$ [140] to transform the PDR results from the ENU system to the ECEF coordinate system. This transformation enables us to obtain the PDR results in three dimensions within the ECEF framework. The relative displacement of the smartphone $\Delta\mathbf{p}_{pdr,t}^{enu}$ could be obtained from PDR results between two consecutive frames under the ENU coordinate system:

$$\Delta\mathbf{p}_{pdr,t}^{enu} = [\Delta x_t^{enu}, \Delta y_t^{enu}, \Delta z_t^{enu}]^T \tag{3.11}$$

$$\Delta\mathbf{p}_{pdr,t}^{enu} = [\Delta x_t^{enu}, \Delta y_t^{enu}, \Delta z_t^{enu}]^T \tag{3.12}$$

where Δx_t^{enu}, Δy_t^{enu} and Δz_t^{enu} are displacement of the receiver which obtained from the PDR in three different directions under the ENU frame. Thus, the relative displacement of the smartphone $\Delta\mathbf{p}_{pdr,t}^{ecef}$ could be obtained by applying the rotation matrix $\mathbf{R}_{enu}^{ecef}$ to $\Delta\mathbf{p}_{pdr,t}^{enu}$:

$$\Delta\mathbf{p}_{pdr,t}^{ecef} = \mathbf{R}_{enu}^{ecef}\Delta\mathbf{p}_{pdr,t}^{enu} \tag{3.13}$$

The difference between two consecutive epochs can be represented as:

$$\Delta\mathbf{p}_{r,t} = \mathbf{p}_{r,t} - \mathbf{p}_{r,t-1} \tag{3.14}$$

Where $\mathbf{p}_{r,t}$ denotes the position of the receiver at the t epoch and the $\mathbf{p}_{r,t-1}$ represents the position of the receiver at the t-1 epoch. Hence, we can get the error function ($\mathbf{e}_{r,t}^{R}$) for a given relative displacement $\Delta\mathbf{p}_{pdr,t}^{ecef}$ as follows:

$$\left\|\mathbf{e}_{r,t}^{R}\right\|_{\mathbf{\Sigma}_{r,t}^{PDR}}^{2} = \left\|\Delta\mathbf{p}_{pdr,t}^{ecef} - \Delta\mathbf{p}_{r,t}\right\|_{\mathbf{\Sigma}_{r,t}^{PDR}}^{2} \tag{3.15}$$

where $\mathbf{\Sigma}_{r,t}^{PDR}$ denotes the covariance matrix. We set it as the fixed value for denoting the performance of the PDR factor, which is experimentally determined as 0.1.

3.1.4 Constant velocity Factor

The constant velocity factor is constructed based on the assumption that the speed of the pedestrian is nearly invariant in walking. In addition to the velocity remaining constant during walking, the acceleration of the receiver should also converge to zero. Hence, we can get the observation model for the smartphone-level GNSS receiver velocity ($\mathbf{v}_{r,t}$) expressed as follows:

$$\mathbf{v}_{r,t} = h_{r,t}^{C}\left(\Delta\mathbf{p}_{r,t}, \mathbf{v}_{r,t}, \mathbf{v}_{r,t+1}\right) + \boldsymbol{\omega}_{r,t}^{C} \tag{3.16}$$

with $h_{r,t}^{C}\left(\Delta\mathbf{p}_{r,t}, \mathbf{v}_{r,t}, \mathbf{v}_{r,t+1}\right) = \begin{bmatrix} \Delta p_{r,t,x}/\Delta t - (v_{r,t,x} + v_{r,t+1,x})/2 \\ \Delta p_{r,t,y}/\Delta t - (v_{r,t,y} + v_{r,t+1,y})/2 \\ \Delta p_{r,t,z}/\Delta t - (v_{r,t,z} + v_{r,t+1,z})/2 \end{bmatrix}$,

where the $\mathbf{v}_{r,t}$ and $\mathbf{v}_{r,t+1}$ denote the velocity at two consecutive epochs with three dimensions in the ECEF frame, respectively. $\Delta p_{r,t,x}$, $\Delta p_{r,t,y}$, $\Delta p_{r,t,z}$ denote the receiver displacement between the t frame and t+1 frame at three dimensions. The variable $\boldsymbol{\omega}_{r,t}^{C}$ denotes the noise associated with constant motion. Hence, the error function ($\mathbf{e}_{r,t}^{C}$) in our proposed GNSS/PDR integration for a given receiver velocity measurement $\mathbf{v}_{r,t}$ could be derived as follows:

$$\left\|\mathbf{e}_{r,t}^{C}\right\|_{\mathbf{\Sigma}_{r,t}^{C}}^{2} = \left\|h_{r,t}^{C}\left((\Delta\mathbf{p}_{r,t}, \mathbf{v}_{r,t}, \mathbf{v}_{r,t+1})\right)\right\|_{\mathbf{\Sigma}_{r,t}^{C}}^{2} \tag{3.17}$$

where $\mathbf{\Sigma}_{r,t}^{C}$ denotes the covariance matrix corresponding to the receiver velocity measurement. This study empirically set $\mathbf{\Sigma}_{r,t}^{C}$ as a fixed value.

3.1.5 Smoothness-driven Motion Model Factor

Given the context of pedestrian navigation, the accelerations caused by smartphone motion tend to be small. To exploit this property which can effectively improve the smoothness of the trajectory, this study proposes a smoothness-driven motion model factor. We can calculate the acceleration of the smartphone-level GNSS receiver $\mathbf{a}_{r,t}$ as follows:

$$\mathbf{a}_{r,t} = \begin{bmatrix} \left(v_{r,t+1,y} - v_{r,t,y}\right)/\Delta t \\ \left(v_{r,t+1,y} - v_{r,t,y}\right)/\Delta t \\ \left(v_{r,t+1,z} - v_{r,t,z}\right)/\Delta t \end{bmatrix} \tag{3.18}$$

Therefore, we can get the observation model for the acceleration ($\mathbf{a}_{r,t}$) expressed as follows:

$$\mathbf{a}_{r,t} = h_{r,t}^{M}\left(0, \mathbf{a}_{r,t}\right) + \boldsymbol{\omega}_{r,t}^{M} \tag{3.19}$$

with $h_{r,t}^{M}\left(0, \mathbf{a}_{r,t}\right) = \begin{bmatrix} 0 - \left(v_{r,t+1,y} - v_{r,t,y}\right)/\Delta t \\ 0 - \left(v_{r,t+1,y} - v_{r,t,y}\right)/\Delta t \\ 0 - \left(v_{r,t+1,z} - v_{r,t,z}\right)/\Delta t \end{bmatrix}$

where the variable $\boldsymbol{\omega}_{r,t}^{M}$ denotes the noise associated with the zero-acceleration model. Hence, we can get the error function ($\mathbf{e}_{r,t}^{M}$) in the proposed GNSS/PDR integration for a given receiver velocity measurement $\mathbf{v}_{r,t}$ as follows:

$$\left|\left|\mathbf{e}_{r,t}^{M}\right|\right|_{\mathbf{\Sigma}_{r,t}^{M}}^{2} = \left|\left|\mathbf{a}_{r,t} - h_{r,t}^{M}\left(0, \mathbf{a}_{r,t}\right)\right|\right|_{\mathbf{\Sigma}_{r,t}^{M}}^{2} \tag{3.20}$$

where $\mathbf{\Sigma}_{r,t}^{M}$ denotes the covariance matrix corresponding to the receiver acceleration measurement. This study also empirically set $\mathbf{\Sigma}_{r,t}^{M}$ as a fixed value.

Therefore, we can formulate the objective function for the GNSS/PDR integration using FGO based on the factors derived above as follows:

$$\boldsymbol{\chi}^{*} = \arg\min_{\boldsymbol{\chi}} \sum_{s,t} \left(\left\| \mathbf{e}_{r,t}^{D} \right\|_{\boldsymbol{\Sigma}_{r,t}^{D}}^{2} + \left\| \mathbf{e}_{r,t}^{s} \right\|_{\boldsymbol{\Sigma}_{r,t}^{s}}^{2} + \left\| \mathbf{e}_{r,t}^{R} \right\|_{\boldsymbol{\Sigma}_{r,t}^{PDR}}^{2} + \left\| \mathbf{e}_{r,t}^{C} \right\|_{\boldsymbol{\Sigma}_{r,t}^{C}}^{2} + \left\| \mathbf{e}_{r,t}^{M} \right\|_{\boldsymbol{\Sigma}_{r,t}^{M}}^{2} \right) \quad (3.21)$$

The variable $\boldsymbol{\chi}^{*}$ denotes the optimal estimation of the state sets. The Ceres Solver [141] is used as a non-linear optimization solver for solving the objective function above. Meanwhile, the Levenberg-Marquardt algorithm [142] is employed in our FGO processes to minimize the cost function iteratively. Additionally, we employed the Huber loss [143] to the optimizer for down-weighting some potential outliers.

3.2 Experiment Setup

To evaluate the efficacy of the proposed FGO-based GNSS/PDR positioning methodology, we acquired four distinct datasets across two challenging scenarios (refer to Figure 3.4 to Figure 3.6). These environments were characterized by a dense presence of buildings and trees, thereby inducing significant multipath effects and NLOS reception. Data collection was performed utilizing a Huawei P40 Pro smartphone, capturing raw GPS and BeiDou measurements [144] at a frequency of 1 Hz and IMU data at 100 Hz. To ensure data consistency, experimental continuity, and controlled comparison conditions, a single hardware platform was used to avoid introducing additional variability caused by sensor differences across devices. For the first and third experiments, pedestrian ground truth trajectories were established using a LiDAR/inertial system. This system comprised a Velodyne HDL-32E LiDAR and an Xsens Mti 10 IMU [103]. The LIO-SAM algorithm was employed for SLAM processing within this system, with the incorporation of a loop-closure constraint to achieve sub-meter level accuracy [145-147]. In the second experiment, conducted within a highly urbanized area characterized by dense vehicular traffic, ground truth data was labeled offline using Google Earth in conjunction with precise time stamps. Subsequently, linear interpolation techniques were applied to ascertain positional information [139]. The proposed framework was executed on a high-performance laptop equipped with an Intel i7-9750K 2.60GHz processor and 32GB of RAM.

Since the satellite geometry in dense urban canyons leads to very unreliable GNSS positioning in the vertical direction, in this study, the horizontal positioning performance will be evaluated in the ENU framework, including the root-mean-square of error (RMSE), the mean error (MEAN), standard deviation (STD), maximum error (MAX).

To verify the effectiveness of our GNSS/PDR integration method in urban canyons step-by-step, we compared the following methods:

(1) **FGO**: GNSS pseudorange/Doppler integration using FGO [32].

(2) **EKF-PDR**: GNSS pseudorange/Doppler/PDR-based extended Kalman filter [148].

(3) **FGO-CV**: CV factor aided GNSS tightly-coupled Doppler/pseudorange integration using FGO.

(4) **FGO-CV-SMM** (1st proposed integration): The CV and SMM factors aided GNSS tightly-coupled Doppler/pseudorange integration using FGO.

(5) **FGO-PDR** (2nd proposed integration): The PDR factor aided GNSS tightly-coupled Doppler/pseudorange integration using FGO.

(6) **FGO-PDR-SMM** (3rd proposed integration): The PDR and SMM factors aided GNSS tightly-coupled Doppler/pseudorange integration using FGO.

(7) **FGO-PDR-CV** (4th proposed integration): The PDR and CV factors aided GNSS tightly-coupled Doppler/pseudorange integration using FGO.

The colors corresponding to each method in the subsequent trajectory and error figures are as follows: The red denotes the FGO. The green color denotes the EKF-PDR. The light pink and pink denote FGO-CV and FGO-CV-SMM, respectively. The light orange and orange denote FGO-PDR and FGO-PDR-SMM, respectively. The light blue and blue colors denote FGO-PDR-CV, and FGO-PDR-CV-SMM, respectively. All the FGO-based methods are post-processing methods. Figure 3.3, 3.4, 3.5 show the experiment environments and the sensors configurations.

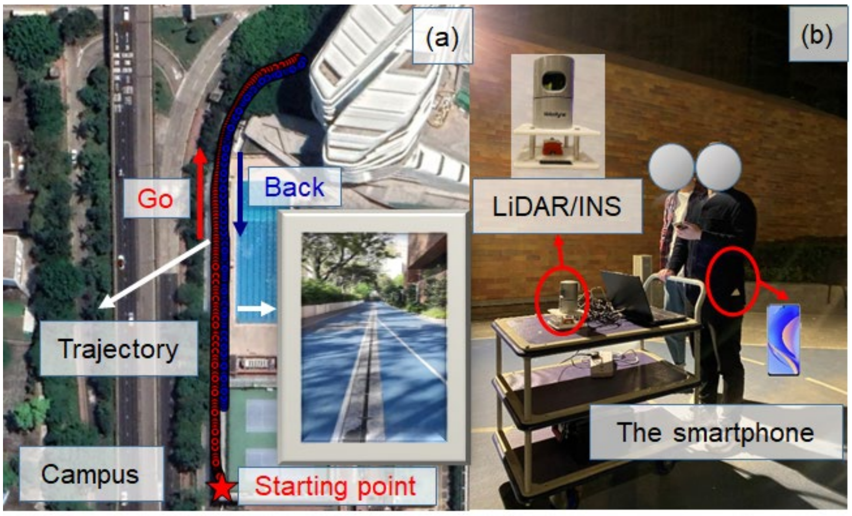

Fig. 3.3. The scenarios and sensor setup of the campus experiment. (a) the evaluated trajectory during the test. (b) the data collection platform with LiDAR/INS-based ground truth system and smartphone for GNSS data collection.

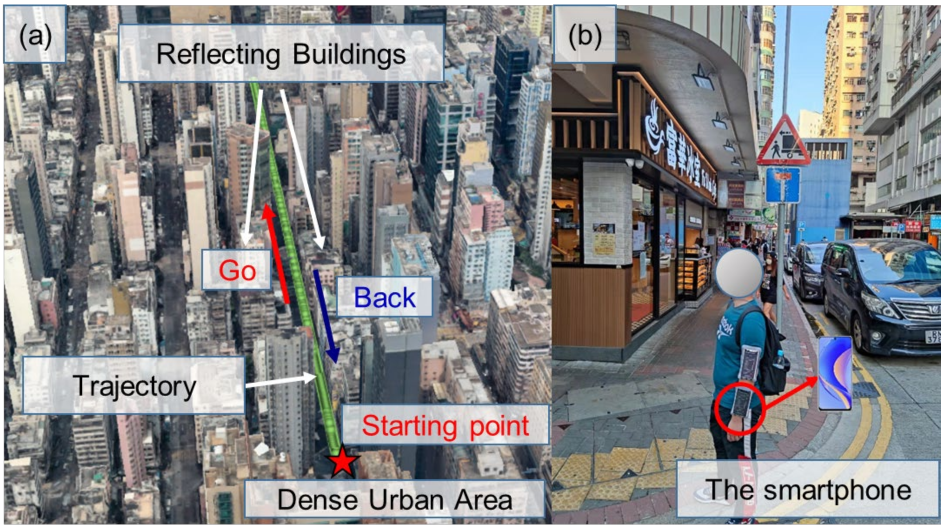

Fig. 3.4. The sensor setup of the dense urban area. (a) the evaluated trajectory in a dense urban canyon. (b) the data collection platform by hand-hold bag with a smartphone for GNSS data collection.

Fig. 3.5. The sensor setup of the mixed scenario. (a) image overview with GT from Google Earth. (b) the GT overview from OpenStreetMap. The LiDAR/INS system is used for generating the GT, HUAWEI P40 Pro smartphone is used for collecting the GNSS and IMU measurements. (c) Street-view of the scenario from Google Earth [85].

The quality of GNSS measurements will be quantified through double-difference (DD) errors. We utilized reference station data from the Hong Kong Geodetic Survey Services [55] to compute the DD pseudorange. This computation was achieved by differencing the reference station data with the receiver data. Subsequently, we combined these results with our position ground truth to ascertain the true DD range. The true DD range was determined by resolving the satellite positions using the ground truth of the reference station. The discrepancy between the DD range and the DD pseudorange was then used to define the error in the double-difference pseudorange.

3.2.1 Experimental Evaluation on Campus

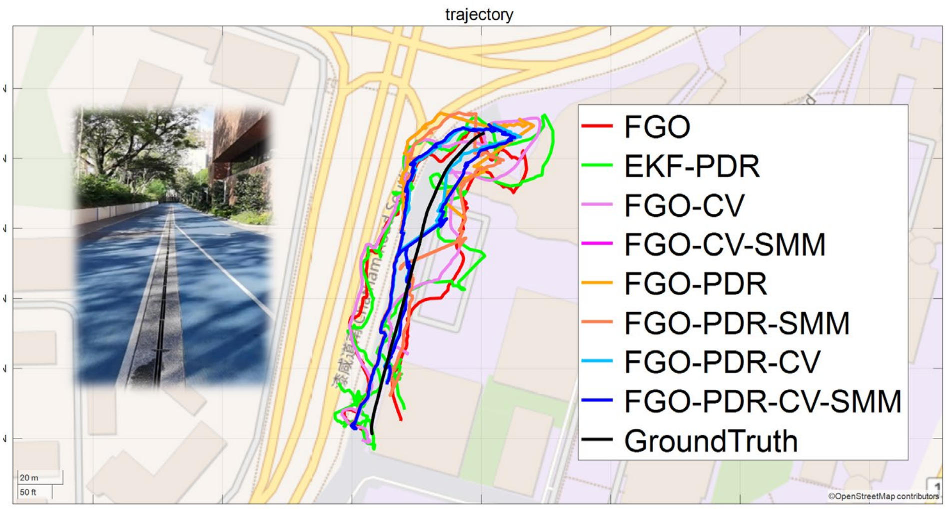

Fig. 3.6. Trajectories of evaluated eight methods on the campus in OpenStreetMap [82].

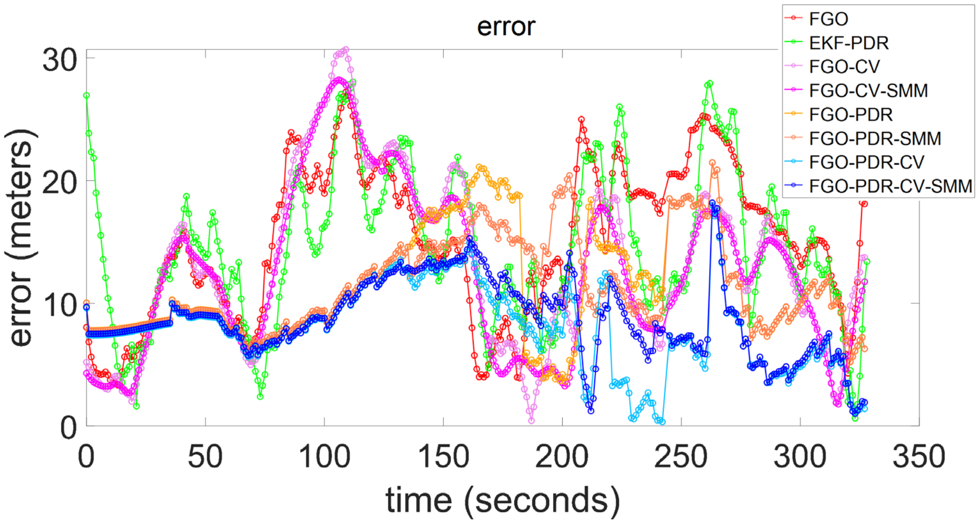

Fig. 3.7. Horizontal positioning errors on the campus.

Figure 3.6 and Figure 3.7 present the two-dimensional (2D) positioning trajectories overlaid on OpenStreetMap [82] and the horizontal errors of all evaluated positioning methods within the campus environment, respectively. Referring to Figure 3.6, it is evident that the trajectory generated by the FGO-PDR-CV-SMM approach (depicted by the blue curve) aligns with the expected characteristics of pedestrian motion. This alignment is achieved through the integration of the PDR factor, CV factor, and SMM factor. Figure 3.7 demonstrates that the incorporation of the PDR factor results in a discernible reduction in positioning error, particularly around epochs 50 and

150. Comprehensive statistical analyses of the horizontal errors are detailed in Table 3.2 and Table 3.3.

Table 3.2. Positioning performance of the listed methods in the campus experiment

All Methods	RMSE (m)	MEAN (m)	STD (m)	MAX (m)
FGO	16.17	14.97	6.13	27.23
EKF-PDR	15.80	14.57	6.13	28.05
FGO-CV	14.85	13.13	6.94	30.69
FGO-CV-SMM	14.17	12.53	6.64	28.22
FGO-PDR	12.17	11.32	4.46	21.47
FGO-PDR-SMM	11.99	11.41	3.69	21.48
FGO-PDR-CV	8.63	7.97	3.33	17.98
FGO-PDR-CV-SMM	9.24	8.71	3.07	18.19

Table 3.3. Horizontal positioning improvements of the listed methods in the campus experiment

Improvements	**RMSE (m)**	**MEAN (m)**	**STD (m)**	**MAX (m)**
FGO	/	/	/	/
EKF-PDR	2.27%	2.65%	0.07%	-3.02%
FGO-CV	8.19%	12.26%	-13.10%	-12.74%
FGO-CV-SMM	12.36%	16.29%	-8.19%	-3.65%
FGO-PDR	24.77%	24.35%	27.31%	21.16%
FGO-PDR-SMM	25.86%	23.77%	39.82%	21.10%
FGO-PDR-CV	46.61%	46.77%	45.69%	33.95%
FGO-PDR-CV-SMM	42.88%	41.78%	49.94%	33.19%

The histogram of DD pseudorange errors in the campus experiment is shown in Figure 3.8. The distribution of errors ranges from about -40 to 20 meters shows that there are errors in the pseudorange of this data that would lead to the degraded positioning performance.

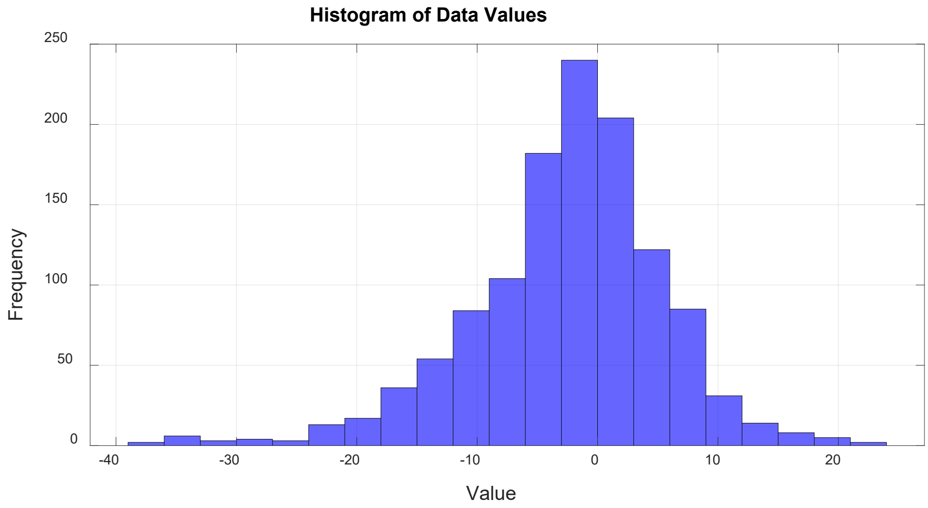

Fig. 3.8. Histogram of the DD pseudorange error in campus experiment.

The standalone FGO approach yields a mean error of 14.97 meters, accompanied by a standard deviation (STD) of 6.13 meters. However, the maximum error observed with FGO reaching 27.23 meters underscores the significant vulnerability of this method to compromised GNSS measurements. The incorporation of the tightly-coupled (TC) Doppler factor in conjunction with the CV factor (FGO-CV) results in a reduction of the mean error to 13.13 meters. This observation indicates that the integration of the CV factor with TC Doppler measurements can effectively enhance positioning performance. Nevertheless, the CV factor, predicated on pedestrian motion models, lacks robust acceleration constraints necessary to effectively mitigate potential GNSS outliers. This deficiency can manifest as a non-smooth trajectory in GNSS-standalone positioning solutions. Upon implementing our proposed SMM factor, the mean error is further reduced to 12.53 meters, demonstrating superior performance compared to FGO-CV. However, the limited availability of satellites and the presence of unhealthy GNSS multipath effects constrain the extent of achievable improvement. A mean error of 11.32 meters, with an STD of 4.46 meters, is attained by incorporating PDR into the TC Doppler FGO framework (FGO-PDR) in lieu of the CV factor. This enhancement, relative to FGO-CV, suggests that the PDR factor offers a more effective constraint on relative position between consecutive epochs. Further augmentation with the SMM factor in FGO-PDR leads to a reduction in the mean error. However, the magnitude of improvement remains limited, potentially due to the inherent error sources within the smartphone accelerometer and magnetometer, which may not perfectly adhere to pedestrian motion patterns. The effectiveness of the CV factor is corroborated by the 7.97-meter mean error achieved with FGO-PDR-CV, which integrates the CV factor. Intriguingly, the STD of error is reduced to 3.07 meters upon applying the SMM factor in FGO-CV-PDR-SMM. However, this configuration exhibits a slightly larger mean error than FGO-CV-PDR. This observation can be attributed to instances of non-zero pedestrian acceleration during ambulation within the experimental scenario.

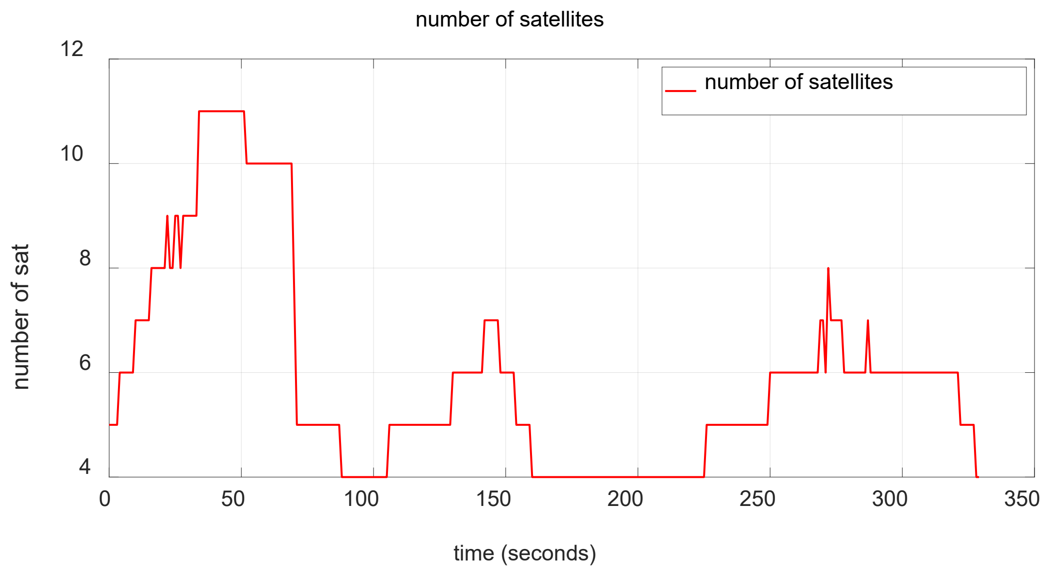

Fig. 3.9. The relationship between the number of satellites with time.

A GNSS/PDR methodology predicated on EKF was also subjected to evaluation. The Root Mean Square Error (RMSE) for this approach was determined to be 15.80 meters, marginally exceeding that of FGO-CV and FGO-CV-SMM. This outcome suggests that the tightly-coupled GNSS standalone FGO methodology exhibits superior performance compared to the EKF-PDR integration in this context. The temporal variation in the number of satellites observed during the campus experiment is illustrated in Figure 3.9. The satellite count demonstrates fluctuations within the epoch range of 75 to 150, which is suboptimal for robust GNSS positioning. As depicted in Figure 3.9, the error magnitudes associated with FGO-PDR (light orange curve) are demonstrably lower than those of both standalone FGO (red curve) and FGO-CV-SMM (pink curve) within this timeframe. This observation substantiates the assertion that the proposed PDR factor retains its efficacy in maintaining positioning accuracy, particularly in GNSS-denied or challenged environments, thereby fulfilling the requirements for pedestrian navigation.

3.2.2 Experimental Evaluation in a Dense Urban Area

To challenge the effectiveness of the SMM factor and PDR factor for localization in complex scenes, we conducted another experiment in an even denser urban area. Figure 3.10 shows the pseudorange quality of this dataset in terms of the DD pseudorange error. The max error is larger than 200 meters, and the mean value of the DD pseudorange error is 30.55 meters. The standard deviation value is 43.739.

Table 3.4 and Table 3.5 present the comparative positioning performance metrics for the aforementioned FGO-based GNSS/PDR integration methodologies. In this experimental scenario, the standalone FGO approach exhibits a mean error of 16.80 meters. This value is demonstrably larger than the mean error observed in the campus experiment (14.97 meters), a discrepancy attributable to the increased density of buildings in the current environment, which presents a more challenging setting for satellite signal propagation. Following the integration of the SMM factor, the FGO-CV-SMM configuration demonstrates superior performance relative to standalone FGO. This observed phenomenon provides empirical validation of the assertion that the proposed SMM factor effectively mitigates the adverse impacts of GNSS outliers within densely built urban areas. Intriguingly, FGO-PDR and FGO-PDR-SMM exhibit comparable levels of performance. The incorporation of the CV factor in FGO-PDR-CV results in a reduction of the mean error to 13.20 meters. This outcome substantiates the effectiveness of employing the constant velocity assumption in pedestrian navigation contexts. Further application of the SMM factor, yielding the FGO-PDR-CV-SMM configuration, leads to a further reduction in the mean error to 13.10 meters. This incremental improvement reinforces the conclusion regarding the SMM factor's capacity to effectively mitigate potential GNSS outliers within GNSS/PDR integrated positioning systems under the conditions of this experimental scenario.

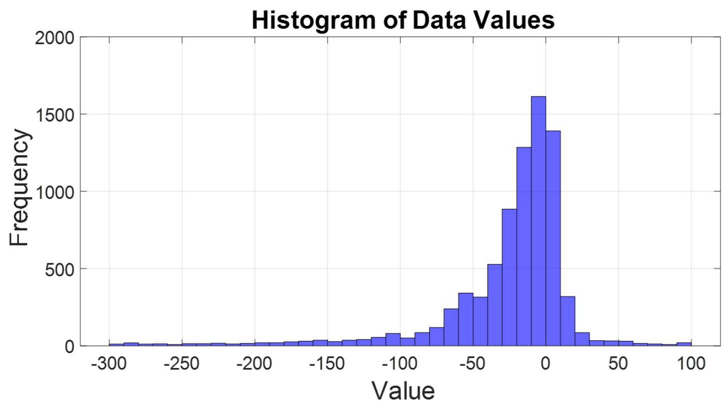

Fig. 3.10. Histogram of the DD pseudorange error in campus experiment.

Table 3.4. Positioning performance of the listed methods in dense urban canyon

All Methods	RMSE (m)	MEAN (m)	STD (m)	MAX (m)
FGO	19.61	16.80	10.11	76.29
EKF-PDR	26.20	21.39	15.15	148.74
FGO-CV	20.53	17.50	10.74	108.94
FGO-CV-SMM	19.42	16.66	9.97	74.02
FGO-PDR	15.12	13.55	6.72	56.92
FGO-PDR-SMM	15.12	13.55	6.72	57.00
FGO-PDR-CV	14.51	13.20	6.04	50.01
FGO-PDR-CV-SMM	14.36	13.10	5.88	45.09

Table 3.5. Improvements of the listed methods in dense urban canyon

Improvements	RMSE (m)	MEAN (m)	STD (m)	MAX (m)
FGO	/	/	/	/
EKF-PDR	-33.64%	-27.28%	-49.83%	-94.95%
FGO-CV	-4.72%	-4.16%	-6.25%	-42.80%
FGO-CV-SMM	0.96%	0.82%	1.33%	2.98%
FGO-PDR	22.87%	19.35%	33.55%	25.39%
FGO-PDR-SMM	22.87%	19.37%	33.52%	25.29%
FGO-PDR-CV	25.98%	21.46%	40.22%	34.45%
FGO-PDR-CV-SMM	26.78%	22.05%	41.84%	40.91%

Figure 3.11 and Figure 3.12 respectively illustrate the two-dimensional (2D) positioning trajectories, contextualized within OpenStreetMap [82], and the horizontal positioning errors observed in the dense urban scenario. In this particular scenario, the ground truth trajectory is characterized by a linear path, thereby facilitating a straightforward comparative analysis of trajectory smoothness across all evaluated methodologies. It is apparent that the degradation of GNSS pseudorange accuracy, resulting from signal reflections prevalent in dense urban environments, leads to the

occurrence of outliers. These outliers have a demonstrably detrimental impact on the performance of EKF-PDR (depicted by the green curve). Indeed, the EKF-PDR approach yields results inferior to those of standalone GNSS-FGO in this scenario, exhibiting a substantial deviation from the ground truth trajectory. In contrast to standalone FGO, the FGO-PDR-CV-SMM method produces a trajectory that is perceptibly smoother and more consistent with the expected linear path.

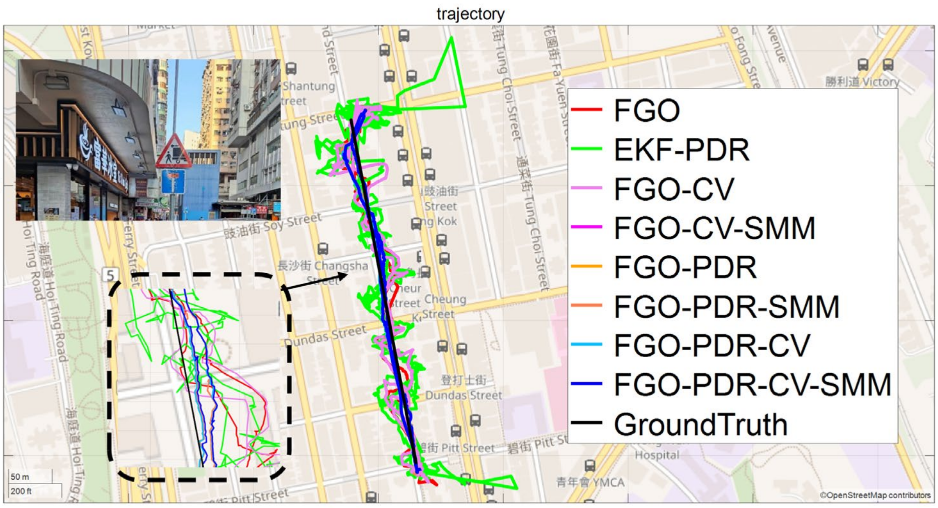

Fig. 3.11. Trajectories of evaluated eight methods in the urban canyon in OpenStreetMap [82].

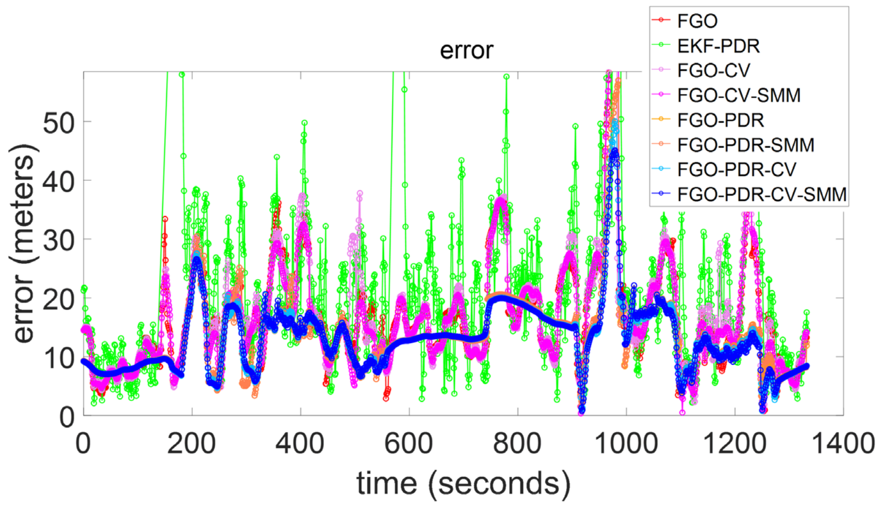

Fig. 3.12. Horizontal positioning errors in the dense urban experiment.

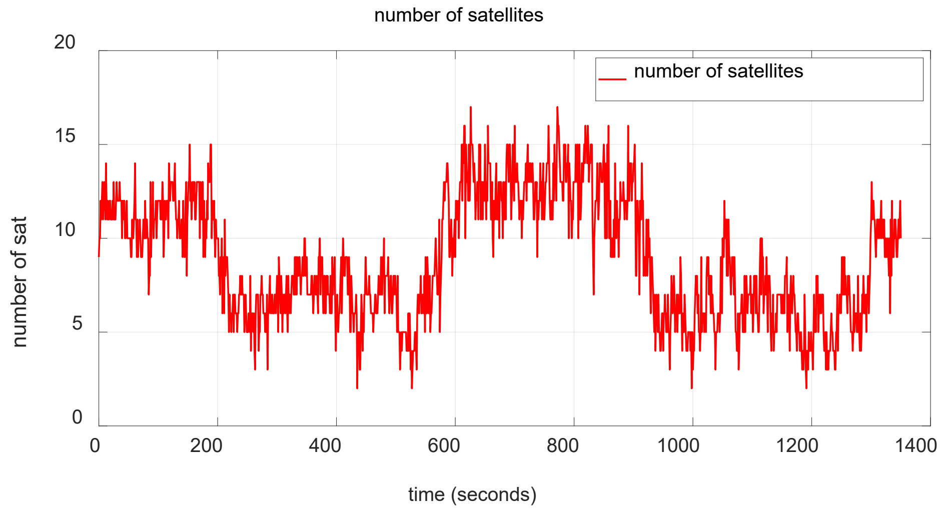

Fig. 3.13. The relationship between the number of satellites with time.

Figure 3.13 shows the number of satellites in the deep urban experiment with time. FGO-CV (light pink) and FGO-CV-SMM (pink curve), which without adding the PDR factor, reach an error close to 30 meters during epoch 250-400. The FGO-PDR (light orange curve) with the PDR factor added also shows resistance to the decreased data redundancy caused by the insufficient number of satellites.

3.2.3 Experimental Evaluation in the Mixed Scenario

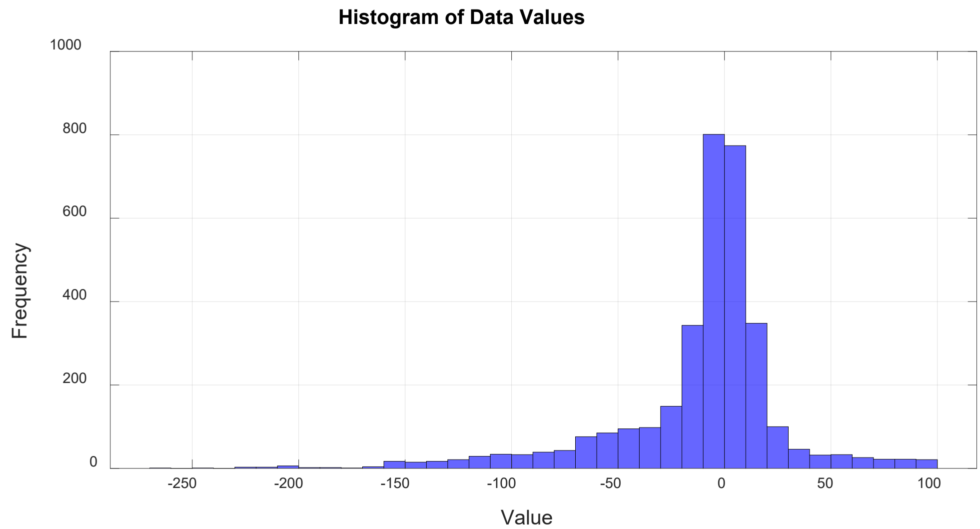

Fig. 3.14. Histogram of the DD pseudorange error in mixed scenario.

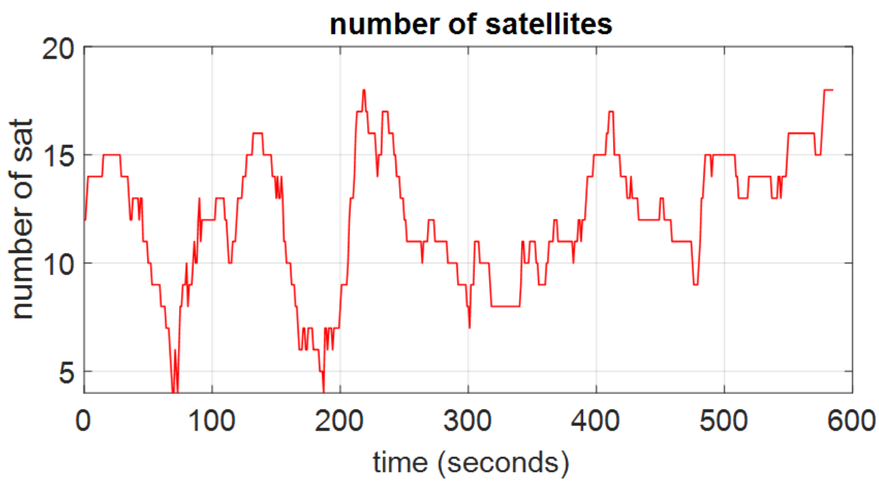

Fig. 3.15. The relationship between the number of satellites with time.

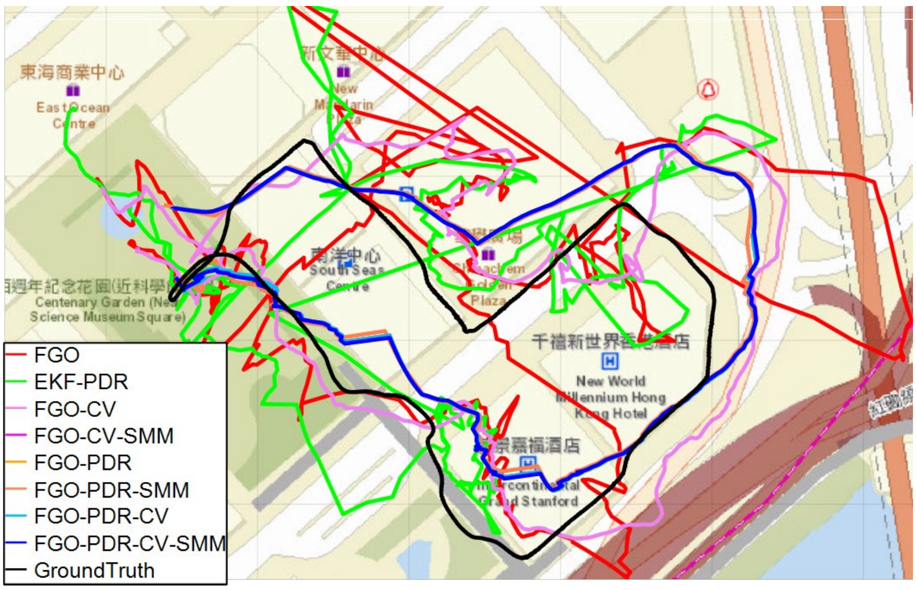

Fig. 3.16. Trajectories of evaluated eight methods in the urban canyon in OpenStreetMap [82].

Table 3.6. Positioning performance of the listed methods in the mixed scenario

All Methods	RMSE (m)	MEAN (m)	STD (m)	MAX (m)
FGO	39.23	31.64	23.21	149.16
EKF-PDR	35.20	29.58	19.10	144.03
FGO-CV	26.00	22.85	12.42	63.43
FGO-CV-SMM	25.60	22.29	12.59	57.91
FGO-PDR	21.23	18.57	10.31	36.53
FGO-PDR-SMM	21.66	18.84	10.70	39.88
FGO-PDR-CV	21.23	18.57	10.31	36.53
FGO-PDR-CV-SMM	21.20	18.51	10.34	36.41

For a more comprehensive evaluation of the proposed method, we conducted one additional experiment. Figure 3.14 shows the DD pseudorange error distribution of this mixed scenario dataset. The mean value of the DD pseudorange error is 24.93 meters, and the standard deviation value of the errors is 33.90. Figure 3.15 shows satellite numbers at each epoch in this experiment. In most cases, the number of satellites is around 10. In extreme cases, there are only four satellites. Figure 3.16 shows the paths of eight different localization methods in the mixed scenario. The original FGO method performs very poorly in the mixed scene, which is due to the multipath effect present in the scene and the NLOS reception, and there is no motion model in the method, the motion constraints between frames are provided by the Doppler velocity factor [32]. Similar conclusions can be derived from Figure 3.17 which shows the 2D positioning errors of all the methods. Table 3.6 shows the statistical results of all the methods. The baseline algorithm, FGO, exhibited initial values of 39.23m RMSE, 31.64m Mean, 23.21m STD, and a Maximum error of 149.16m.

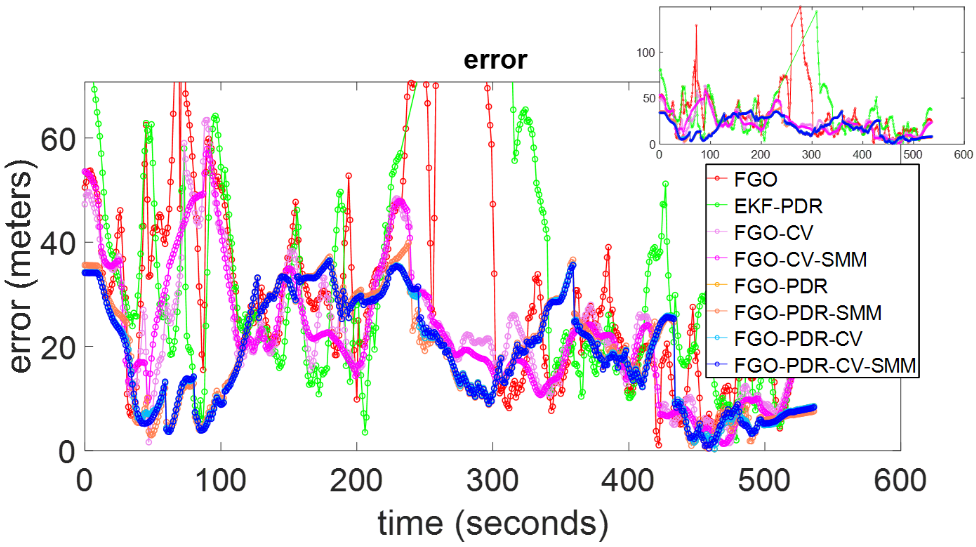

Fig. 3.17. Horizontal positioning errors in the mixed scenario. with time.

Upon integrating the Extended Kalman Filter with Pedestrian Dead Reckoning (EKF-PDR), we observed an overall performance increase with reductions in all metrics: the RMSE decreased to 35.20m, Mean to 29.58m, STD to 19.10m, and Max to 144.03m. This indicates an enhanced accuracy in the EKF-PDR algorithm over the standalone FGO which shows the improvement from PDR. The FGO-CV variant showed a significant improvement, particularly in the Maximum error, which was reduced to 63.43m, suggesting that the CV factor greatly contributes to limiting the maximum deviation of the algorithm under pedestrian walking conditions. The RMSE also has a notable reduction to 26.00m. Further incremental improvements were observed with the addition of the SMM factor in the FGO-CV-SMM configuration, with a slight decrease in the Mean error to 22.29m and an increase in STD to 12.59m, indicating a slightly increased variability in the errors. Substantial improvements were achieved by the FGO-PDR, which reduced the RMSE to 21.23m and the Max error to a remarkable 36.53m. This is indicative of significant enhancements in algorithm precision and reliability. Including the SMM factor to form the FGO-PDR-SMM configuration resulted in a minimal increase in STD and Max, suggesting that the SMM factor may introduce some variability under certain experimental conditions. The consistency of the performance was observed in the FGO-PDR-CV and FGO-PDR-CV-SMM configurations, which maintained the RMSE around 21.20m, and the Max error around 36.41m. These configurations represent the most balanced approach, with improvements across all metrics. With adding the SMM factor, the MEAN and RMSE are slightly decreasing to 18.51 meters and 21.20 meters, respectively. In conclusion, the integration of PDR, CV, and SMM components has proven to be highly effective in refining the accuracy and consistency of the algorithm. The experimental results indicate that these configurations can significantly enhance performance in complex urban environments, yielding a reliable algorithm that consistently minimizes errors.

3.3 Discussions

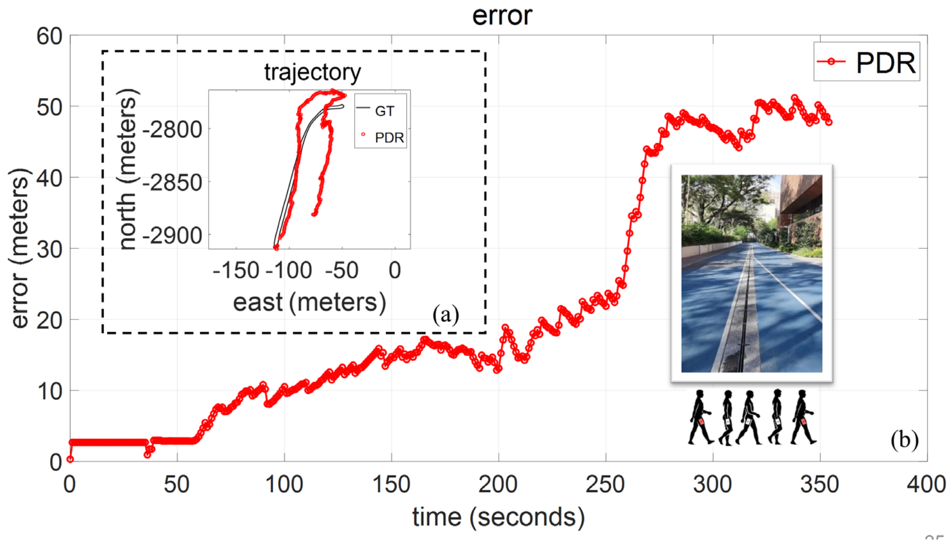

Fig. 3.18. (a) Horizontal PDR positioning trajectory in the campus experiment. The Ground Truth (GT) is the black curve. PDR trajectory is represented as the red curve. (b) 2D positioning error of the PDR in the campus experiment. The red curve denotes the PDR error.

Table 3.7 shows the performance of the employed PDR in the campus experiment. Figure 3.18 shows the employed PDR algorithm's horizontal trajectory and error. The PDR algorithm accumulated the errors over time, resulting in a very significant error in the PDR positioning results compared to the ground truth from the trajectory. The mean value of the positioning error of the PDR localization algorithm in the campus experiment is 21.04 m, while the RMSE is 26.74 m.

Table 3.7. Performance of the PDR in campus experiment

Items	RMSE (m)	MEAN (m)	STD (m)	MAX (m)
PDR	26.74	21.04	16.52	51.18

Figure 3.19 shows the error between 70-140 seconds in the campus experiment. During this period, the PDR algorithm has lower errors than the FGO-CV-SMM, indicating that the proposed PDR factor provides better constraints than the CV factor in the estimation process.

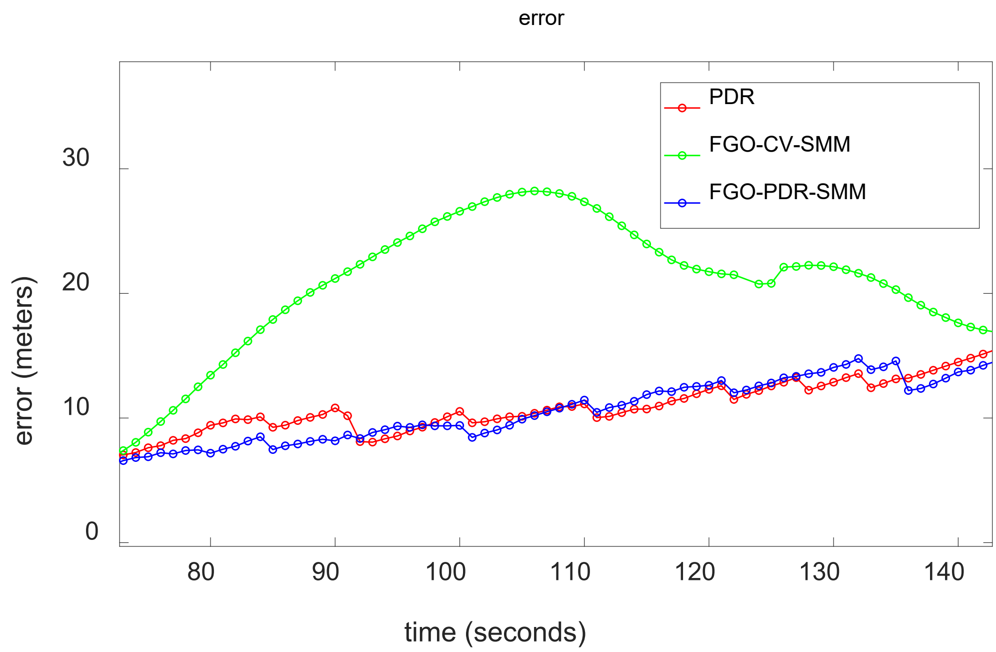

Fig. 3.19. 2D positioning error of PDR, FGO-CV-SMM, and FGO-PDR-SMM between 70 to 140 epochs in the campus experiment. The red, green, and cyan curves denote PDR, FGO-CV-SMM, and FGO-PDR-SMM, respectively.

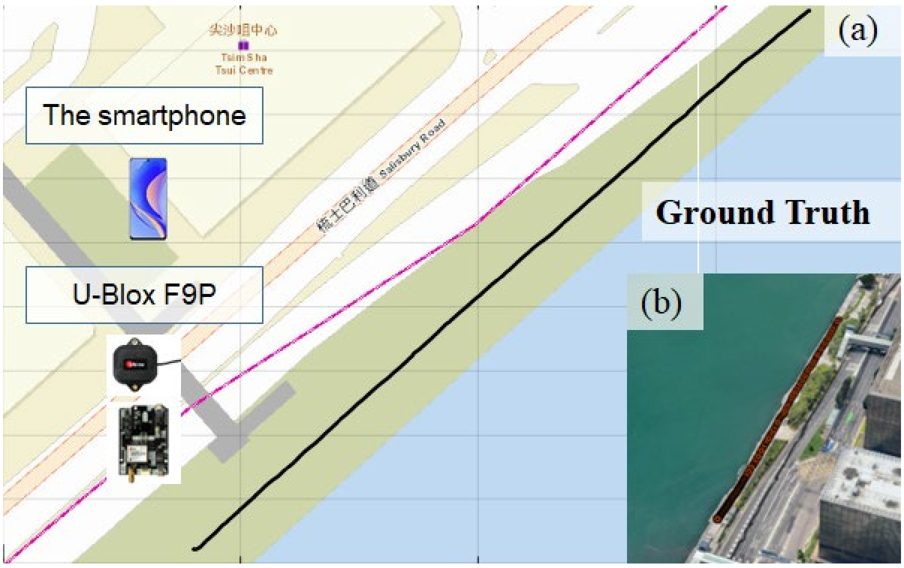

Fig. 3.20. The sensor setup of the seaside dataset. (a) image overview with GT from Google Earth. (b) the GT overview from OpenStreetMap. u-blox F9P system is used for generating the GT with RTK. The HUAWEI P40 Pro smartphone is used for collecting the GNSS and IMU measurements.

Figure 3.19 shows the horizontal positioning errors of the eight methods in this open-sky area. Figure 3.20 shows the configuration of the seaside experiment. In this scenario, we use u-blox F9P to collect GNSS L1/L2 signals in 1 Hz. The GT of this area is generated by the RTKLIB [33]. We use the combined mode real-time Kinematic (RTK) for calculating the GT by manually checking the positions and trajectories.

Table 3.8 presents the statistical results of the eight evaluated methods in this area. After incorporating the PDR factor into the system, the FGO-PDR-CV method exhibits degraded performance compared with the FGO-CV approach. This phenomenon indicates that PDR measurements may introduce additional errors due to the noisy smartphone IMU, particularly when a fixed covariance matrix is adopted for the PDR factor in the factor graph optimization framework. In contrast, the original FGO method achieves the best overall performance, outperforming FGO-CV. This observation suggests that, in the evaluated scenario, Doppler velocity measurements provide more effective constraints between consecutive states than the PDR-based motion model.

Table 3.8. Positioning performance of the listed methods in the seaside scenario

All Methods	RMSE (m)	MEAN (m)	STD (m)	MAX (m)
FGO	5.89	5.62	1.79	8.73
EKF-PDR	6.85	6.38	2.51	11.65
FGO-CV	6.08	5.74	2.02	9.56
FGO-CV-SMM	6.09	5.76	2.00	9.56
FGO-PDR	7.66	7.21	2.61	12.40
FGO-PDR-SMM	7.69	7.22	2.65	12.12
FGO-PDR-CV	7.61	7.15	2.59	11.87
FGO-PDR-CV-SMM	7.55	7.11	2.55	11.61

The enhanced performance observed in FGO-PDR compared to FGO-CV-SMM underscores the efficacy of incorporating the PDR factor within the integrated system. To further elucidate the impact of the PDR factor on the derived positioning solution across the two methodologies, an investigation of the residuals following convergence of the GNSS measurement models was conducted. The underlying principle posits that diminished residuals associated with applied measurements are indicative of potentially more accurate estimation outcomes. This is predicated on the assumption that a more consistent solution is derivable when the proportion of valid measurements exceeds that of compromised or erroneous measurements.

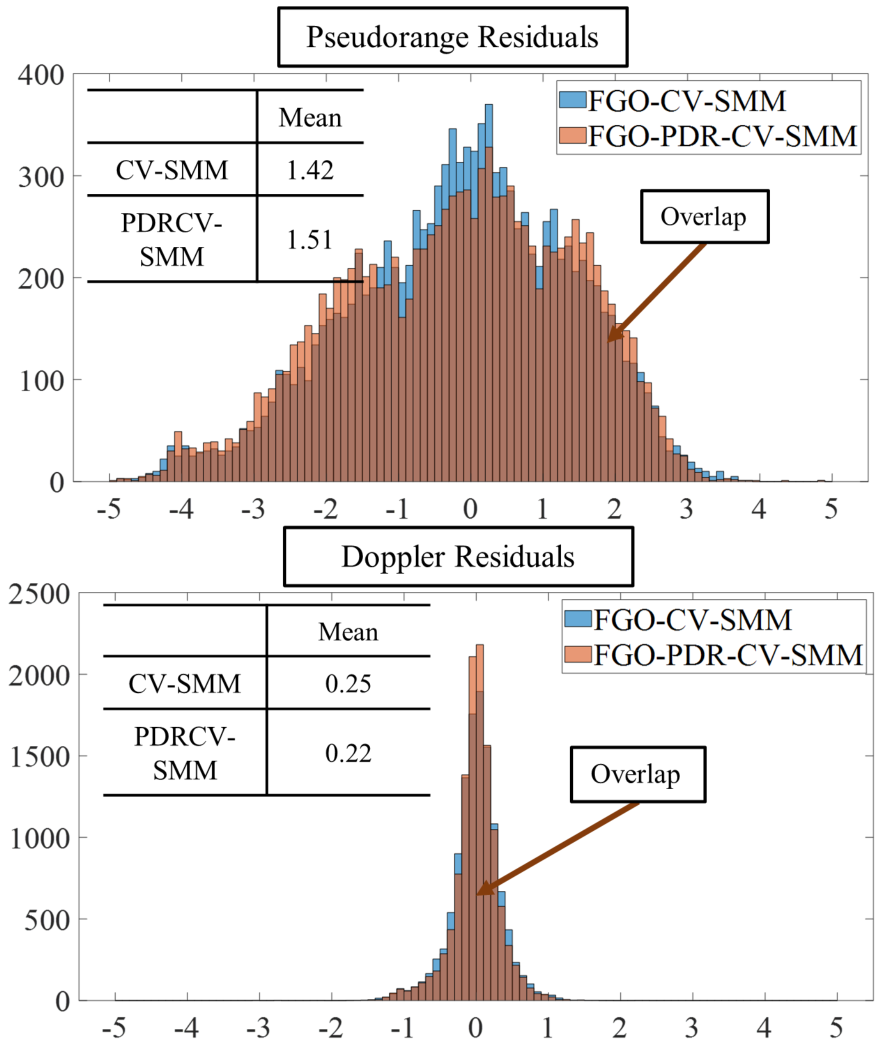

Fig. 3.21. Histograms of pseudorange factor and Doppler factor residuals. The x-axis denotes the value of residuals. The y-axis denotes the counts of residuals within the histogram.

Figure 3.21 presents a histogram-based comparison of pseudorange and Doppler factor residuals subsequent to optimization using the two specified methods. With respect to pseudorange measurements, the histogram reveals that the peak of FGO-CV-SMM pseudorange factor residuals, centered around zero, is higher in magnitude compared to that of FGO-PDR-CV-SMM. It is well-established that pseudorange measurements are indispensable for standalone GNSS positioning, as they provide the basis for absolute position determination. Notably, the positioning results obtained with FGO-PDR-CV-SMM demonstrate superior performance, despite exhibiting larger pseudorange residuals compared to FGO-CV-SMM.

Interestedly, a different phenomenon occurs in Doppler residuals. The mean value of the FGO-CV-SMM Doppler factor residuals is higher than the mean value of FGO-PDR-CV-SMM residuals. The potential reason is that the Doppler is less affected by the multipath effect while the pedestrian is walking along the street [149]. As a result, the assumption that the percentage of healthy measurements exceeds the one from polluted measurements could be largely held for the Doppler measurements.

3.4 Conclusions

In conclusion, pedestrian navigation within urban canyon environments remains a formidable challenge. This study introduces an innovative FGO-based GNSS/PDR positioning methodology designed to address this challenge. The proposed approach achieves a tightly-coupled integration of information derived from GNSS raw measurements and PDR, the latter being computed from magnetometer and accelerometer data acquired from the smartphone's internal IMU. This integration aims to facilitate accurate pedestrian positioning and generate smoother trajectory estimations. Furthermore, this study substantiates the validity of the assumption that pedestrians exhibit limited acceleration, which is leveraged for trajectory smoothing. The implementation of the SMM factor demonstrably enhances the system's robustness against potential GNSS outliers. To effectively model the dynamic characteristics of pedestrian navigation, a smoothness-driven motion model is proposed and integrated within the framework. Comparative evaluations against GNSS/PDR localization results obtained using extended Kalman filtering reveal a significant performance degradation for the EKF-based method in dense urban canyons. This degradation is primarily attributed to the susceptibility of EKF to GNSS outliers prevalent in such environments.

Building upon the tightly-coupled GNSS/PDR factor graph developed in this chapter, we have demonstrated that incorporating PDR-derived relative motion constraints can effectively smooth smartphone pedestrian trajectories and improve robustness against GNSS outliers in dense urban canyons. Nevertheless, when GNSS measurements are severely degraded by multipath and NLOS receptions, motion-consistency constraints alone may still be insufficient to prevent the estimated trajectory from drifting away from the physically feasible space. This observation motivates the exploitation of environmental priors that are naturally available in urban navigation scenarios. In particular, vehicles are constrained to travel on a road network, and such lane-level information can be formulated as additional multi-epoch constraints within the same FGO framework. Therefore, Chapter 4 extends the proposed FGO paradigm from integrating inertial/motion information to integrating geospatial road information, by tightly coupling Google Earth-derived road constraints with raw GNSS measurements. To mitigate the risk of erroneous map associations in complex urban layouts, a switchable-factor strategy is further introduced to adaptively down-weight unreliable lane constraints, enabling more robust road-constrained positioning for urban road monitoring applications.

4. ENHANCING GNSS POSITIONING ACCURACY FOR ROAD MONITORING SYSTEMS: A FACTOR GRAPH OPTIMIZATION APPROACH AIDED BY GEOSPATIAL INFORMATION

By reviewing studies about the map-aided positioning algorithm and the research gap in the current research stage, we aim to foster a broader understanding of map-matching inaccuracies and their impact on positioning precision. We also seek to demonstrate how our method parallels or deviates from these existing techniques. Therefore, inspired by the performance of integrating additional map information and the characteristics of the advanced FGO framework, this study employs an FGO-based approach to tightly couple the road information from Google Earth with raw GNSS measurements to solve for the receiver's position. To the best of the authors' knowledge, this study is the first research that combines map information with GNSS raw measurements using FGO. The main contributions of this study are threefold:

(1) *Multi-epoch-based lane matching model based on FGO*: This study proposed a novel FGO-based GNSS positioning system with a map-matching factor. The map-matching factor utilizes manually marked road information from Google Earth, a robust countermeasure against signal reflections and blockage in urban environments. This integration of geospatial data and FGO brings a new dimension to GNSS data processing and enhances the reliability of positioning in complex urban scenarios.

(2) *Switchable variable-based mis-lane matching mitigation*: Recognizing the intricacy of urban environments, which often feature multiple lane lines, this study proposes the switchable factor for comprehensively considering the multi-roads information. This factor aims to mitigate the potential for erroneous lane matching,

thereby enhancing the precision of our system. To succinctly explain, the switchable factor will represent this concept in the following text.

(3) *Extensive experimental validation*: The proposed methodology is comprehensively validated using real-world data collected from Hong Kong. This rigorous empirical assessment underscores our commitment to ensuring our innovations' practical applicability and performance. The step-by-step validation process provides clear insights into the performance of our system, demonstrating its potential for improving GNSS positioning in the real world.

4.1 Methodology

4.1.1 System Overview

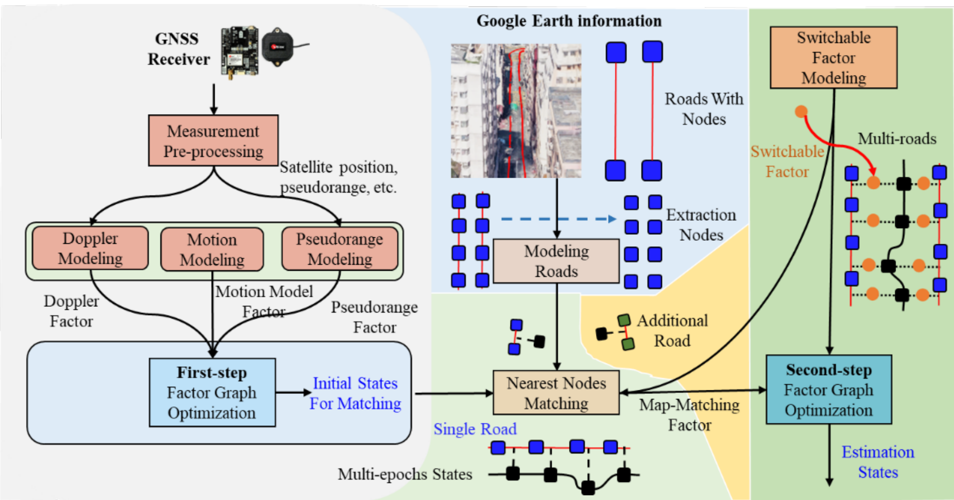

Fig. 4.1. The problem of urban GNSS positioning.

Our proposed map-aided GNSS positioning method, as depicted in Figure 4.1, leverages data from GE to improve the accuracy and reliability of GNSS positioning in urban canyons. The integrated GNSS/GE system consists of three primary components. The first component is the basic FGO part, which utilizes raw pseudorange and Doppler frequency measurements from the GNSS receiver. To ensure data quality, satellites with elevation angles (ELE) below 15 degrees or signal-to-noise ratios (SNR) below 20 are excluded. The basic FGO part provides initial states for the matching part. The second component incorporates geospatial information from GE. We mark the lanes in GE and divide each road into multiple nodes. For each initial state, we determine the nearest nodes for matching. By identifying the closest road with nodes, we create a map-matching factor for each epoch state. This allows us to utilize multi-epoch constraints for global lane alignment. Additionally, we propose a switchable factor to ensure reliable lane alignment. Unlike the previous map-matching factor, the switchable factor provides more options for optimization by integrating two roads into the estimation simultaneously. The output of the GNSS/Map integration is the user's state estimation, which includes position, velocity, clock biases, and clock drift. The positioning solution is obtained by solving the optimization problem, incorporating various constraints and factors. These factors encompass the pseudorange, Doppler frequency, and motion model (MM) factor, which smooths the receiver's trajectory. Notably, we introduce a map-matching factor and switchable factor in this study, aligning the user's trajectory with the road network from Google Earth. This effectively mitigates the influence of multi-path effects in urban canyons.

4.1.2 Basic FGO model

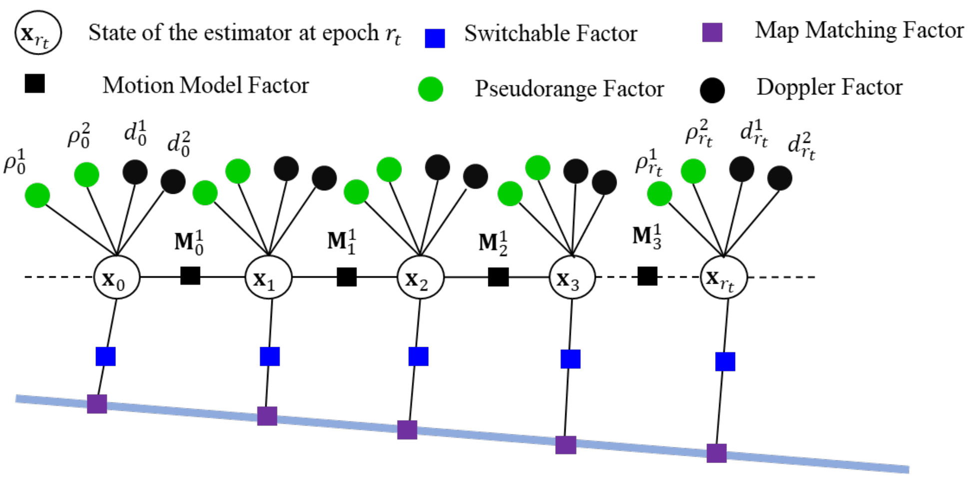

Fig. 4.2. Overview of the proposed factor graph.

Table 4.1 shows the descriptions of the parameters in this section for a clear explanation. Figure 4.2 shows our proposed factor graph. The black, blue, and purple rectangular denote the motion model factor, the switchable factor, and the map matching factor, respectively. The green and black circles denote the pseudorange and Doppler frequency factors, respectively. The subscript k denotes the total epochs of measurements considered in the FGO.

Table 4.1 Parameters and their description in this section

Parameter name	***Description***
r	The GNSS receiver
s	The index of the satellite
t	The time epoch
$\rho_{r,t}^{s}$	The pseudorange measurement
$d_{r,t}^{s}$	The Doppler measurement
$rr_{r,t}^{s}$	The expected range rate
$\mathbf{p}_{t}^{s}$	The satellite position $\mathbf{p}_{t}^{s} = (p_{t,x}^{s}, p_{t,y}^{s}, p_{t,z}^{s})^{T}$
$\mathbf{v}_{t}^{s}$	The velocity of the satellite $\mathbf{v}_{t}^{s} = (v_{t,x}^{s}, v_{t,y}^{s}, v_{t,z}^{s})^{T}$
$\mathbf{p}_{r,t}$	The position of the GNSS receiver $\mathbf{p}_{r,t} = (p_{r,t,x}, p_{r,t,y}, p_{r,t,z})^{T}$
$\mathbf{v}_{r,t}$	The velocity of the GNSS receiver $\mathbf{v}_{r,t} = (v_{r,t,x}, v_{r,t,y}, v_{r,t,z})^{T}$
$\delta_{r,t}$	The clock bias of the GNSS receiver
$\delta_{r,t}^{s}$	The satellite clock bias by meters

The GNSS receiver state set is represented as follows:

$$\boldsymbol{\chi} = [\mathbf{x}_{\mathrm{r},1}, \mathbf{x}_{\mathrm{r},2}, \dots, \mathbf{x}_{r,k}] \tag{4.1}$$

$$\mathbf{x}_{r,t} = (\mathbf{p}_{r,t}, \mathbf{v}_{r,t}, \boldsymbol{\delta}_{r,t}, \dot{\boldsymbol{\delta}}_{r,t})^{T} \tag{4.2}$$

where the variable $\boldsymbol{\chi}$ denotes the state set of the GNSS receiver ranging from the first epoch to the current k. $\mathbf{x}_{r,t}$ denotes the state of the GNSS receiver at epoch t which involves the position ($\mathbf{p}_{r,t}$), velocity ($\mathbf{v}_{r,t}$, receiver clock bias ($\boldsymbol{\delta}_{r,t}$) and clock drift $\dot{\boldsymbol{\delta}}_{r,t}$.

This study's main contribution is not the pseudorange, Doppler frequency, and motion model factors [118, 150, 151]. Thus, this study will briefly introduce these three factors for estimating the initial pose in our proposed map-aided system. The GNSS pseudorange factor can be written as:

$$\left\|e_{r,t}^{s,P}\right\|_{\boldsymbol{\Sigma}_{r,t}^{s}}^{2} = \left\|\rho_{r,t}^{s} - \left\|p_{t}^{s} - p_{r,t}\right\| - \delta_{r,t}\right\|_{\boldsymbol{\Sigma}_{r,t}^{s}}^{2} \tag{4.3}$$

where $\omega_{r,t}^{s}$ denotes the noise, $\boldsymbol{\Sigma}_{r,t}^{s}$ denotes the covariance matrix, calculated using satellite SNR and ELE [152]. The Doppler frequency factor can be written as:

$$\left\|e_{r,k}^{s,D}\right\|_{\boldsymbol{\Sigma}_{r,t}^{D}}^{2} = \left\|\lambda d_{r,t}^{s} - rr_{r,t}^{s}\right\|_{\boldsymbol{\Sigma}_{r,t}^{D}}^{2} \tag{4.4}$$

where $\boldsymbol{\Sigma}_{r,t}^{D}$ denotes the covariance matrix corresponding to the Doppler measurement which is equal $\boldsymbol{\Sigma}_{r,t}^{s}$ multiplied by a fixed coefficient valued at 10. λ is the wavelength.

The motion model factor is constructed for smoothing the vehicle trajectory. We can get the observation model for the smartphone-level GNSS receiver velocity ($\mathbf{v}_{r,t}$) expressed as follows:

$$\left|\left|\mathbf{e}_{r,t}^{C}\right|\right|_{\boldsymbol{\Sigma}_{r,t}^{C}}^{2} = \left|\left|\Delta\mathbf{p}_{r,t} - (\mathbf{v}_{r,t} + \mathbf{v}_{r,t+1})/2\right|\right|_{\boldsymbol{\Sigma}_{r,t}^{C}}^{2} \tag{4.5}$$

where the $\mathbf{v}_{r,t}$ and $\mathbf{v}_{r,t+1}$ denote the velocity at two consecutive epochs with three-dimension in the Earth-centered, Earth-fixed coordinate (ECEF) frame, respectively. $\Delta p_{r,t,x}$, $\Delta p_{r,t,y}$, $\Delta p_{r,t,z}$ denote the receiver displacement between two consecutive epochs at three dimensions. The variable $\boldsymbol{\omega}_{r,t}^{C}$ denotes the noise associated with constant motion. $\boldsymbol{\Sigma}_{r,t}^{C}$ denotes the covariance matrix corresponding to the receiver velocity measurement. This study empirically [148] set $\boldsymbol{\Sigma}_{r,t}^{C}$ as follows:

$$\boldsymbol{\Sigma}_{r,t}^{C} = \begin{bmatrix} 0.3^2 & 0 & 0 \\ 0 & 0.3^2 & 0 \\ 0 & 0 & 0.3^2 \end{bmatrix} \tag{4.6}$$

where the units for the covariance matrix is meter.

4.1.3 Incorporating GE Data in Multi-epoch GNSS Positioning

This section describes the methodology for incorporating Google Earth data into our GNSS positioning technique to improve accuracy and reliability in urban canyon environments.

Firstly, we retrieve relevant road information from the Google Earth database to incorporate GE data and manually mark the road's latitude and longitude. The method we extract road information is similar to our previous work that extracting 3D building models [139]. Initially, we ascertain the approximate lane ranges by conducting a comparative analysis with the terrain features depicted in GE. Subsequently, we refine the delineation of specific lanes through an iterative process, which involves a detailed comparison with the panoramic imagery available on Google Earth. The representation of the roadways is then accomplished by systematically plotting points along these identified lanes. The geographic coordinates (latitude and longitude) of these points are compiled to form a comprehensive dataset representing the specific lane information. Finally, we undertake a manual verification process to confirm the accuracy of the demarcated lanes, utilizing the camera data provided in the dataset [103] for validation. Thus, the road information can be denoted as follows:

$$\mathbf{R} = [\mathbf{R}_1, \mathbf{R}_2, \dots, \mathbf{R}_n] \tag{4.7}$$

$$\mathbf{R}_n = \begin{bmatrix} l_{1,x}, l_{1,y} \\ l_{2,x}, l_{2,y} \\ \vdots \\ l_{m,x}, l_{m,y} \end{bmatrix} \tag{4.8}$$

where $\mathbf{R}$ denotes the matrix of road information and $\mathbf{R}_\mathrm{n}$ denote the road with index n. $l_{m,x}$ and $l_{m,y}$ denote the longitude and latitude of the nodes of the road with the index m, respectively.

In the second step, we should consider incorporating road information into the optimization progress for better estimation based on the previously solved position. We can get the initial position for each epoch after solving the first-step optimization based on the previous GNSS factors and the MM factor. Once the initial position is determined, it is matched to the nearest two nodes by identifying the corresponding road indexes. Before we input these two roads into the map-matching factor, we should transform the coordinate system of the roads to ENU frame because we solely consider the horizontal errors in urban positioning. Then, we could employ a simple 2D linear function for describing the chosen line in the ENU frame. So finally, we can derive the specified k and b for each line for the two selected lines.

Finally, the error functions of the map-matching factor can be written as follows:

$$\left\| e_{r,k}^{0} \right\|_{\boldsymbol{\Sigma}_{r,t}^{rd}}^{2} = \| k_1 x^{ENU} - y^{ENU} + b_1 \|_{\boldsymbol{\Sigma}_{r,t}^{rd}}^{2} \tag{4.9}$$

where the superscript 0 denotes the closest road, $[x^{ENU}, y^{ENU}]^T$ denote the horizontal state position to be estimated in the ENU frame. k_1 is the slope of the selected roads in the ENU coordinate system. b_1 is the intercept of the selected roads in the ENU coordinate system. $\boldsymbol{\Sigma}_{r,t}^{rd}$ denotes the covariance matrix of the map-matching factor.

4.1.4 The switchable factor

In complex urban environments, relying solely on the position result of FGO to determine the matched road can easily lead to incorrect matching. To comprehensively consider the possibility of multiple roads and fully leverage the map information in the FGO process, our method considers the information from the two nearest roads simultaneously during the optimization process. Therefore, the map-matching factor would add one more road to Eqs. 8 and the aided factor can be written as:

$$\left\| \boldsymbol{e}_{r,k}^{1} \right\|_{\boldsymbol{\Sigma}_{r,t}^{rd}}^{2} = \| k_2 x^{ENU} - y^{ENU} + b_2 \|_{\boldsymbol{\Sigma}_{r,t}^{rd}}^{2} \tag{4.10}$$

where superscript 1 denotes the additional roads, $[x^{ENU}, y^{ENU}]^T$ denote the horizontal state position to be estimated in the ENU frame. k_2 is the slope of the selected roads in the ENU coordinate system. b_2 is the intercept of the selected roads in the ENU coordinate system. $\mathbf{\Sigma}_{r,t}^{rd}$ denotes the covariance matrix of the map-matching factor:

$$\mathbf{\Sigma}_{r,t}^{rd} = \begin{bmatrix} 0.1^2 & 0 \\ 0 & 0.1^2 \end{bmatrix} \tag{4.11}$$

This study considers the probabilities of multi-roads with a switchable factor [36]. The switchable factor is utilized to anchor the switch variables at an initial value of 1, preventing the optimization process from getting stuck in a local minimum with all zero switch values. After aiding the switchable factor into the map-matching factor, the factor could be rewritten as:

$$\left\|\mathbf{e}_{r,k}^{0}\right\|_{\mathbf{\Sigma}_{r,t}^{rd}}^{2} = s_k^i \|k_1 x^{ENU} - y^{ENU} + b_1\|_{\mathbf{\Sigma}_{r,t}^{rd}}^{2} \tag{4.12}$$

$$\left\|\mathbf{e}_{r,k}^{1}\right\|_{\mathbf{\Sigma}_{r,t}^{rd}}^{2} = \left(1 - s_k^i\right) \|k_2 x^{ENU} - y^{ENU} + b_2\|_{\mathbf{\Sigma}_{r,t}^{rd}}^{2} \tag{4.13}$$

where s_k^i denotes the switchable factor, the superscript i denotes the road index, and the subscript k denotes the epoch.

To avoid the switchable factor falling into a local minimum, we add the switchable prior factor into our framework [117, 153] :

$$\left\|\mathbf{e}_{r,k}^{s}\right\|_{\mathbf{\Sigma}_{r,t}^{s}}^{2} = \left\|1 - s_k^i\right\|_{\mathbf{\Sigma}_{r,t}^{s}}^{2} \tag{4.14}$$

where $\mathbf{\Sigma}_{r,t}^{s}$ is the covariance matrix of the switchable prior factor which equals to 1.0.

Therefore, we can formulate the objective function for the map-aided FGO-based GNSS system based on the factors derived above as follows:

$$\chi^* = \underset{\chi}{argmin} \sum_{s,t} (\left\| \mathbf{e}_{r,t}^{s,P} \right\|_{\boldsymbol{\Sigma}_{r,t}^{s}}^2 + \left\| \mathbf{e}_{r,t}^{C} \right\|_{\boldsymbol{\Sigma}_{r,t}^{C}}^2 + \left\| \mathbf{e}_{r,k}^{s,D} \right\|_{\boldsymbol{\Sigma}_{r,t}^{D}}^2$$
$$+ \left\| \mathbf{e}_{r,k}^{0} \right\|_{\boldsymbol{\Sigma}_{r,t}^{rd}}^2 + \left\| \mathbf{e}_{r,k}^{1} \right\|_{\boldsymbol{\Sigma}_{r,t}^{rd}}^2 + \left\| \mathbf{e}_{r,k}^{s} \right\|_{\boldsymbol{\Sigma}_{r,t}^{s}}^2) \quad (4.15)$$

The variable χ^* denotes the optimal estimation of the state sets. We employ the Ceres Solver [141] as a non-linear optimization solver to solve the above objective function. Concurrently, the Levenberg-Marquardt (L-M) algorithm [154] is utilized within our FGO processes to minimize the cost function iteratively. Overview of the Proposed Method

4.2 Experiment setup

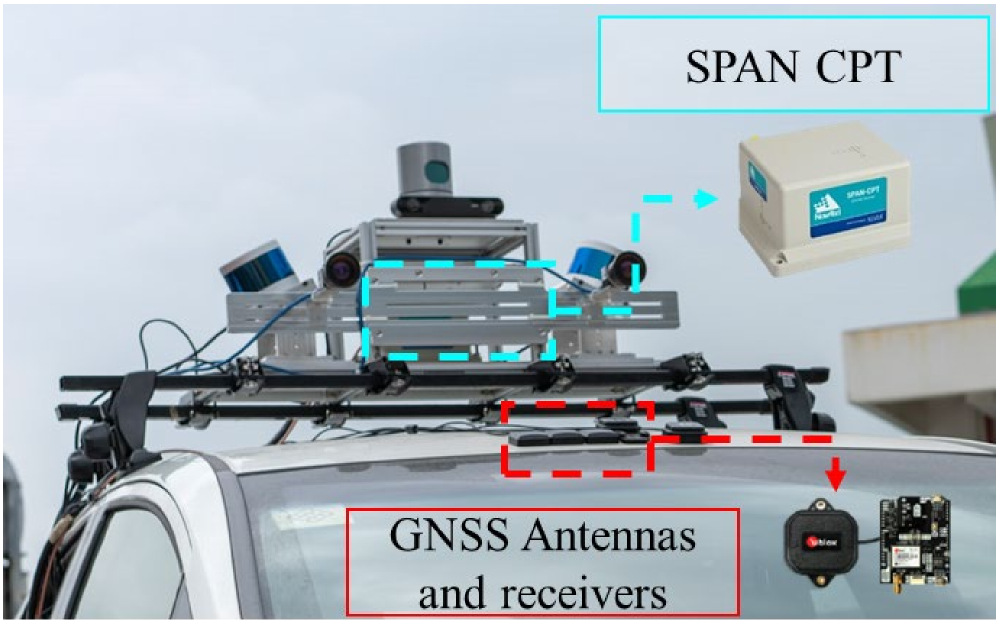

Fig. 4.3. The platform for the dataset collection.

To evaluate the performance of the proposed method, we gathered two datasets in a representative urban environment in Hong Kong. These two datasets show typical urban scenarios in Hong Kong, and we follow the definitions from [155]. The first dataset (Dataset 1) is gathered in deep urban, and another (Dataset 2) is collected in harsh urban. During the experiment, we utilized a u-blox F9P GNSS receiver to obtain raw GPS/BeiDou measurements at a frequency of 1 Hz. Additionally, the NovAtel SPAN-CPT, an integrated GNSS (GPS/ GLONASS/ BeiDou) RTK/INS (fiber-optic gyroscopes, FOG) navigation system, provided ground truth (GT) positioning data. The FOG's gyro bias in-run stability is 1 degree per hour, with a random walk of 0.067 degrees per hour. Prior to the experiments, the coordinate systems between all sensors were calibrated. Our data collection platform is shown in Figure 4.3.

4.2.1 The collected data in Hong Kong

Dataset 1 was collected in Whampoa, Hong Kong, a typical driving scenario due to the area's dense population and numerous residential districts. As a representative region of Hong Kong, vehicular GNSS positioning issues in this locale warrant considerable attention. We selected a random time slot during the day to gather data, with a collection length of nearly 1200 seconds. Figure 4.4-(a) demonstrates the variation in satellite count from the beginning to the end of the dataset's timeframe. As observed, in some extreme scenarios, the number of satellites is less than four, which is insufficient for GNSS positioning.

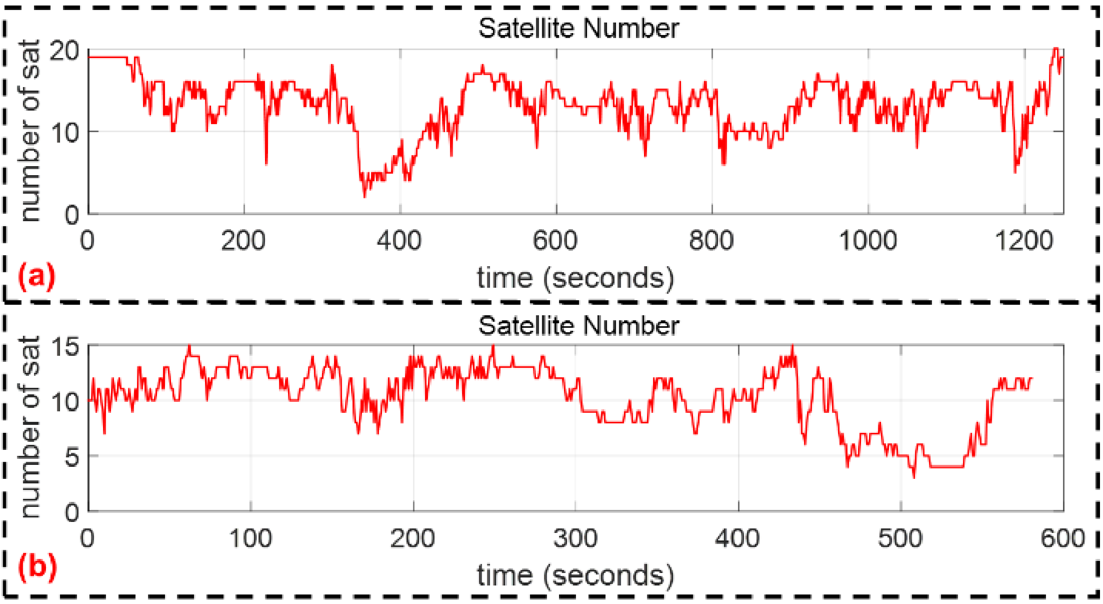

Fig. 4.4. The number of satellites in two datasets. (a) The satellite number of Dataset 1. (b) The satellite number of Dataset 2.

Different from the first dataset, the second dataset (Dataset 2) is collected in Mangkok, Hong Kong. This scenario has more high-rise buildings. A reduced number of satellites clearly illustrates this point. In the Whampoa dataset, the satellite count primarily fluctuates around 15, whereas in this dataset, it oscillates near 10, signifying a lower level of satellite redundancy. Figure 4.6-(b) shows the number of satellites in Dataset 2.

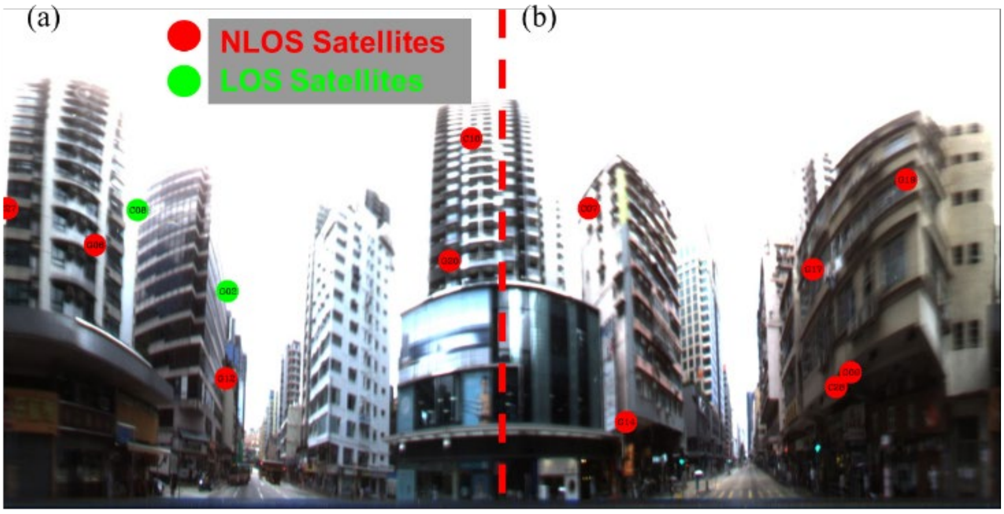

Fig. 4.5. Unfolded fish-eye camera figures with the satellite distributions in the urban canyon.

To further illustrate the difficulties of using GNSS positioning in urban canyons, we elucidate the issues in Dataset 1 by unfolding images from a fish-eye camera. As shown in Figure 7, Figure 7-(a) represents the back 180 degrees of the fish-eye camera, usually facing the rear of the vehicle, while Figure 7-(b) displays the satellite distribution in the vehicle's forward. Although the number of received satellites is sufficient in this scenario, it still contains numerous NLOS receptions or multi-path effects. Red circles denote the NLOS satellites, and green circles denote the LOS satellites. These signals can result in GNSS positioning errors.

4.2.2 Evaluation methods

We evaluated the performance of map-aided GNSS positioning by comparing three methods, as shown below. The objective of this analysis was to validate the effectiveness of the proposed method in improving FGO-based GNSS positioning. The accuracy is evaluated in the east, north, and up (ENU) frame by selecting the first point as the reference position.

(1) FGO [118]: conventional tightly-coupled GNSS pseudorange/doppler frequency positioning solution. This method utilizes raw measurements from the GNSS receiver and optimizes the positioning solution based on conventional factor graph optimization [118].

(2) 3DMA [156]: State-of-the-art urban GNSS positioning method. First, the weighted least square method is employed to obtain the initial guess of 3D-mapping-adied (3DMA). The sky masks of the corresponding areas can be generated based on the particles' location and the prior 3D map. Then, the likelihood of each particle can be calculated by GNSS shadow matching. The predicted and measured satellite visibilities with the predicted and measured ranging measurements are considered. Finally, the absolute position can be calculated from the weighted average of the particles' positions. This 3D-mapping-aided (3DMA) method is integrated with all constellations and L1/L2 frequency measurements.

(3) FGO-Matching: FGO-based GNSS positioning solution incorporating GE road data through a map-matching factor. This approach matches the initial positioning solution to the nearest road using road information from Google Earth.

(4) FGO-Switch: FGO-Matching aided by a switchable factor for reliable road selection. This method considers the probabilities of both the closest roads in the map-matching process, utilizing a switchable factor for considering both roads, adding robustness and reliability to the positioning solution.

Algorithm 4.1: Solution to FGO-Matching

Inputs: Road information **R**, GNSS measurements $\rho_{r,t}^{s}$ and $d_{r,t}^{s}$

Outputs: A set of state $\boldsymbol{\chi}$

Step 1 (Initialization): Initialize the state set $\boldsymbol{\chi}$ using the weighted least squares and solve the following equation to estimate the state $\boldsymbol{\chi}$:

$$\chi^{*} = \underset{\chi}{argmin} \sum_{s,t} \left(\left\| \mathbf{e}_{r,t}^{s,P} \right\|_{\boldsymbol{\Sigma}_{r,t}^{s}}^{2} + \left\| \mathbf{e}_{r,t}^{C} \right\|_{\boldsymbol{\Sigma}_{r,t}^{C}}^{2} + \left\| \mathbf{e}_{r,k}^{s,D} \right\|_{\boldsymbol{\Sigma}_{r,t}^{D}}^{2} \right)$$

Step 2 (Matching): Select the nearest lane to the state $\boldsymbol{\chi}$ from the road information in terms of calculating the closest point.

Step 3 (FGO-Matching): Solve the following equation to estimate the state $\boldsymbol{\chi}$

$$\chi^{*} = \underset{\chi}{argmin} \sum_{s,t} \left(\left\| \mathbf{e}_{r,t}^{s,P} \right\|_{\boldsymbol{\Sigma}_{r,t}^{s}}^{2} + \left\| \mathbf{e}_{r,t}^{C} \right\|_{\boldsymbol{\Sigma}_{r,t}^{C}}^{2} + \left\| \mathbf{e}_{r,k}^{s,D} \right\|_{\boldsymbol{\Sigma}_{r,t}^{D}}^{2} + \left\| \mathbf{e}_{r,k}^{0} \right\|_{\boldsymbol{\Sigma}_{r,t}^{rd}}^{2} \right)$$

Algorithm 4.2: Solution to FGO-Switch

Inputs: Road information **R**, GNSS measurements $\rho_{r,t}^{s}$ and $d_{r,t}^{s}$, a set of switchable variables $\mathbf{s}_{k}^{i}$

Outputs: A set of state $\boldsymbol{\chi}$ and a set of switchable variables $\mathbf{s}_{k}^{i}$

Step 1 (Initialization): Initialize the switchable variables $\mathbf{s}_{k}^{i}$ with fixed value 1.0. Initialize the state set $\boldsymbol{\chi}$ using the weighted least squares and solve the following equation to estimate the state $\boldsymbol{\chi}$:

$$\chi^{*} = \underset{\chi}{argmin} \sum_{s,t} \left(\left\| \mathbf{e}_{r,t}^{s,P} \right\|_{\boldsymbol{\Sigma}_{r,t}^{s}}^{2} + \left\| \mathbf{e}_{r,t}^{C} \right\|_{\boldsymbol{\Sigma}_{r,t}^{C}}^{2} + \left\| \mathbf{e}_{r,k}^{s,D} \right\|_{\boldsymbol{\Sigma}_{r,t}^{D}}^{2} \right)$$

Step 2 (Matching): Select the two nearest lanes to the state $\boldsymbol{\chi}$ from the road information in terms of calculating the closest point.

Step 3 (FGO-Switch): Solve the following equation to estimate the state $\boldsymbol{\chi}$

$$\chi^{*} = \underset{\chi}{argmin} \textstyle\sum_{s,t} (\left\| \mathbf{e}_{r,t}^{s,P} \right\|_{\boldsymbol{\Sigma}_{r,t}^{s}}^{2} + \left\| \mathbf{e}_{r,t}^{C} \right\|_{\boldsymbol{\Sigma}_{r,t}^{C}}^{2} + \left\| \mathbf{e}_{r,k}^{s,D} \right\|_{\boldsymbol{\Sigma}_{r,t}^{D}}^{2}$$
$$+ \left\| \mathbf{e}_{r,k}^{0} \right\|_{\boldsymbol{\Sigma}_{r,t}^{rd}}^{2} + \left\| \mathbf{e}_{r,k}^{1} \right\|_{\boldsymbol{\Sigma}_{r,t}^{rd}}^{2} + \left\| \mathbf{e}_{r,k}^{\mathrm{s}} \right\|_{\boldsymbol{\Sigma}_{r,t}^{s}}^{2})$$

In this study, we proposed two algorithms. The first algorithm is FGO-Matching which only considers one road information without switchable factors. The second algorithm is FGO-Switch which incorporates the road information with switchable factors. The detailed steps of FGO-Matching are shown in the algorithm 4.1. The detailed steps of FGO-Switch are shown in the algorithm 4.2.

4.3 Experiment results

All methods in this study are post-processing methods. FGO-Switch typically runs 120% more than FGO-Matching with 3.3 seconds per epoch for FGO-Switch and 1.5 seconds per epoch for FGO-Matching in Dataset 1.

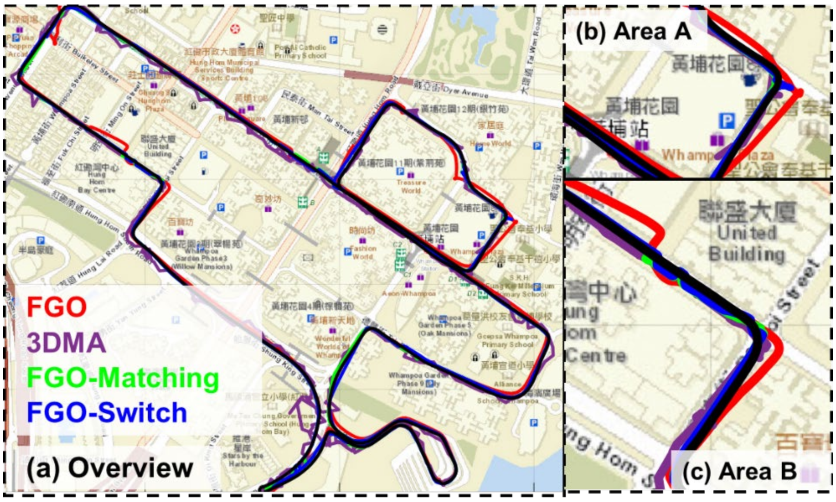

Fig. 4.6. Trajectories overview of Dataset 1.

Figure 4.6 illustrates the positioning trajectories of FGO, FGO-Matching, and FGO-Switch in Dataset 1, corresponding to red, green, and blue, respectively. The trajectories show that FGO is prone to erroneous positioning results in urban environments, causing the actual trajectory to deviate from city roads onto buildings. Figures 4.6-(b) and 4.6-(c) show that FGO has a significant drift in these scenarios. In contrast, methods incorporating map matching can reduce errors in scenarios with severe drift, as evidenced by trajectories returning to the roadways.

Figure 4.7 illustrates the positioning trajectories of FGO, FGO-Matching, and FGO-Switch in Dataset 2. Similar to the results in Dataset 1, FGO positioning yields erroneous results in more challenging urban environments, causing the actual positioning results to deviate from city roads and drift into buildings. The 3DMA method shows larger errors than other FGO-based methods in this scenario. By incorporating map-matching methods, errors can be reduced even in cases of severe drift, as trajectories are readjusted to the roadways based on road information from Google Earth.

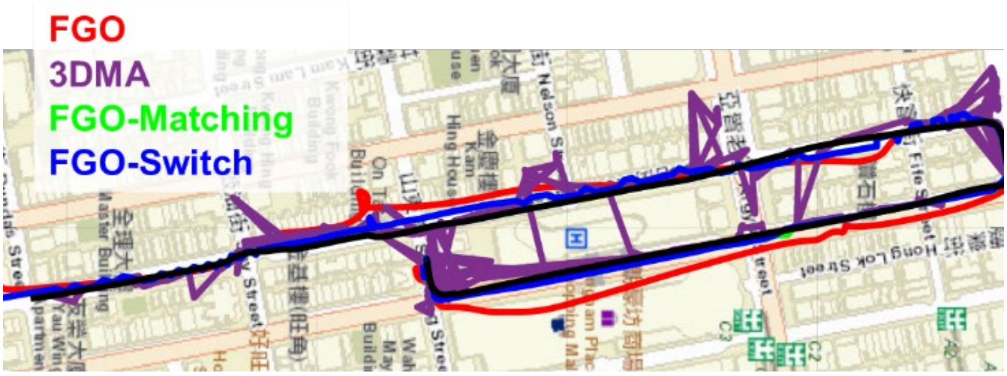

Fig. 4.7. Trajectories overview of Dataset 2.

Table 4.2 presents the positioning error comparison in meters for Dataset 1, evaluating the performance of different methods, including FGO, FGO-Matching, 3DMA, and FGO-Switch. The metrics include Root Mean Square Error (RMSE), Mean, Standard Deviation (STD), and Maximum Error (MAX). The 3DMA method shows a slight improvement over FGO and FGO-Matching, with an RMSE of 10.91m and a mean error of 8.41m. However, the standard deviation increased to 6.95m, indicating a slightly higher variability in the results. Notably, the maximum error for 3DMA was significantly higher at 58.5m, indicating occasional large deviations from the expected position. Compared to FGO, the FGO-Matching method demonstrates improvements in RMSE by 10.27%, Mean by 11.52%, and STD by 7.41%. These improvements indicate that the FGO-Matching method provides superior accuracy and precision in positioning. However, the maximum error increases slightly by -3.23%, suggesting that, in some instances, the FGO-Matching method might generate more significant errors than the FGO method. When comparing the FGO-Switch to the FGO method, we notice further enhancements in RMSE by 13.36%, Mean by 14.55%, and STD by 10.63%. The result demonstrates that the FGO-Switch method further improves positioning accuracy and precision compared to FGO-Matching. Moreover, the MAX shows a marginal improvement of 0.95%, indicating that the FGO-Switch method can also effectively control the maximum error. In summary, both FGO-Matching and FGO-Switch methods outperform the FGO method regarding positioning accuracy and precision. Furthermore, the FGO-Switch method appears to be more effective in controlling the maximum error and offers slightly better overall improvements compared to the FGO-Matching method.

Table 4.2 2D Positioning performance of all methods in Dataset 1

All Methods	RMSE (m)	MEAN (m)	STD (m)	MAX (m)
FGO	11.66	9.76	6.39	26.75
3DMA	10.91	8.41	6.95	58.45
FGO-Matching	10.47	8.63	5.92	27.62
FGO-Switch	10.11	8.34	5.71	26.50

Table 4.3 2D Positioning performance of all methods in Dataset 2

All Methods	RMSE (m)	MEAN (m)	STD (m)	MAX (m)
FGO	15.02	12.31	8.62	29.03
3DMA	31.47	20.27	24.09	136.34
FGO-Matching	10.71	8.15	6.95	27.19
FGO-Switch	10.88	8.35	6.98	27.14

Table 4.3 presents the positioning error comparison in meters for Dataset 2. The 3DMA method exhibits relatively lower performance on this dataset compared to all FGO-based methods. A potential contributing factor could be the suboptimal initial estimates derived from the weighted least squares results, which may adversely affect

the overall estimation accuracy. In a comparison against the FGO method, the FGO-Matching approach yields substantial improvements across several key metrics. We observed a decrease of 28.72% in the RMSE, 33.82% in the MEAN, and 19.30% in the STD. These improvements suggest a significant enhancement in positioning accuracy and precision with the implementation of FGO-Matching for this dataset. The MAX also improved by 6.33%, indicative of the method's effectiveness in reducing the most significant positioning errors relative to the conventional FGO approach.

On the other hand, when analyzing the FGO-Switch method against the FGO approach, we also noted appreciable improvements. There was a reduction of 27.55% in RMSE, 32.14% in Mean, and 18.98% in STD. These results demonstrate that FGO-Switch provides superior positioning accuracy and precision compared to the conventional FGO method. Furthermore, we also observed a slight improvement of 6.51% in the Maximum Error, implying that the FGO-Switch method has a credible capacity to handle the maximum error effectively. FGO-Matching has better performance compared to the FGO-Switch. One potential reason for this suboptimal performance is similar to the 3DMA method that a bad initial guess for map-matching leading to erroneous estimation. This error could also be caused by the motion model factor, leading to inaccurate global estimation. Although FGO-Matching performed slightly better regarding RMSE, MEAN, and STD, FGO-Switch has advantages in some cases. The primary advantage of FGO-Switch is that it effectively handles the potential problem of wrong map-matching by considering the probabilities of both roads using a switchable factor, which adds redundancy to the method.

To better elucidate the error data listed in Table 4.2 and 4.3, Figures 4.8 and 4.9 respectively display the trends of GNSS errors over time in the two datasets. As with the previously plotted trajectories, red, green, and blue denote FGO, FGO-Matching, and FGO-Switch, respectively. We can observe that between 400 and 700 seconds, both proposed methods exhibit significant improvements compared to the FGO, with a notable reduction in errors. This demonstrates that our proposed map-matching-based FGO method can effectively utilize the added map information to counteract the impact of GNSS outliers caused by multi-path effects or NLOS receptions.

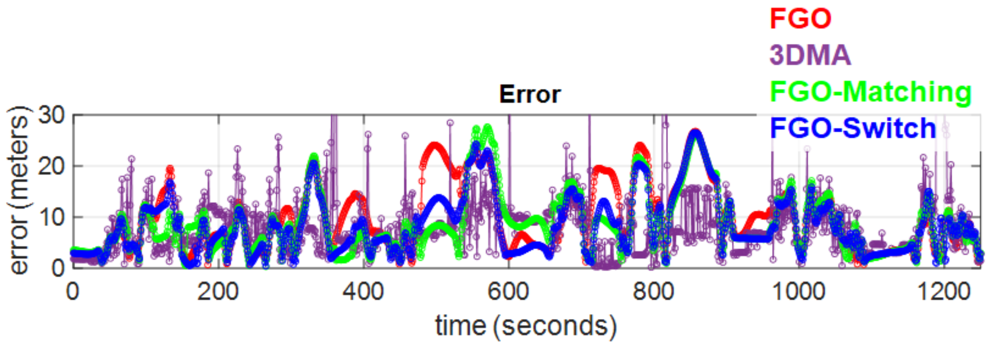

Fig. 4.8. 2D positioning errors of three methods in Dataset 1

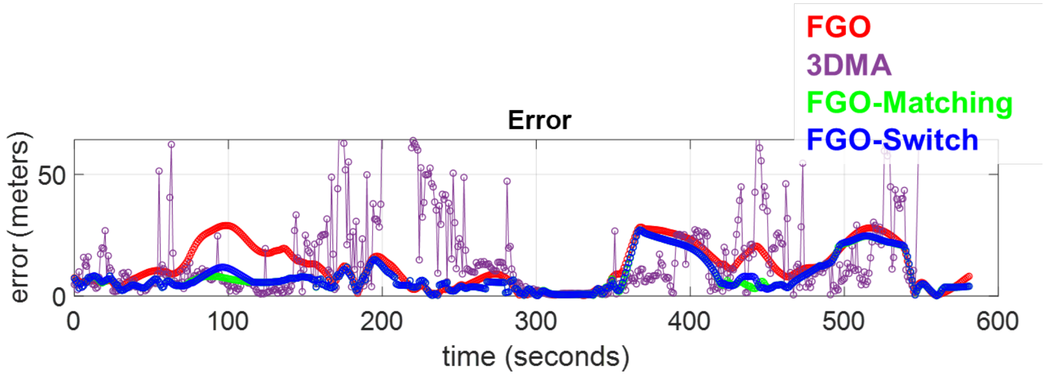

Fig. 4.9. 2D positioning errors of three methods in Dataset 2

Figure 4.11 shows the performance of the three evaluation methods in Dataset 2. Our proposed approach demonstrates more significant optimization in this scenario. The error of FGO (red curve) reaches around 30 meters at approximately 100 seconds, while by incorporating lane constraints from the map in the optimization process, we can observe that both FGO-Matching and FGO-Switch effectively resist outliers, with errors distributed around 10 meters.

4.4 Discussion

This study demonstrates that incorporating the switchable factor into our GNSS positioning system is instrumental in accurately selecting the correct lane for the estimated trajectories. Figure 4.10 compares the trajectories of three methods: FGO, FGO-Matching, and FGO-Switch. The red circle means the scenario in FGO-matching chose the wrong road. Figures 4.10-(a), 4.10-(b), and 4.10-(c) all show the estimated trajectories for the respective method alongside the ground truth trajectory. Compared to the FGO and the FGO-Matching methods, we can observe that the FGO-Switch method achieves better lane selection and positioning accuracy. By integrating the switchable factor, the FGO-Switch method can effectively weigh the probability of the vehicle being on two adjacent lanes, enabling it to select the correct lane more consistently. The switchable factor is a constraint that prevents reliable lane selection. In conclusion, Figure 4.12 provides strong evidence that incorporating the switchable factor into our GNSS positioning system significantly improves the accuracy of lane selection, leading to better overall positioning performance in urban environments.

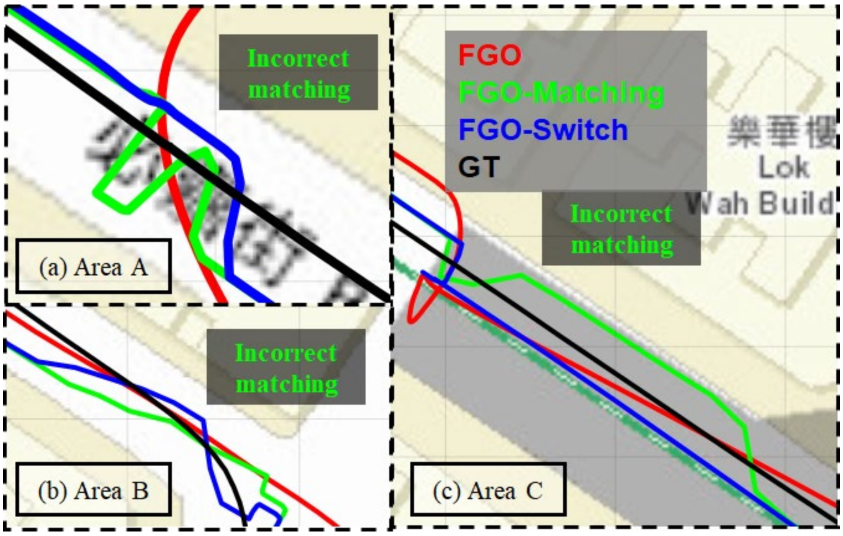

Fig. 4.10. Comparison of three methods

Figure 4.11 illustrates the error values associated with three distinct methods, measured in a direction perpendicular to the GT. It is essential to highlight that these evaluations were limited to dynamic scenes due to the absence of a motion direction in static scenarios. The figure shows a significant fluctuation in the error curve associated with the FGO method (represented by the red curve). Notably, the peak value of this curve markedly surpasses that of the method incorporating map matching. In contrast, FGO-Switch (depicted by the blue curve) demonstrates superior performance compared to FGO-Matching at approximately 200 and 600 seconds. This pattern suggests that our proposed switchable factor can more effectively facilitate vehicle lane-matching within this context.

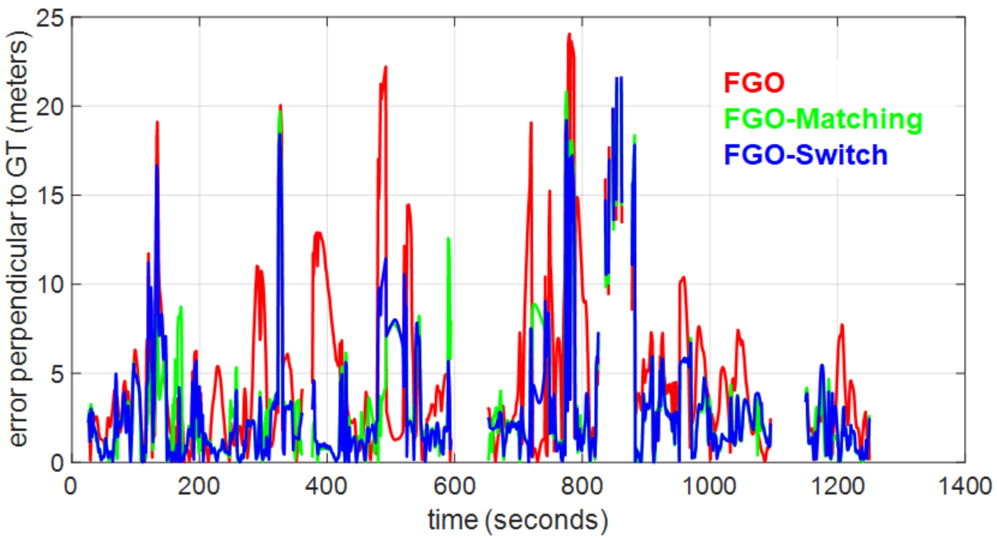

Fig. 4.11. 2D positioning errors perpendicular to the GT direction of the three methods in Dataset 1.

As illustrated in Table 4.4, the RMSE was 6.53 meters, the mean error was 4.67 meters, the STD was 4.56 meters, and the maximum error value was 24.06 meters for the FGO method. In comparison, the FGO-Matching method yielded substantial improvements across all metrics. The RMSE decreased to 4.50 meters, representing a reduction of 31.12%. The mean error correspondingly decreased to 2.98 meters, signifying an improvement of 36.07%. Moreover, the STD, which serves as a statistical indicator of error dispersion, declined to 3.36 meters, denoting an enhancement of 26.29%. The MAX also observed a decrease to 21.38 meters, marking an improvement of 11.15%.

On the other hand, our proposed FGO-Switch method exhibited performance metrics akin to those of the FGO-Matching method. Although the RMSE was marginally higher at 4.51 meters, it still signified a 30.97% improvement over the traditional FGO method. The mean error slightly decreased to 2.95 meters, indicating an improvement of 36.85%. The STD increased marginally to 3.41 meters, yet it still represented an improvement of 25.30% over the FGO method. The maximum error was also slightly larger at 21.68 meters, but it denoted a 9.88% improvement compared to the FGO method.

Table 4.4 Perpendicular errors of all methods in Dataset 1

All Methods	RMSE (m)	MEAN (m)	STD (m)	MAX (m)
FGO	6.53	4.67	4.56	24.06
FGO-Matching	4.50	2.98	3.36	21.38
FGO-Switch	4.51	2.95	3.41	21.68

In summary, FGO-Matching and FGO-Switch methods substantially improve over the conventional FGO method. However, it is pertinent to underscore that the FGO-Switch method demonstrated a minor improvement in mean error when compared to the FGO-Matching method, suggesting its potential for superior accuracy in lane-level localization.

Table 4.5 Perpendicular errors of all methods in Dataset 2

All Methods	RMSE (m)	MEAN (m)	STD (m)	MAX (m)
FGO	10.72	8.38	6.70	27.25
FGO-Matching	7.50	4.84	5.73	25.31
FGO-Switch	7.53	4.91	5.72	25.32

Based on Table 4.5 results, the FGO method yielded an RMSE of 10.72, a mean error of 8.38, a standard deviation of 6.70, and a maximum error of 27.25. In contrast, the FGO-Matching method demonstrated significant improvements in all metrics compared to the conventional FGO method. The RMSE was reduced to 7.50 meters, signifying a decrease of 30.07%. Additionally, the mean error reduced considerably to 4.84 meters, marking a 42.18% improvement. The standard deviation decreased to 5.73

meters, indicating a 14.48% improvement. Similarly, the maximum error experienced a reduction to 25.31 meters, an improvement of 7.10%. The FGO-Switch method showed performance metrics akin to those of the FGO-Matching method. Despite a slight increase in the RMSE to 7.53 meters, it still represented a 29.73% improvement over the FGO method. The MEAN also increased marginally to 4.91 but showed a substantial 41.38% improvement. The standard deviation remained nearly consistent at 5.72 meters, showing a 14.61% improvement, while the maximum error, though marginally higher at 25.32 meters, still represented a 7.08% improvement over the FGO method. Similar to the Dataset 1 result, both the FGO-Matching and FGO-Switch methods significantly supersede the performance of the traditional FGO method across all metrics. However, the marginal difference between the FGO-Matching and FGO-Switch methods suggests comparable effectiveness in reducing the errors perpendicular to the GT.

4.5 Conclusion

This study presents a novel method for enhancing the accuracy of urban GNSS positioning that suffered multi-path effects and NLOS receptions. Our approach integrates multi-epoch human-marked lane information from GE into an FGO-based method as a map, and its efficacy in improving the GNSS positioning performance was validated using two real-world datasets. Furthermore, we introduced a switchable factor to enhance the reliability of map matching. Our results demonstrate that the proposed FGO-Matching and FGO-Switch methods achieved superior positioning accuracy compared to the conventional FGO method in the validated challenging urban environments. Moreover, our approach provides a practical solution for urban road monitoring applications requiring precise positioning data. We observed an increase of approximately 120% in computation time compared to the original algorithm. Despite this increment, the overall efficiency of the algorithm remains within acceptable limits for practical applications. However, when the initial guess is bad, FGO-Switch shows lower robustness than FGO-Matching because a bad initial guess leads to erroneous map-matching. These errors would be integrated into the estimation process and the motion model factor will potentially propagate these errors.

In this chapter, we demonstrated that introducing lane-level map constraints into the FGO formulation can effectively regularize smartphone-based GNSS positioning in complex urban roads, while the switchable-factor mechanism provides an essential safeguard against incorrect lane associations and map inconsistencies. Despite these improvements, the current system is still primarily limited by the information content of the employed measurements and the simplicity of the motion-related constraints. At present, only GPS/BeiDou L1 pseudorange and Doppler are utilized, which restricts measurement redundancy and the attainable accuracy under severe multipath/NLOS conditions. This naturally motivates the next stage of development: extending the observation model to multi-constellation and multi-frequency measurements, and further incorporating carrier-phase observations to strengthen geometry and improve precision. In parallel, integrating IMU/INS into the same factor-graph framework will provide more informative and physically consistent motion constraints, reducing the reliance on simplified motion-model factors and enhancing continuity during GNSS outages. Finally, to support practical deployment, the proposed road-constrained FGO can be reformulated into a real-time sliding-window estimator with marginalization, and can be further augmented by cooperative information sources (e.g., V2X or collaborative positioning) to increase redundancy and reliability in future iterations.

5. ENHANCING GNSS/INS POSITIONING ACCURACY AND ROBUSTNESS IN URBAN ENVIRONMENTS

Building upon the insights from prior research focused on enhancing positioning accuracy, this study introduces a novel post-processing algorithm designed to deliver high-precision positioning solutions for demanding applications such as high-definition mapping. Our system employs a tightly coupled integration of Global Navigation Satellite System (GNSS) and IMU data to achieve robust and accurate state estimation. A key innovation of our post-processing approach lies in the utilization of real-time initial solutions, inspired by the publicly available gici-lib, to guide the subsequent non-linear optimization process. This initialization strategy offers significant mathematical advantages within the optimization framework by enhancing robustness, and mitigates the risk of converging to suboptimal local minima in the non-linear optimization. Furthermore, this study investigates the impact of different measurement weighting models within our post-processing system. We rigorously tested both traditional elevation-based weighting and C/N0-based weighting, leveraging massive GNSS observations to meticulously fit optimal weighting parameters specifically tailored for the unique urban environment of Hong Kong. The resulting optimized weighting model demonstrably enhances positioning performance in this challenging region. Finally, to ensure the credibility and generalizability of our findings, the proposed algorithm has been thoroughly validated using publicly accessible real-world datasets, demonstrating its practical applicability and robustness. The main contributions of this study are summarized as follows:

(1) This study presents an innovative post-processing system that tightly integrates GNSS and IMU measurements, leveraging a real-time initial solution derived from Gici-Lib [111] within a batch non-linear optimization framework. This approach boosts

the measurements redundancy and harnesses the benefits of improved initialization in non-linear optimization, leading to more reliable and accurate state estimation, particularly beneficial for high-precision post-processing applications.

(2) This study provides a comprehensive evaluation of different measurement weighting models within a post-processing context, including elevation-based and C/N0-based strategies. We present empirically optimized weighting parameters specifically fitted for the urban environment of Hong Kong, derived from extensive real-world GNSS data.

(3) The system's efficacy and reliability are rigorously validated using publicly available real-world datasets, confirming its practical applicability and performance in challenging urban canyon scenarios.

5.1 Methodology

5.1.1 System Overview

In this research, we designed a novel post-processing system designed for more accurate urban positioning through the tight integration of Global Navigation Satellite System (GNSS) and IMU data. As Figure 5.1 shows, the system processes pre-collected GNSS and IMU measurements. For the GNSS subsystem, our approach leverages multi-system measurements across dual frequencies, enhancing observation redundancy and robustness. To ensure GNSS measurement quality, satellites with elevation angles below 15 degrees and C/N0 below 20 dB/Hz are excluded from processing. For the IMU pre-integration, we employ a segmented pre-integration strategy. Specifically, IMU measurements within segments anchored by GNSS epochs are pre-integrated to construct IMU pre-integration factors. The detailed formulation of the IMU pre-integration factor within our post-processing framework will be elaborated upon in subsequent sections of this study.

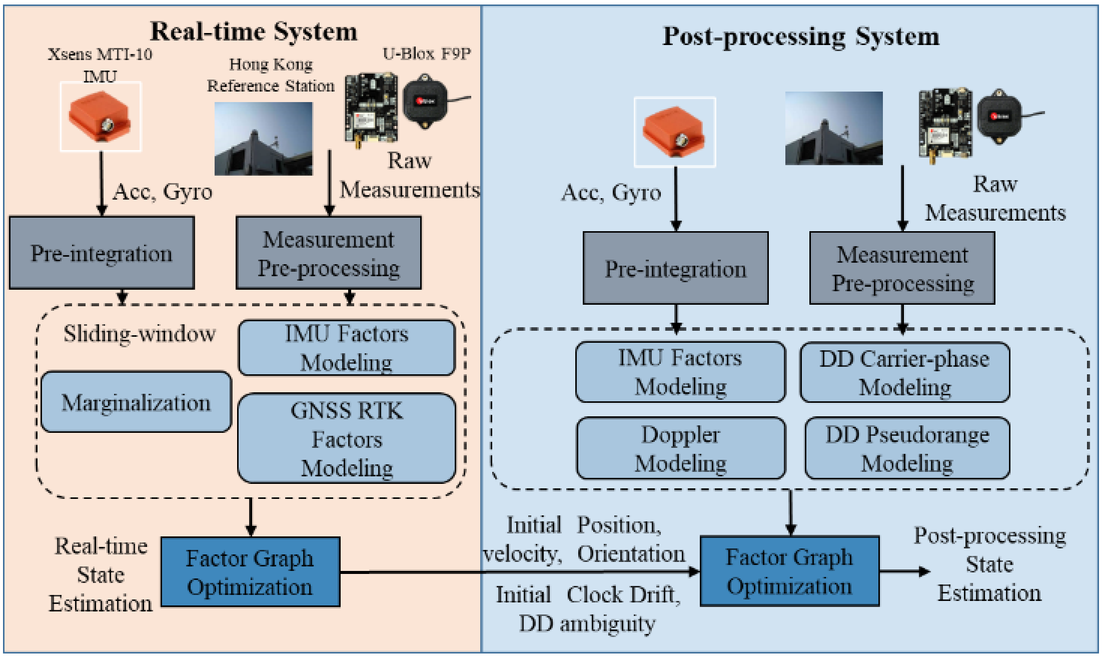

Fig. 5.1. The detailed methodology of the proposed system.

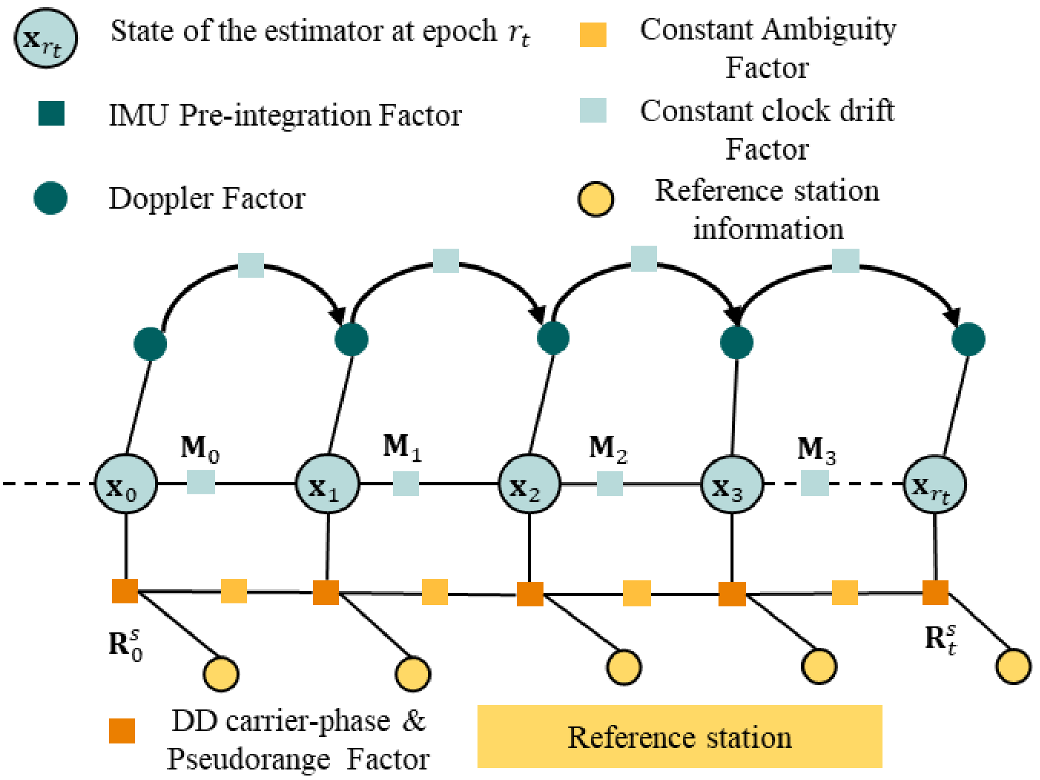

Fig. 5.2. The overview of the proposed system.

Figure 5.2 illustrates the factor graph representation of the proposed post-processing GNSS/INS tightly coupled system, designed for high-accuracy state estimation. Nodes in the graph represent various types of variables, including the state of the estimator at each epoch, constant ambiguity factors (orange squares), constant clock drift factors (blue squares), and reference station information (yellow circles). Edges, or factors, denote different constraints and measurements: IMU pre-integration factors (dark cyan squares) connect states across consecutive epochs, modeling relative transformation using IMU data. Doppler factors (cyan circles) link to each state node, incorporating GNSS Doppler shift measurements; Double-Difference (DD) carrier-phase and pseudorange factors (orange squares) connect to each state node and reference station information nodes, to integrate DD GNSS observations from both the rover and reference stations. Initial state prior information is also incorporated at the initial state node. The factor graph structure unfolds chronologically in the whole sequence, with IMU pre-integration facilitating states propagation. At each epoch, the system fuses GNSS and reference station observations, along with optional initial state priors, to achieve optimal state estimation through factor graph optimization, such as non-linear least squares. Constant ambiguity and clock drift factors enhance the graph's constraint strength, improving the precision and reliability of parameter estimation. This factor graph clearly visualizes the model structure and information fusion of the proposed post-processing system, providing an intuitive framework for understanding and implementing this positioning approach.

The GNSS receiver state set is represented as follows:

$$\boldsymbol{\chi} = \left[\mathbf{x}_{r,0}, \mathbf{x}_{r,1}, \dots, \mathbf{x}_{r,t}\right] \tag{5.1}$$

$$\mathbf{x}_{r,t} = \left(\mathbf{p}_{r,t}, \mathbf{v}_{r,t}, \mathbf{q}_{r,t}, \dot{\boldsymbol{\delta}}_{r,t}, \Delta\nabla\mathbf{N}_{r,t}^{s,j}, \mathbf{ba}_t, \mathbf{bg}_t\right)^T \tag{5.2}$$

where the variable $\boldsymbol{\chi}$ denotes the state set of the GNSS receiver ranging from the first epoch to the current t. $\mathbf{x}_{r,t}$ denotes the state of the GNSS receiver at epoch t which involves the position ($\mathbf{p}_{r,t}$), velocity ($\mathbf{v}_{r,t}$), orientation ($\mathbf{q}_{r,t}$), clock drift $\dot{\boldsymbol{\delta}}_{r,t}$ and DD integer ambiguity ($\Delta\nabla\mathbf{N}_{r,t}^{s,j}$). The DD integer ambiguity will be added the constant ambiguity factor after detecting the absence of cycle slip by loss of lock indicator (LLI).

$\mathbf{ba}_t$ and $\mathbf{bg}_t$ are the bias of the accelerometer and the gyroscope. The clock drift parameter can also be set as equal between two consecutive states. All the The details of the factors will be shown in the following part.

5.1.2 DD pseudorange and carrier-phase factors

In our proposed method, the DD pseudorange and DD carrier-phase factors have been integrated for a more accurate map-matching system in urban canyons.

The DD pseudorange measurement is shown as:

$$\Delta\nabla p_{r,t}^{s} = (\rho_{r,t}^{s} - \rho_{b,t}^{s}) - (\rho_{r,t}^{j} - \rho_{b,t}^{j}) + \Delta\nabla\varepsilon_{r,t}^{s,j} \tag{5.3}$$

where the pseudorange from the closest reference station is denoted by the subscript b. $\Delta\nabla\varepsilon_{r,t}^{s}$ represents the DD pseudorange errors. The DD carrier-phase measurement can be written as:

$$\Delta\nabla\phi_{r,t}^{s} = (\phi_{r,t}^{s} - \phi_{b,t}^{s}) - (\phi_{r,t}^{j} - \phi_{b,t}^{j}) \tag{5.4}$$

$$+\Delta\nabla N_{r,t}^{s,j} + \Delta\nabla\omega_{r,t}^{s,j}$$

where ϕ denotes the carrier-phase measurements, and the sub-scripter r and b denote the measurement from the receiver or the reference station. $\Delta\nabla N_{r,t}^{s,j}$ represents the double difference ambiguity of this satellites pair in the same constellation.

Based on the above models, the cost function of DD pseudorange factors can be written as :

$$\left\|e_{r,k}^{s,DD}\right\|_{\boldsymbol{\Sigma}_{r,t}^{D}}^{2} = \left\|\Delta\nabla p_{r,t}^{s} - h_{r,t}^{s}(\mathbf{p}_{r,t}, \mathbf{p}_{b,t}, \mathbf{p}_{t}^{s}, \mathbf{p}_{t}^{j})\right\|_{\boldsymbol{\Sigma}_{r,t}^{DD}}^{2} \tag{5.5}$$

with $h_{r,t}^{s}(\mathbf{p}_{r,t}, \mathbf{p}_{b,t}, \mathbf{p}_{t}^{s}, \mathbf{p}_{t}^{j}) = \|(|\mathbf{p}_{t}^{j} - \mathbf{p}_{b,t}| - |\mathbf{p}_{t}^{j} - \mathbf{p}_{r,t}|) - (|\mathbf{p}_{t}^{s} - \mathbf{p}_{b,t}| - |\mathbf{p}_{t}^{s} - \mathbf{p}_{r,t}|)\| + \omega_{r,t}^{DD}$, where $\mathbf{p}_{r,t}, \mathbf{p}_{b,t}, \mathbf{p}_t^s, \mathbf{p}_t^j$ represent receiver position, reference station position, satellite s position and satellite j position, respectively. $\mathbf{\Sigma}_{r,t}^{DD}$ is the covariance calculated using satellite elevation angle. For each satellite and the receiver, it would have four covariance matrices, $\mathbf{\Sigma}_{r,t}^{s,DD}$, $\mathbf{\Sigma}_{b,t}^{s,DD}$, $\mathbf{\Sigma}_{r,t}^{j,DD}$, $\mathbf{\Sigma}_{b,t}^{j,DD}$. For the double difference pseudorange factor, the $\mathbf{\Sigma}_{r,t}^{DD}$ can be written as:

$$\mathbf{\Sigma}_{r,t}^{DD} = \left(\mathbf{\Sigma}_{r,t}^{s,DD} + \mathbf{\Sigma}_{b,t}^{s,DD} + \mathbf{\Sigma}_{r,t}^{j,DD} + \mathbf{\Sigma}_{b,t}^{j,DD}\right) \times \alpha \tag{5.6}$$

where α is the weighting ratio of code and phase which is set as 10000.

The cost function of the DD carrier-phase factor is similar to the DD pseudorange except for the ambiguity term which can be written as:

$$\left\| e_{r,k}^{s,DD\phi} \right\|_{\mathbf{\Sigma}_{r,t}^{D}}^2 = \left\| \Delta\nabla\phi_{r,t}^{s} - h_{r,t}^{s}\left(\mathbf{p}_{r,t}, \mathbf{p}_{b,t}, \mathbf{p}_t^s, \mathbf{p}_t^j\right) \right\|_{\mathbf{\Sigma}_{r,t}^{DD\phi}}^2 \tag{5.7}$$

with $h_{r,t}^{s}\left(\mathbf{p}_{r,t}, \mathbf{p}_{b,t}, \mathbf{p}_t^s, \mathbf{p}_t^j\right) =$

$$\left\| \left(\left|\mathbf{p}_t^j - \mathbf{p}_{b,t}\right| - \left|\mathbf{p}_t^j - \mathbf{p}_{r,t}\right|\right) - \left(\left|\mathbf{p}_t^s - \mathbf{p}_{b,t}\right| - \left|\mathbf{p}_t^s - \mathbf{p}_{r,t}\right|\right) \right\|$$

$$+\Delta\nabla N_{r,t}^{s,j} + \omega_{r,t}^{DD}$$

where $\mathbf{\Sigma}_{r,t}^{DD\phi}$ is the covariance matrix for the satellite pair which is similar to the DD pseudorange covariance except the ratio α.

$$\mathbf{\Sigma}_{r,t}^{DD\phi} = \left(\mathbf{\Sigma}_{r,t}^{s,DD} + \mathbf{\Sigma}_{b,t}^{s,DD} + \mathbf{\Sigma}_{r,t}^{j,DD} + \mathbf{\Sigma}_{b,t}^{j,DD}\right) \tag{5.8}$$

The $\Delta\nabla N_{r,t}^{s,j}$ can be decomposed into single difference ambiguity of the same satellite:

$$\Delta\nabla N_{r,t}^{s,j} = \left(\Delta N_{r,t}^{s} - \Delta N_{r,t}^{j}\right) \tag{5.9}$$

Where $\Delta N_{r,t}^{s}$ represents the single difference (SD) ambiguity of satellite s, where $\Delta N_{r,t}^{j}$ is the SD ambiguity of satellite j. If the LLI from the raw RINEX does not indicate the satellite's carrier-phase exists cycle slip, the constant ambiguity factor will be constructed as:

$$\left\| e_{r,k}^{N} \right\|_{\boldsymbol{\Sigma}_{r,t}^{D}}^{2} = \left\| \Delta N_{r,t}^{s} - \Delta N_{r,t-1}^{s} \right\|_{\boldsymbol{\Sigma}_{r,t}^{N}}^{2} \tag{5.10}$$

where $\boldsymbol{\Sigma}_{r,t}^{N}$ is the random walk for SD ambiguity in two consecutive epochs which is set as 0.0001.

Similar to the SD ambiguity, the constant clock drift factor could be written as:

$$\left\| e_{r,k}^{\dot{\boldsymbol{\delta}}} \right\|_{\boldsymbol{\Sigma}_{r,t}^{D}}^{2} = \left\| \dot{\boldsymbol{\delta}}_{r,t} - \dot{\boldsymbol{\delta}}_{r,t-1} \right\|_{\boldsymbol{\Sigma}_{r,t}^{\dot{\boldsymbol{\delta}}}}^{2} \tag{5.11}$$

The clock drift parameter contains four constellations' clock drift, and $\boldsymbol{\Sigma}_{r,t}^{\dot{\boldsymbol{\delta}}}$ is set as a random walk, which is 0.0001.

5.1.3 IMU pre-integration

This section details the mathematical formulation of the IMU pre-integration factor. Inertial Measurement Units are instruments designed to sense the angular velocity and linear acceleration of their own body frame. This measurement is achieved through the integration of accelerometers and gyroscopes, which are fundamental components of IMUs. The raw measurements include acceleration $\hat{\mathbf{a}}^{B}$ and angular velocity $\widehat{\boldsymbol{\omega}}^{B}$ in body frame B. $\mathbf{b_g}$ represents the bias of $\widehat{\boldsymbol{\omega}}^{B}$, $\mathbf{n}_{\omega}$ denotes the additive noise of the acceleration of $\widehat{\boldsymbol{\omega}}^{B}$. $\mathbf{b_a}$ represents the bias of $\hat{\mathbf{a}}^{B}$, $\mathbf{n}_{a}$ denotes the additive noise of the acceleration of $\hat{\mathbf{a}}^{B}$. Taking into account the measurement noise $\mathbf{n}$ and bias $\mathbf{b}$, the measurement of IMU is defined as follows:

$$\widehat{\boldsymbol{\omega}}^{B} = \boldsymbol{\omega}^{B} + \mathbf{bg} + \mathbf{n}_{\omega} \tag{5.12}$$

$$\hat{\mathbf{a}}^{B} = \mathbf{R}^{BW}(\mathbf{a}^{W} - \mathrm{g}^{W}) + \mathbf{ba} + \mathbf{n}_{a} \tag{5.13}$$

$\mathbf{R}^{BW}$ is the rotation matrix from the world frame to the body frame. In GNSS/INS system, the world frame usually denotes East, North, Up (ENU) frame. g^{W} is the constant gravity vector in the world frame. $\mathbf{a}^{W}$represents the noise-free acceleration of the system in the world frame.

Due to the inherent difference in measurement frequencies, GNSS updates occur less frequently compared to IMU measurements. During the interval between two consecutive GNSS measurement epochs, a considerable number of IMU readings are available. IMU pre-integration is employed to efficiently process this high-rate IMU data. It summarizes the motion information from a series of IMU measurements into a single, integrated relative motion constraint, thereby mitigating computational redundancy and lessening the processing load. The t and $t+1$ are assumed to be two consecutive time instants between B_k and B_{k+1}. The angular velocity $\boldsymbol{\omega}$ and the acceleration a between t and $t+\Delta t$ can be expressed as:

$$\boldsymbol{\omega} = \frac{1}{2}\left((\widehat{\boldsymbol{\omega}}^{B_t} - \mathbf{bg}_k) + (\widehat{\boldsymbol{\omega}}^{B_{t+1}} - \mathbf{bg}_k)\right) \tag{5.14}$$

$$\mathbf{a} = \frac{1}{2}\left(\mathbf{q}_{B_t}^{B_k}(\hat{\mathbf{a}}^{B_t} - \mathbf{ba}_k) + \mathbf{q}_{B_{t+1}}^{B_k}(\hat{\mathbf{a}}^{B_{t+1}} - \mathbf{ba}_k)\right) \tag{5.15}$$

the pre-integrated translation $\boldsymbol{\alpha}_{B_{k+1}}^{B_k}$, the velocity $\boldsymbol{\beta}_{B_{k+1}}^{B_k}$, the rotation $\mathbf{q}_{B_{k+1}}^{B_k}$ and between B_k and B_{k+1} can be expressed by the following equations [157, 158]:

$$\boldsymbol{\alpha}_{B_{k+1}}^{B_k} = \boldsymbol{\alpha}_{B_t}^{B_k} + \boldsymbol{\beta}_{B_{k+1}}^{B_k}\Delta t + \frac{1}{2}\mathbf{a}\Delta t^2 \tag{5.16}$$

$$\boldsymbol{\beta}_{B_{k+1}}^{B_k} = \mathbf{a}_{B_t}^{B_k} + \mathbf{a}\Delta t \tag{5.17}$$

$$\mathbf{q}_{B_{k+1}}^{B_k} = \mathbf{q}_{B_t}^{B_k} \otimes \begin{bmatrix} 0 \\ \frac{1}{2}\boldsymbol{\omega}\Delta t \end{bmatrix} \tag{5.18}$$

Therefore, the observation measurements $\mathbf{z}_{B_{k+1}}^{B_k}$ generated by pre-integration can be denoted as:

$$\mathbf{z}_{B_{k+1}}^{B_k\ (IMU)} = \left\{\boldsymbol{\alpha}_{B_{k+1}}^{B_k}, \boldsymbol{\beta}_{B_{k+1}}^{B_k}, \mathbf{q}_{B_{k+1}}^{B_k}, \mathbf{ba}_{k+1}, \mathbf{bg}_{k+1}\right\} \tag{5.19}$$

the residual for IMU pre-integration between two IMU states can be defined as:

$$\mathbf{e}_{r,t}^{\mathrm{I}}\left(\mathbf{z}_{B_{k+1}}^{B_k}{}^{(IMU)},\chi\right)=\begin{bmatrix}\mathbf{r}_p\\\mathbf{r}_v\\\mathbf{r}_q\\\mathbf{r}_{ba}\\\mathbf{r}_{bg}\end{bmatrix}=\begin{bmatrix}\mathbf{q}_{B_k}^{W\ -1}\begin{pmatrix}\mathbf{p}_{B_{k+1}}^{W}-\mathbf{p}_{B_k}^{W}-\mathbf{v}_{B_k}^{W}\Delta t\\-\frac{1}{2}\mathbf{g}^{W}\Delta t^2\end{pmatrix}-\boldsymbol{\alpha}_{B_{k+1}}^{B_k}\\\mathbf{q}_{B_k}^{W\ -1}\left(\mathbf{v}_{B_{k+1}}^{W}-\mathbf{v}_{B_k}^{W}-\mathbf{g}^{W}\Delta t\right)-\boldsymbol{\beta}_{B_{k+1}}^{B_k}\\2\left[\mathbf{q}_{B_{k+1}}^{B_k}{}^{-1}\otimes\left(\mathrm{q}_{B_k}^{W\ -1}\otimes\mathbf{q}_{B_{k+1}}^{W}\right)\right]_{xyz}\\\mathbf{ba}_{k+1}-\mathbf{ba}_k\\\mathbf{bg}_{k+1}-\mathbf{bg}_k\end{bmatrix} \tag{5.20}$$

where $[\cdot]_{xyz}$ is used for extracting the imaginary part of a quaternion. Where the $\otimes$ denotes multiplication between two different quaternions. The covariance of the IMU pre-integration factor $\boldsymbol{\Sigma}_{r,t}^{I}$ can be derived from Gici-Lib [111]

Non-linear optimization for factors

$$\chi^*=\underset{\chi}{argmin}\sum\left(\left\|e_{r,k}^{s,DD}\right\|_{\boldsymbol{\Sigma}_{r,t}^{D}}^{2}+\left\|e_{r,k}^{s,DD\phi}\right\|_{\boldsymbol{\Sigma}_{r,t}^{D}}^{2}+\left\|e_{r,k}^{s,D}\right\|_{\boldsymbol{\Sigma}_{r,t}^{D}}^{2}\right.$$

$$\left.+\left\|\mathbf{e}_{r,t}^{\mathrm{I}}\right\|_{\boldsymbol{\Sigma}_{r,t}^{I}}^{2}+\left\|e_{r,k}^{\dot{\boldsymbol{\delta}}}\right\|_{\boldsymbol{\Sigma}_{r,t}^{D}}^{2}+\left\|e_{r,k}^{N}\right\|_{\boldsymbol{\Sigma}_{r,t}^{D}}^{2}\right) \tag{5.21}$$

The variable χ^* denotes the optimal estimation of the system state sets. The Ceres Solver [159] is employed as a non-linear optimization solver to solve the above objective function.

5.2 Experiments Setup

To validate the effectiveness of our proposed methodology, we conducted experiments using two real-world datasets. The first dataset was obtained from the "medium urban" portion of the publicly available UrbanNav [103] dataset. UrbanNav is an open-sourced multisensory dataset designed for benchmarking positioning algorithms in challenging urban environments (e.g., urban canyons) in Hong Kong. It provides synchronized measurements from multi-frequency GNSS receivers (including raw GNSS RINEX data), IMU, and additional sensors such as LiDAR and cameras, together with high-accuracy reference trajectories for evaluation (e.g., from a SPAN-CPT system). The dataset contains scenarios with different levels of difficulty, and the “medium urban” subset used in this study reflects representative real-world urban traffic conditions with frequent environmental dynamics (e.g., moving vehicles, buses, and pedestrians), thereby implicitly incorporating the effects of dynamic obstacles into the evaluation. This segment represents a challenging urban environment where GNSS signals are prone to multipath effects and NLOS reception. The second dataset was derived from the open-source Pyrtklib dataset [160], which corresponds to a slight urban environment. This environment is characterized by lower building heights and a reduced prevalence of NLOS and multipath phenomena. The GNSS receiver is u-blox F9P with the patch antenna. This study utilized all the GNSS system GPS/BeiDou/GLONASS/GALILEO measurements at a frequency of 1 Hz. The ground truth (GT) is provided by the NovAtel SPAN-CPT. The FOG's gyro bias in-run stability is 1 degree per hour, with a random walk of 0.067 degrees per hour. Before the experiments, the coordinate systems between all sensors were calibrated.

5.2.1 C/N0 with the time of all the used satellites

Figure 5.3 illustrates the C/N0 value changes over time in medium urban dataset. In medium urban, the signal reflection and blockage occur frequently, which will be reflected in the satellite's C/N0, so observing the change in C/N0 over time can reflect the quality of the satellite signal at a given time. The GNSS C/N0 all fluctuate around 30-35 dB/Hz. However, many times the visibility of the satellites drops drastically due to building occlusion, reliable localization in such scenarios is very challenging.

Figure 5.4 illustrates the C/N0 value changes over time in the slight urban dataset. In general, the C/N0 values for most satellites appear to be within 30-40 dB/Hz for robust GNSS positioning, although variations and potential signal strength differences between individual satellites and across different satellite constellations are evident. In short, these two figures demonstrate that satellite signals in slight urban areas are healthier than the signals in medium urban.

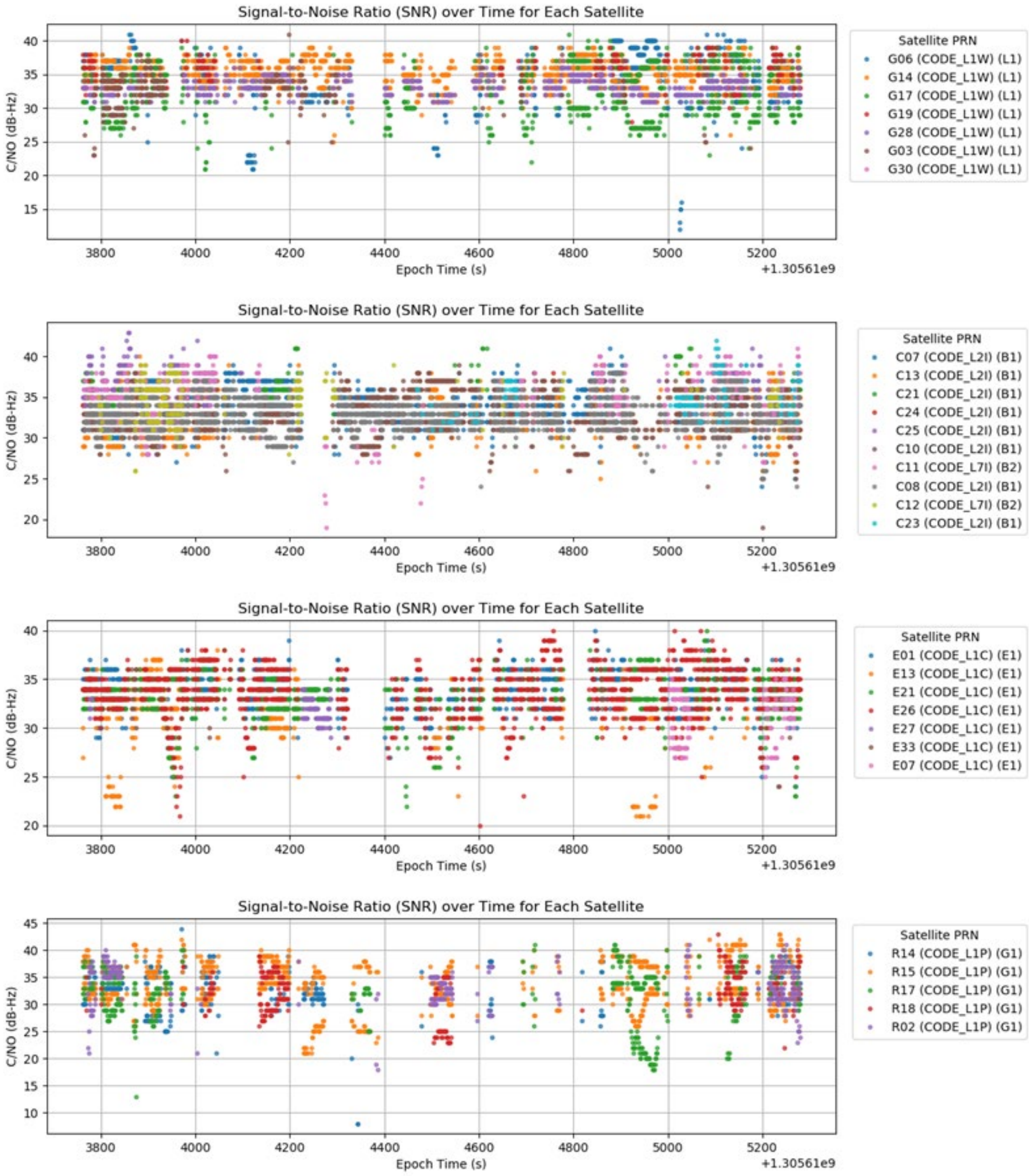

Fig. 5.3. C/N0 over time for all the GNSS constellations in medium urban.

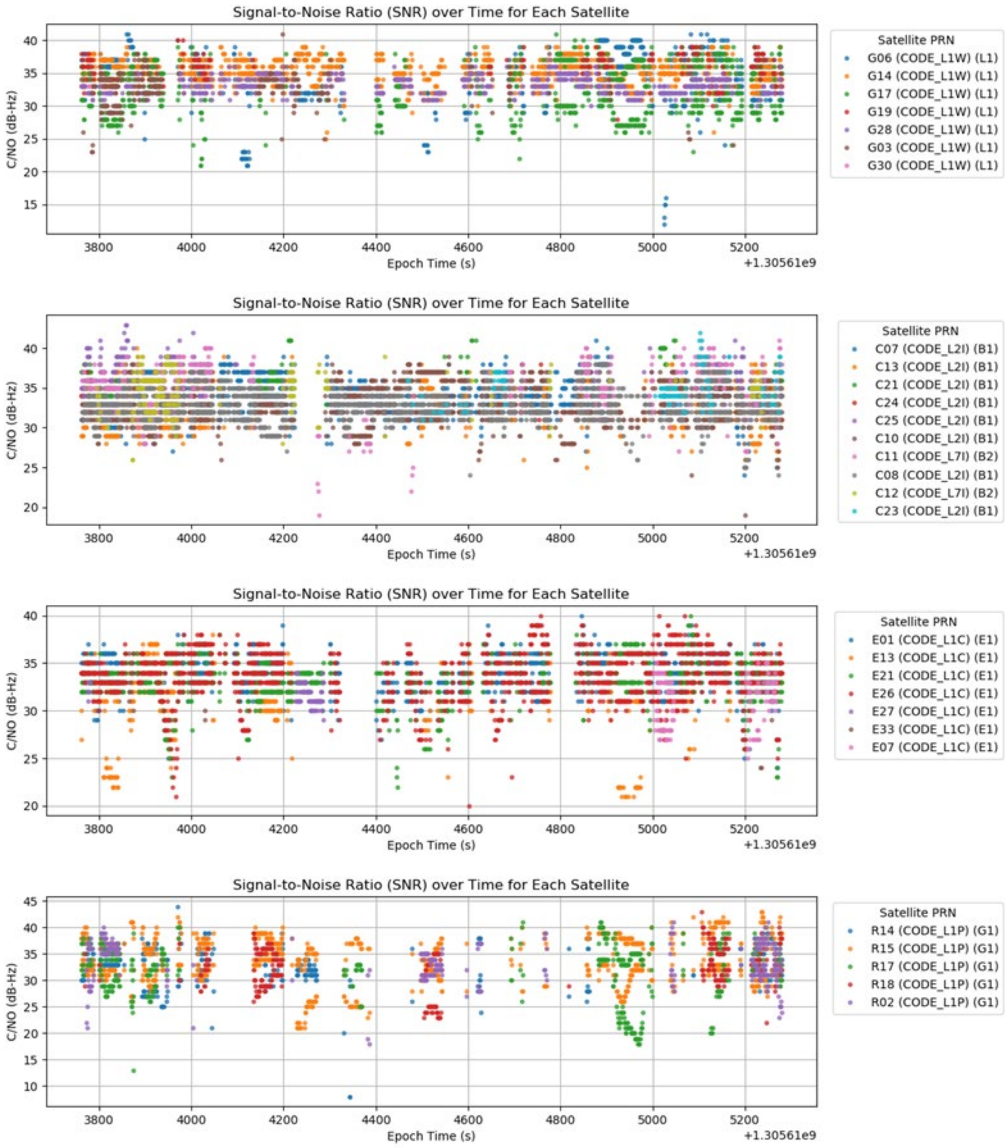

Fig. 5.4. C/N0 over time for all the GNSS constellations in slight urban.

5.2.2 Evaluation Methods

The objective of this part was to validate the effectiveness of the proposed method in improving positioning performance. The accuracy is evaluated in the ENU frame by selecting the first point in the ground truth as the reference position. Both of these estimators are post-processing systems. The metrics include Root Mean Square Error (RMSE), Mean Error(Mean), and Standard Deviation (STD).

(1) Gici-Lib [111]: Open-source SOTA Real-time FGO-based RTK/INS positioning solution. In this study, we set the sliding-window as 8 for real-time estimation.

(2)Post-processing RTK/INS FGO system (**PP-RTK/INS**): The first proposed method. Post-processing FGO-based RTK/INS positioning solution. Compared to the Gici-Lib, the sliding window approach inherent in has been substituted with an infinite sliding window configuration operating in a post-processing regime. Moreover, the marginalization part has been omitted from the processing pipeline. With these specified modifications, the remaining part adhere to the established conventions of the original Gici-Lib framework. Furthermore, we leverages the Gici-Lib solution to generate an improved initial solution for the system.

(3) Post-processing RTK/INS with C/N0-based weighting method (**PP-RTK/INS-W**): The second proposed method. Post-processing FGO-based RTK/INS positioning solution. In addition to expanding the sliding window to infinity and integrating the SOTA solution as an initial guess, we also introduce a novel weighting model [131] specifically optimized for urban scenarios. This model, derived through fitting against measurements from both static and dynamic u-blox F9P receivers and validated against ground truth data collected in urban settings, is engineered to more effectively mitigate positioning errors arising from multipath effects and NLOS signal reception.

In both of these datasets, the Gici-Lib get 0% fix rate, so in this study we only consider the float solutions for comparison.

5.3 RESULTS

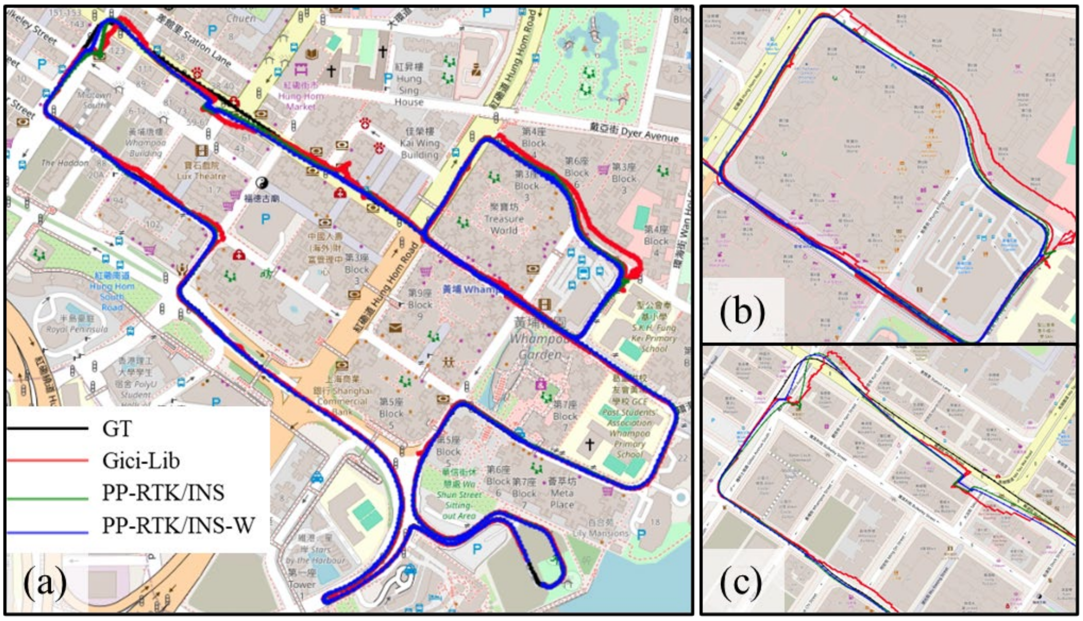

Fig. 5.5. Proposed method trajectory with the GT.

Figure 5.5 compares the estimated trajectories in the East-North-Up (ENU) frame, encompassing the Ground Truth (GT) trajectory, the trajectory estimated by the Gici-Lib method, the trajectory of PP-RTK/INS, and the trajectory derived from the PP-RTK/INS-W. As depicted in Figure 5-(a), the GT trajectory is represented by a black line, serving as the benchmark for comparison. The trajectory estimated by the Gici-Lib method is shown in red, the PP-RTK/INS trajectory in green, and the PP-RTK/INS-W 's trajectory in blue. Observation of Figure 5-(a) reveals that the Gici-Lib trajectory exhibits noticeable deviations from the GT trajectory across the entire test route, and in several instances, diverges significantly from the actual road path. In contrast, the PP-RTK/INS-W demonstrates a considerably closer alignment with the GT trajectory, indicating enhanced accuracy in trajectory estimation. The PP-RTK/INS trajectory appears to offer some improvement over the original Gici-Lib but still exhibits more deviation compared to the PP-RTK/INS-W, particularly in areas with sharp turns and complex road geometries. Figures 5-(b) and 5-(c) provide zoomed-in views of specific sections, further highlighting the performance differences. These magnified views underscore the superior trajectory estimation accuracy achieved by the PP-RTK/INS-W, especially in challenging driving scenarios, while also illustrating the limitations of the Gici-Lib method and the incremental improvements offered by PP-RTK/INS. The observed deviations in the Gici-Lib trajectory, especially its tendency to stray from the road, likely stem from its potentially limited capability in handling NLOS reception and multi-path. Conversely, the PP-RTK/INS-W, through its refined approach, appears to mitigate these limitations with the C/N0-based weighting method, resulting in a more robust and accurate trajectory estimation performance

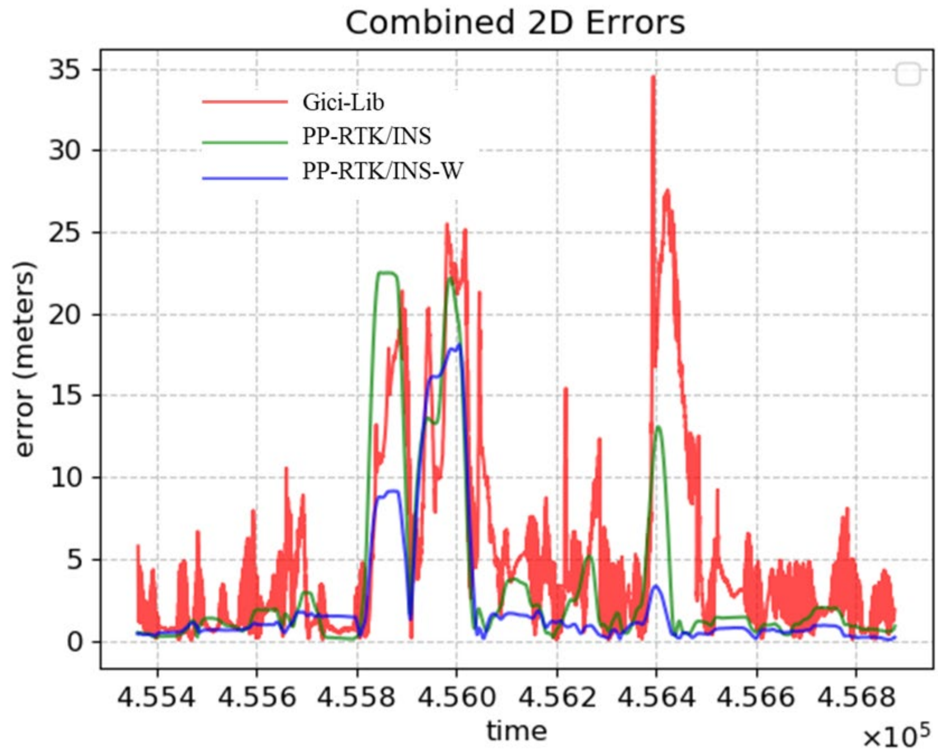

Fig. 5.6. 2D Errors of evaluated methods

Building upon the trajectory analysis presented in Figure 5.5, Figure 5.6 provides a quantitative evaluation of the estimator performance by illustrating the Combined 2D Errors over time for the Gici-Lib method, PP-RTK/INS, and PP-RTK/INS-W. Specifically, Figure 5.6 displays a time-series plot of the 2D positioning errors in meters (Y-axis) against time (X-axis), allowing for a direct comparison of the error characteristics of each method across the duration of the experiment. Examination of

Figure 5.6 reveals that the PP-RTK/INS-W consistently exhibits the lowest 2D errors throughout the majority of the time series, demonstrating superior accuracy compared to both the Gici-Lib and PP-RTK/INS methods. In contrast, the Gici-Lib method displays significantly larger error magnitudes, frequently exceeding 10 meters and peaking above 30 meters in certain time intervals. The PP-RTK/INS method offers a noticeable reduction in errors compared to the original Gici-Lib, but its error levels generally remain higher than those of the PP-RTK/INS-W, particularly during periods of rapid error fluctuations. Notably, within specific time segments, such as around the time point of 4.559 and 4.565 on the x-axis, the PP-RTK/INS-W demonstrates significantly reduced error peaks compared to both Gici-Lib and PP-RTK/INS. This observation further substantiates the enhanced robustness of the PP-RTK/INS-W in mitigating error spikes and maintaining a more stable and accurate positioning performance even under dynamically challenging conditions. These error characteristics, depicted in Figure 6, corroborate the trajectory visualizations presented in Figure 5, where the PP-RTK/INS-W's trajectory demonstrated a closer adherence to the Ground Truth trajectory and remained consistently within the road boundaries, while the Gici-Lib method exhibited larger deviations and instances of drifting off-road. The quantitative error analysis in Figure 6 thus provides compelling evidence for the superior performance of the PP-RTK/INS-W in terms of both trajectory accuracy and error magnitude reduction. The merits of the PP-RTK/INS-W are threefold. First, we maximized the window range, leading to significantly enhanced measurement redundancy. This heightened redundancy provides richer data support for trajectory estimation, effectively smoothing the estimated trajectory and mitigating the impact of noise and uncertainties. Second, we employed the Gici-Lib solution as the initial value for nonlinear optimization. This strategy is of paramount importance in nonlinear optimization, primarily because a well-chosen initial value accelerates the convergence of optimization algorithms and effectively aids in avoiding local minima. Particularly in complex nonlinear problems like GNSS positioning, a good initial value guides the optimization process to converge more rapidly and robustly towards the global optimum, thereby improving the accuracy and efficiency of the solution. Third, our tests on the urbannav dataset revealed that in scenarios resembling medium urban areas, relying solely on satellite elevation angles to differentiate Non-Line-of-Sight (NLOS) and multipath effects is limited in effectiveness. Without integrating accurate 3D city models to precisely identify NLOS satellites, elevation angle models alone may fail to effectively suppress outliers. However, our test results in medium urban areas demonstrably show that our integrated C/N0-based weighting method is highly effective in mitigating outlier interference in such scenarios, leading to significant improvements in positioning performance.

TABLE 5.1. COMPARISON OF EVALUATED METHODS

All Methods	**RMSE (m)**	**MEAN (m)**	**STD (m)**
Gici-Lib	8.25	5.39	6.25
PP-RTK/INS	6.63	3.55	5.60
PP-RTK/INS-W	4.62	2.28	4.02

Table 5.1 summarizes the performance comparison across three positioning methods: Gici-Lib, PP-RTK/INS, and the PP-RTK/INS-W. The table presents RMSE, MEAN, and STD for each method, all measured in meters. Gici-Lib has an RMSE of 8.25 meters, which is higher than PP-RTK/INS's 6.63 meters, and significantly higher than the PP-RTK/INS-W's 4.62 meters. In terms of STD, Gici-Lib has a higher variability at 6.25 meters compared to PP-RTK/INS (5.60 meters) and the PP-RTK/INS-W (4.02 meters), which demonstrates superior consistency. Collectively,

these metrics indicate that the PP-RTK/INS-W offers the best performance in terms of accuracy and consistency among the three methods.

Figure 5.7 illustrates a comparative performance analysis of estimated trajectories in a benign urban scenario. This analysis encompasses the GT trajectory, the raw Gici-Lib solution, the post-processed Gici-Lib solution, and the PP-RTK/INS-W. The GT trajectory, serving as the benchmark, is depicted in black. Trajectories derived from the raw Gici-Lib method, the post-processed Gici-Lib, and the PP-RTK/INS-W are represented in red, green, and blue, respectively.

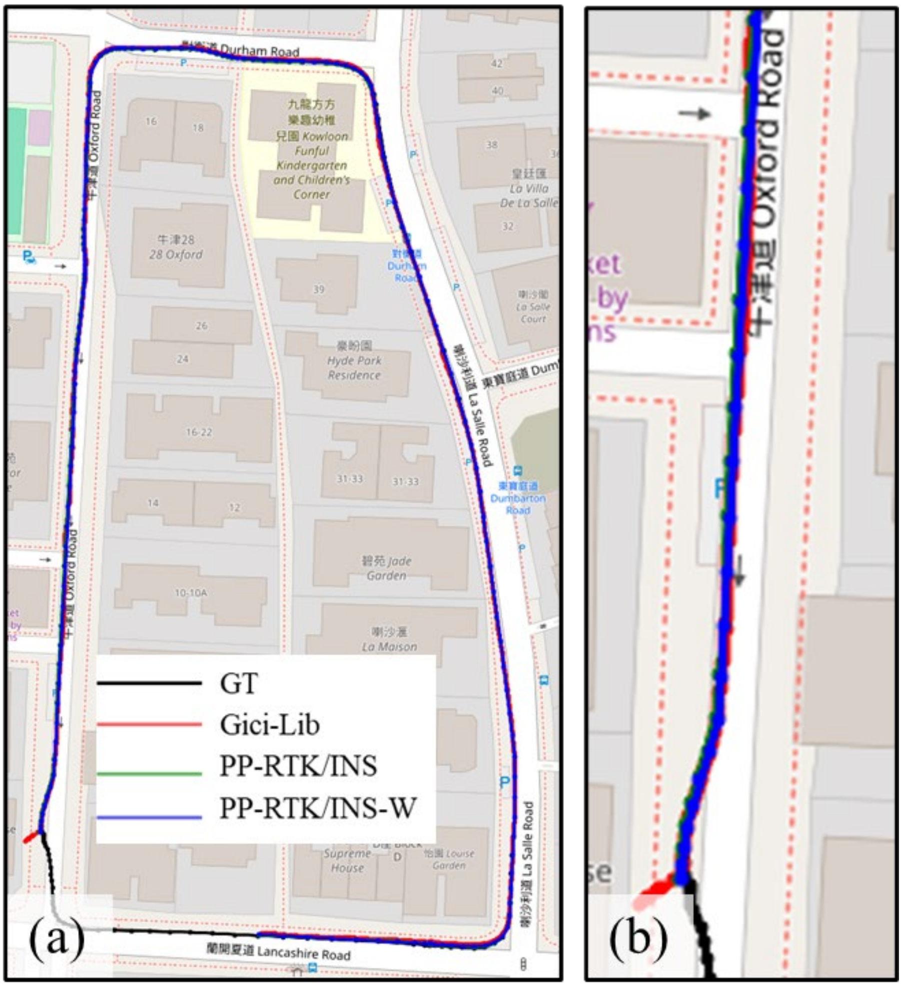

Fig. 5.7. Proposed method trajectory with the GT.

Upon examining Figure 5.7-(a), it is evident that all three methods demonstrate a reasonable proximity to the ground truth in a slight urban environment. Nevertheless, discernible performance variations exist. The Gici-Lib method exhibits commendable accuracy along straight segments but experiences noticeable deviations in curves and at intersections. PP-RTK/INS and PP-RTK/INS-W significantly mitigates these discrepancies through optimization, subtle divergences persist. Figure 5.7-(b) presents a magnified view of a specific road segment, enabling a more granular assessment of performance nuances. The PP-RTK/INS-W maintains a tight alignment with the GT trajectory in localized areas, especially during stationary periods, demonstrating superior stability and consistency. Conversely, Gici-Lib method exhibits slightly more pronounced deviations in these regions, suggesting potential areas for refinement in handling intricate environments.

Figure 5.8 illustrates a comparison of 2D positioning errors for three methods in a mild urban environment. As depicted, in the initial phase of the time series, the post-processed Gici-Lib method (green line) exhibits a performance in error level that is close to, or even slightly better than, the PP-RTK/INS-W (blue line) at certain instances. However, as time progresses, particularly in the later phase of the figure, the PP-RTK/INS-W begins to demonstrate a distinct advantage, consistently maintaining the lowest and most stable error levels. It is noteworthy that at the end of the figure, the raw Gici-Lib method (red line) shows a significant error spike, while the post-processed Gici-Lib method, alttuhough improved, still experiences an increase in error. In contrast, the PP-RTK/INS-W effectively suppresses this error surge, demonstrating superior robustness. Therefore, considering the overall performance across the entire time series, the PP-RTK/INS-W exhibits more superior positioning performance in a mild urban environment, especially when facing potential error disturbances.

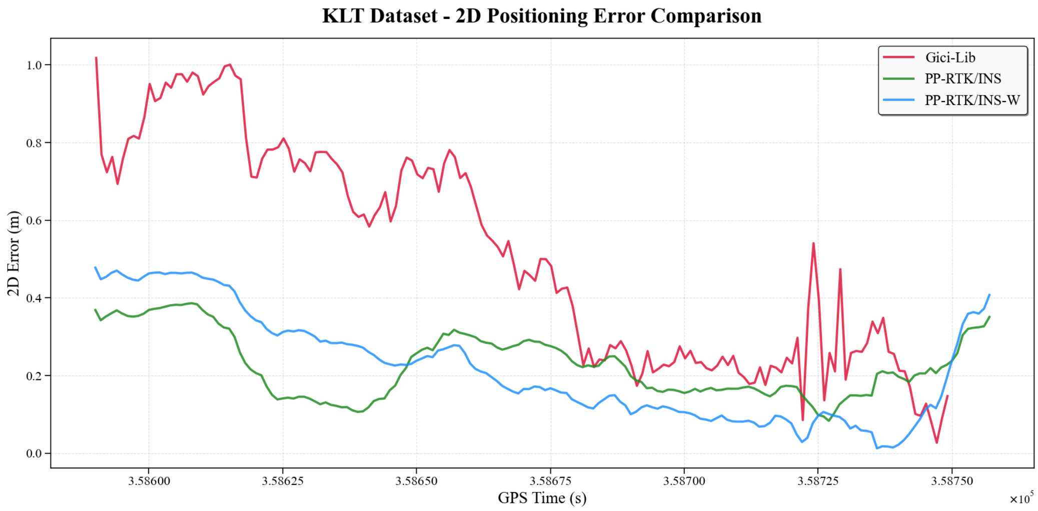

Fig. 5.8. 2D erros of three evaluated methods.

TABLE 5.2. COMPARISON OF EVALUATED METHODS

All Methods	RMSE (m)	MEAN (m)	STD (m)
Gici-Lib	0.70	0.55	0.44
PP-RTK/INS	0.24	0.23	0.08
PP-RTK/INS-W	0.26	0.22	0.14

Table 5.2 presents a comparative analysis of three methods. For Gici-Lib, The RMSE of 0.70 m indicates a significant deviation between predicted and actual values, while the MEAN of 0.55 m suggests an overall systematic bias in its predictions. A standard deviation (STD) of 0.44 m highlights high variability in its errors. PP-RTK/INS shows substantial improvements across all metrics. With an RMSE of 0.24 m, it demonstrates much better accuracy compared to the baseline method. The MEAN error of 0.23 m suggests minimal systematic bias, and a very low STD of 0.08 m indicates highly consistent performance. Our PP-RTK/INS-W achieves an RMSE of 0.26 m, which is slightly higher than PP-RTK/INS but still competitive. The MEAN error of 0.22 m is the smallest among all methods, indicating that this method has the least systematic bias in its predictions. However, its STD of 0.14 m is higher than PP-RTK/INS, suggesting slightly more variability in its errors. In summary, while the PP-

RTK/INS-W does not achieve the lowest RMSE or STD values, it exhibits superior performance in terms of minimizing systematic bias (as evidenced by the smallest MEAN error). This makes it particularly valuable for applications where reducing overall trajectory prediction bias is critical. The PP-RTK/INS method, with its balanced combination of low RMSE and STD, represents a strong alternative, though it sacrifices slightly more bias than the PP-RTK/INS-W.

5.4 Discussion

5.4.1 Similar Results in Slight Urban Area

The similar performance observed between the PP-RTK/INS-W and PP-RTK/INS in slight urban environments can be attributed to several factors. Both methods share the fundamental goal of enhancing trajectory estimation by strategically leveraging satellite signal quality metrics, albeit through different approaches – the PP-RTK/INS-W utilizing C/N0 and PP-RTK/INS employing satellite elevation angles. Specifically, in slight urban settings where obstacles can induce partial signal degradation through blockage or reflection, both techniques effectively mitigate these issues; the PP-RTK/INS-W prioritizes stronger, less noisy signals using C/N0, while PP-RTK/INS strategically avoids lower quality signals from low-elevation satellites more susceptible to interference. Furthermore, the relatively stable availability of satellites and signal conditions in light urban areas contributes to this balanced performance, allowing both methods to operate effectively. Adding to this, the complementary strengths of C/N0-based signal quality assessment and satellite elevation angle-based geometric configuration often align in their effectiveness within these environments, resulting in comparable outcomes. Ultimately, extensive parameter tuning and optimization applied to both methods likely further contribute to their performance parity in controlled, moderately challenging light urban scenarios. In essence, despite their differing underlying models, both the PP-RTK/INS-W and PP-RTK/INS demonstrate effectiveness in improving trajectory estimation within light urban environments by focusing on signal quality and adapting to these moderate environmental challenges.

5.4.2 Potential Fault Detection and Exclusion

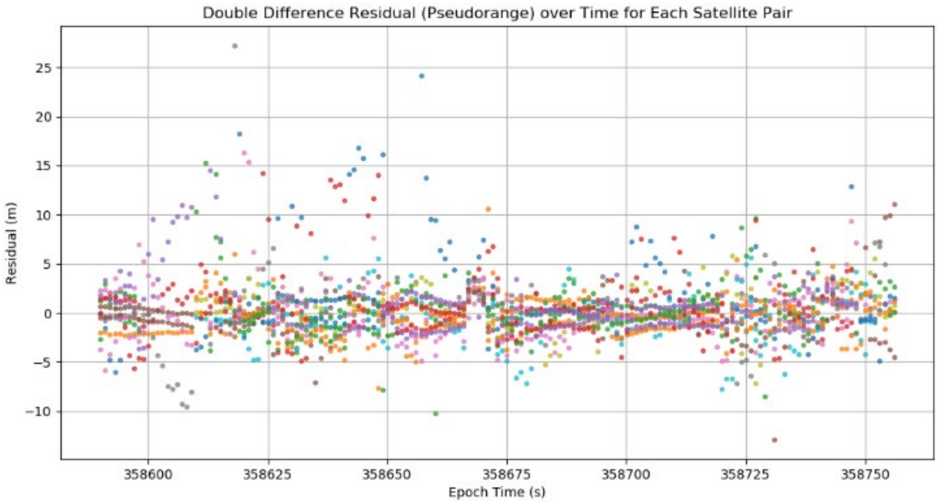

Fig. 5.9. GPS Double Difference pseudorange residuals over time (GNSS seconds).

Figure 9 illustrates the double difference pseudorange residuals over time for each satellite pair (GPS system), obtained in a specific GNSS measurement scenario. The x-axis represents the epoch time in seconds, while the y-axis shows the residual magnitude in meters. Each data point, distinguished by color, corresponds to a double difference pseudorange residual from a unique satellite pair at a given epoch. As depicted, the majority of residuals cluster around zero, indicating effective error mitigation by double differencing. However, the plot also reveals the presence of notable outliers, particularly in the positive direction, reaching magnitudes up to 25 meters. These outliers, scattered across the time series, suggest the existence of unmodeled errors or measurement anomalies. The visual pattern of residuals in this figure highlights the potential benefits of employing Fault Detection and Exclusion (FDE) methods to enhance the GNSS solution. Techniques such as threshold-based outlier removal, Receiver Autonomous Integrity Monitoring (RAIM), or robust estimation could effectively identify and mitigate these large residuals, leading to improved positioning accuracy and robustness by excluding or down-weighting these faulty measurements. This figure underscores the necessity for and potential effectiveness of FDE strategies in addressing residual errors beyond those mitigated by standard double differencing techniques.

5.4.3 Learning-Based GNSS Epoch Health Assessment for Robust Batch FGO

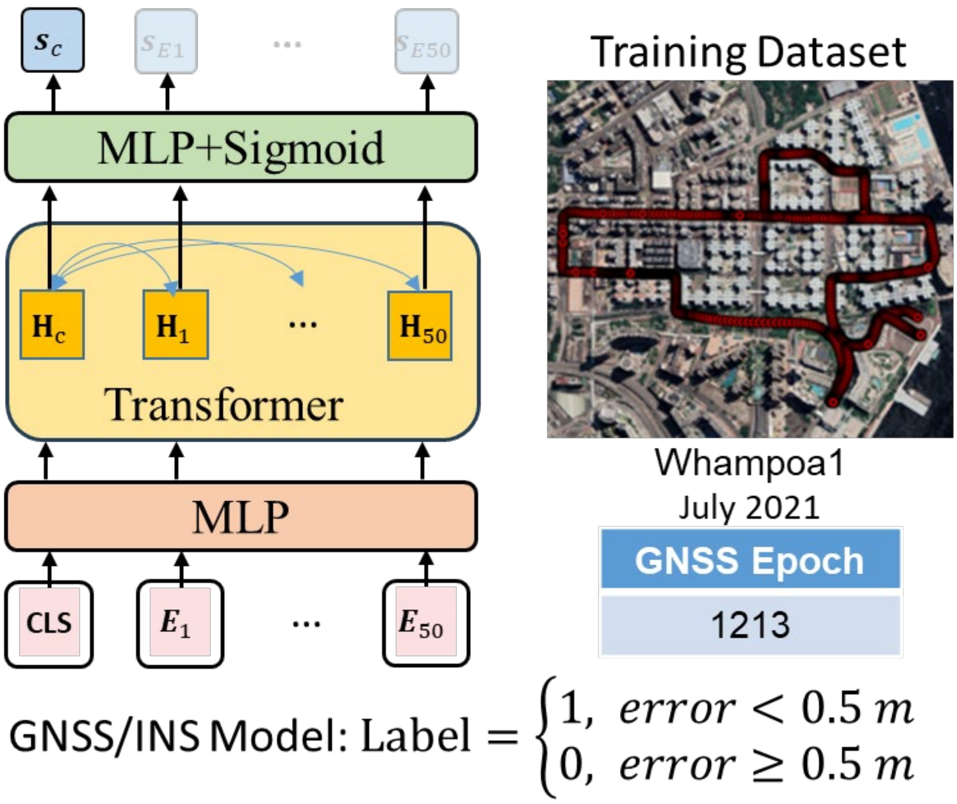

Fig. 5.10. Overview of the proposed model for state classification

This study aims to develop a high-precision post-processing GNSS/INS positioning system tailored for urban-canyon environments. In the proposed framework, multi-constellation dual-frequency GNSS measurements are tightly coupled with a low-cost IMU through batch factor graph optimization (FGO), and measurement robustness is further improved via optimized weighting schemes based on C/N0 and satellite elevation. Nevertheless, in dense urban areas, double-difference pseudorange residuals may still exhibit severe outliers with magnitudes of tens of meters, indicating that traditional threshold-based screening alone is insufficient to fully suppress abnormal observations.

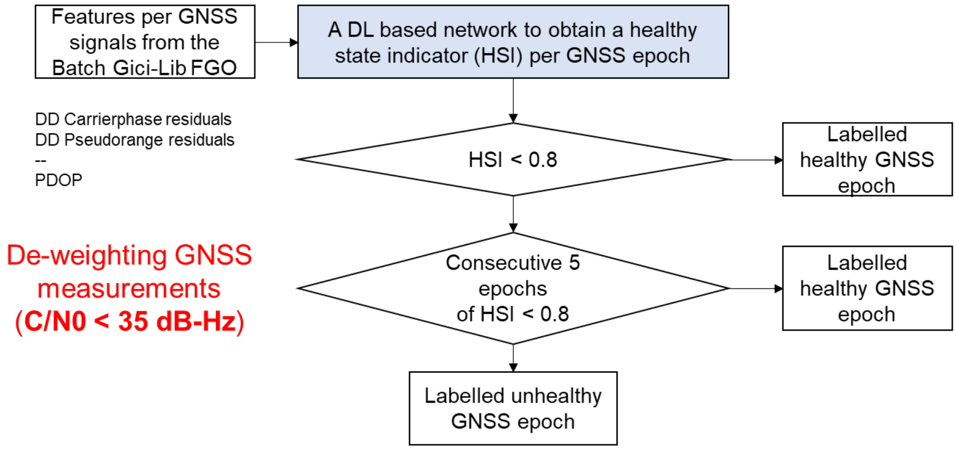

Fig. 5.11. Flow chart of the proposed classifier

To address this issue without fundamentally changing the original optimization backbone, we introduce a deep-learning-based “epoch health” classifier as a second-layer Fault Detection and Exclusion (FDE) module (see Figure 5.11). Specifically, after the first-layer batch FGO, per-epoch features are extracted, including double-difference pseudorange residuals, double-difference carrier-phase residuals, and PDOP. These features are fed into a Transformer with MLP network that outputs a Healthy State Indicator (HSI); the network architecture is illustrated in Figure 5.10. When HSI remains below a preset threshold for consecutive epochs (e.g., HSI < 0.8 for 5 consecutive epochs), the corresponding GNSS epoch is labeled as unreliable. In the second-layer batch FGO, GNSS factors associated with the detected unreliable epochs—pseudorange, carrier-phase, and Doppler—are down-weighted or excluded. In addition, signals with low carrier-to-noise density ratio (e.g., C/N0 < 35 dB-Hz) are also de-weighted to reduce the impact of poor-quality measurements, thereby preventing abnormal observations from dominating the global solution.

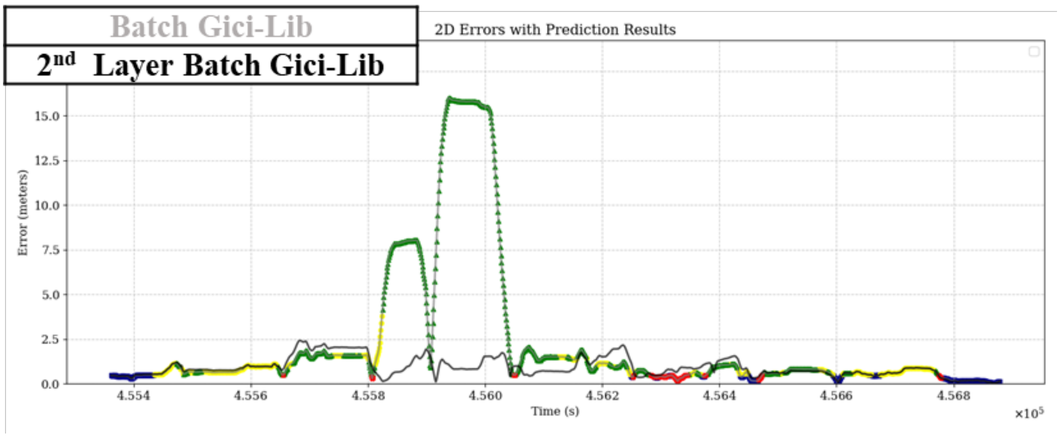

Fig. 5.12. Error of the proposed algorithm with time in UrbanNav Deep dataset

Compared with conventional single-indicator weighting strategies, the proposed AI-based epoch classifier leverages post-optimization residual patterns as learning signals, enabling epoch-level identification of time periods that are heavily affected by blockage and multipath. Figure 5.12 shows that on the UrbanNav Deep test set, the proposed two-layer batch FGO reduces the mean horizontal positioning error from 2.21 m to 0.91 m and decreases CEP95 from 15.16 m to 2.04 m (see Table 5.3).

TABLE 5.3. COMPARISON OF EVALUATED METHODS

Methods	MEAN(m)	CEP 68 (m)	CEP 95 (m)
Real-time Gici-Lib	5.39	4.81	21.6
Batch Gici-Lib	2.21	1.15	15.16
2nd Layer Batch Gici-Lib	**0.91**	**0.96**	**2.04**

In suburban scenarios, the performance difference between the two-layer approach and the conventional batch FGO is marginal, suggesting that the proposed module is most beneficial in harsh urban conditions with frequent abnormal observations. It should be noted that false alarms (misclassifying healthy epochs as unhealthy) may weaken constraints and degrade observability, whereas missed detections may allow faulty measurements to persist; moreover, the HSI threshold and consecutive-epoch rule may require re-calibration under different sampling rates and environments; finally, since the training labels are derived from a specific reference solution, cross-region generalization may require additional data or self-/semi-supervised learning strategies.

5.5 Conclusions And Future Work

This study presents a novel post-processing RTK/INS system for improving the accuracy of urban positioning. Our proposed methods employs the factor graph framework with a non-linear optimization process for robust state estimation in the urban canyon. We observed about 50% improvement in medium urban dataset after we maximize the measurements redundancy and integrating the C/N0-based weighting model for better urban positioning. In the slight urban dataset, we can observe that the mean error has decreased about 70% compared to the Gici-Lib.

This chapter further strengthens the proposed FGO-based positioning framework by exploiting the carrier-phase information and demonstrating its potential for high-precision localization under urban conditions. While the results confirm the benefit of phase-related constraints, residual analysis—particularly on double-difference terms—also indicates that occasional outliers still persist, which may limit robustness in harsh multipath/NLOS scenarios. A natural next step is therefore to incorporate dedicated Fault Detection and Exclusion (FDE) mechanisms to systematically identify and mitigate such abnormal measurements within the factor-graph optimization. In addition, pursuing integer ambiguity resolution will be a key pathway toward centimeter-level precision and faster convergence, building directly upon the formulation and experimental insights established in this chapter. With these findings and remaining challenges clarified, the next chapter concludes this thesis by summarizing the overall contributions and highlighting the broader implications of the proposed methodology.

6. CONCLUSIONS AND FUTURE WORK

Urban GNSS positioning, critical for smart city initiatives, suffers from NLOS and multipath in urban canyons, hindering accuracy for applications such as infrastructure monitoring and traffic management. To combat this, we propose an innovative solution: a multi-sensor fusion framework with factor graph optimization. This approach demonstrably enhances performance across key urban applications, including pedestrian navigation, vehicle trajectory estimation, and high-precision mapping.

To address the perceptual-layer limitations in pedestrian positioning accuracy within urban canyon environments, this research innovatively integrates data from smartphone-embedded MEMS-IMUs and PDR techniques, establishing a tightly-coupled factor graph optimization framework. Experimental results demonstrate that this approach significantly reduces the MEAN of pedestrian positioning to 40% of that achieved by the traditional EKF-PDR method in urban canyon settings. This perceptual-layer innovation not only leverages PDR-based inertial navigation to effectively compensate for GNSS signal outages, but more critically, enhances the robustness and reliability of navigation in complex urban environments through in-depth exploitation of multi-epoch observation redundancy and the reasonable modeling of pedestrian motion patterns. The outcomes of this research provide higher-quality and smoother trajectory data support for critical applications such as urban mobile health monitoring and even emergency response scenarios.

To enhance vehicle trajectory optimization at the positioning layer, this research pioneered the tightly-coupled integration of Google Earth road information with raw GNSS observations within a factor graph framework. By innovatively incorporating lane-line spatial constraint priors and adaptive switch-variable factors, the lateral vehicle positioning accuracy was significantly improved to 3 meters, representing an accuracy enhancement of up to 41% compared to a standalone FGO GNSS solution. This study not only unveils the substantial potential of factor graph optimization and map prior information for enhancing urban positioning performance but, more importantly, effectively addresses the lane selection challenge in multi-lane scenarios through the implementation of switch-variable factors, thereby improving the system's usability and intelligence in practical engineering applications.

In urban environments, both pedestrian navigation and autonomous vehicle localization heavily rely on the geospatial information provided by high-precision maps. Specifically, high-precision maps furnish detailed indoor and outdoor environmental context for pedestrians, enabling seamless navigation and context-aware services. For vehicles, they serve as the foundational data layer for lane-level accurate positioning, intelligent route planning, and environmental perception and decision-making. However, the persistent “cost-accuracy” dilemma in high-precision map production remains a significant bottleneck in urban digital infrastructure development, severely hindering their large-scale deployment and real-time dynamic updates, and ultimately limiting the widespread realization of numerous smart city applications that depend on high-precision maps. Prior Factor Graph Optimization (FGO) based GNSS positioning frameworks have often fallen short of fully leveraging higher-accuracy carrier-phase observations and rarely integrated Inertial Measurement Unit (IMU) pre-integration techniques. Consequently, their positioning performance in complex urban environments often proves insufficient to provide a reliable absolute positioning reference for relative positioning sensors such as LiDAR. To overcome these limitations and pave the way for next-generation urban positioning infrastructure, this research innovatively investigates a post-processing framework integrating Real-Time

Kinematic (RTK) technology with IMU pre-integration. We validate the feasibility and effectiveness of a low-cost integrated navigation solution, based on a u-blox F9P high-precision GNSS receiver and a MEMS-IMU, in revolutionizing high-precision map datum construction methods. By developing an RTK/INS tightly-coupled model, integrating C/N0-based adaptive weighting function for pseudorange and carrier-phase observations, and effectively fusing IMU pre-integration information, we achieved a horizontal positioning accuracy of 20 centimeters while rigorously controlling the total equipment cost to under $1000 USD. This foundational-layer technical advancement not only offers a practically viable technical pathway for the low-cost, high-efficiency production and dynamic updating of high-precision maps but, more importantly, establishes a solid technological cornerstone for building next-generation smart city spatial data infrastructure and promoting the advancement of various high-precision positioning applications, including pedestrian navigation and autonomous vehicle localization.

Future research efforts will be dedicated to the in-depth fusion of PPP-RTK and FDE technologies, aiming to create more efficient, reliable, and intelligent high-precision GNSS positioning systems for urban environments. We believe that in-depth exploration and practical validation along these research directions will significantly advance the state-of-the-art in urban GNSS positioning technology, making substantial contributions to building next-generation smart city spatial information infrastructure and fostering the flourishing development of broader urban intelligent applications.

REFERENCES

[1] P. Sakhardande, S. Hanagal, and S. Kulkarni, "Design of disaster management system using IoT based interconnected network with smart city monitoring," in *2016 international conference on internet of things and applications (IOTA)*, 2016: IEEE, pp. 185-190.

[2] M. Al-Hader and A. Rodzi, "The smart city infrastructure development & monitoring," *Theoretical and Empirical Researches in Urban Management,* vol. 4, no. 2 (11, pp. 87-94, 2009.

[3] R. Du, P. Santi, M. Xiao, A. V. Vasilakos, and C. Fischione, "The sensable city: A survey on the deployment and management for smart city monitoring," *IEEE Communications Surveys & Tutorials,* vol. 21, no. 2, pp. 1533-1560, 2018.

[4] R. B. Langley, "Rtk gps," *Gps World,* vol. 9, no. 9, pp. 70-76, 1998.

[5] M. T. Elnabwy, M. R. Kaloop, and E. Elbeltagi, "Talkha steel highway bridge monitoring and movement identification using RTK-GPS technique," *Measurement,* vol. 46, no. 10, pp. 4282-4292, 2013.

[6] R. Xi, W. Jiang, X. Meng, H. Chen, and Q. Chen, "Bridge monitoring using BDS-RTK and GPS-RTK techniques," *Measurement,* vol. 120, pp. 128-139, 2018.

[7] Q. Chen *et al.*, "Vertical deformation monitoring of the suspension bridge tower using GNSS: A case study of the forth road bridge in the UK," *Remote Sensing,* vol. 10, no. 3, p. 364, 2018.

[8] R. Xi, Q. He, and X. Meng, "Bridge monitoring using multi-GNSS observations with high cutoff elevations: A case study," *Measurement,* vol. 168, p. 108303, 2021.

[9] D. Toshniwal, N. Chaturvedi, M. Parida, A. Garg, C. Choudhary, and Y. Choudhary, "Application of clustering algorithms for spatio-temporal analysis of urban traffic data," *Transportation Research Procedia,* vol. 48, pp. 1046-1059, 2020.

[10] S.-K. Kim and K. S. Choi, "Automatic Exercise Counting and Calorie Calculation for Outdoor Exercise Equipment in the Park," in *Advances in Human Factors in Sports and Outdoor Recreation: Proceedings of the AHFE 2016 International Conference on Human Factors in Sports and Outdoor Recreation, July 27-31, 2016, Walt Disney World®, Florida, USA*, 2017: Springer, pp. 59-70.

[11] A. Zhan, M. Chang, Y. Chen, and A. Terzis, "Accurate caloric expenditure of bicyclists using cellphones," in *Proceedings of the 10th ACM Conference on Embedded Network Sensor Systems*, 2012, pp. 71-84.

[12] P. McGetrick and D. Hester, "Implementation of a drive-by monitoring system for transport infrastructure utilising GNSS," in *Civil Engineering Research in Ireland Conference 2016*, 2016, p. 161.

[13] P. McGetrick, D. Hester, and S. Taylor, "Implementation of a drive-by monitoring system for transport infrastructure utilising smartphone technology and GNSS," *Journal of Civil Structural Health Monitoring,* vol. 7, pp. 175-189, 2017.

[14] B. Santos, P. G. Almeida, and L. Maganinho, "Data Collection Methodology to Assess Road Pavement Condition Using GNSS, Video Image and GIS," in *IOP Conference Series: Materials Science and Engineering*, 2019, vol. 603, no. 4: IOP Publishing, p. 042083.

[15] Z. Bao, S. Hossain, H. Lang, and X. Lin, "A review of high-definition map creation methods for autonomous driving," *Engineering Applications of Artificial Intelligence,* vol. 122, p. 106125, 2023.

[16] K. Kim, S. Cho, and W. Chung, "HD map update for autonomous driving with crowdsourced data," *IEEE Robotics and Automation Letters,* vol. 6, no. 2, pp. 1895-1901, 2021.

[17] C. Dannheim, M. Maeder, A. Dratva, M. Raffero, S. Neumeier, and C. Icking, "A cost-effective solution for HD Maps creation," in *AmE 2017-Automotive meets Electronics; 8th GMM-Symposium*, 2017: VDE, pp. 1-5.

[18] H. Zhang, C. Qian, W. Li, B. Li, and H. Liu, "Tightly coupled integration of vector HD map, LiDAR, GNSS, and INS for precise vehicle navigation in GNSS-challenging environment," *Geo-Spatial Information Science,* pp. 1-18, 2024.

[19] W. Wen, G. Zhang, and L.-T. Hsu, "Correcting GNSS NLOS by 3D LiDAR and building height," in *Proceedings of the 31st International Technical Meeting of the Satellite Division of The Institute of Navigation (ION GNSS+ 2018)*, 2018, pp. 3156-3168.

[20] K. Jo, C. Kim, and M. Sunwoo, "Simultaneous localization and map change update for the high definition map-based autonomous driving car," *Sensors,* vol. 18, no. 9, p. 3145, 2018.

[21] P. D. Groves, "Principles of GNSS, inertial, and multisensor integrated navigation systems, [Book review]," *IEEE Aerospace and Electronic Systems Magazine,* vol. 30, no. 2, pp. 26-27, 2015.

[22] P. D. Groves, Z. Jiang, M. Rudi, and P. Strode, "A portfolio approach to NLOS and multipath mitigation in dense urban areas," 2013: The Institute of Navigation.

[23] L.-T. Hsu, Y. Gu, and S. Kamijo, "NLOS correction/exclusion for GNSS measurement using RAIM and city building models," *Sensors,* vol. 15, no. 7, pp. 17329-17349, 2015.

[24] W. W. Wen, G. Zhang, and L.-T. Hsu, "GNSS NLOS exclusion based on dynamic object detection using LiDAR point cloud," *IEEE transactions on intelligent transportation systems,* vol. 22, no. 2, pp. 853-862, 2019.

[25] T. Suzuki and N. Kubo, "Correcting GNSS multipath errors using a 3D surface model and particle filter," in *Proceedings of the 26th International Technical Meeting of the Satellite Division of The Institute of Navigation (ION GNSS+ 2013)*, 2013, pp. 1583-1595.

[26] N. Sünderhauf and P. Protzel, "Towards robust graphical models for GNSS-based localization in urban environments," in *International Multi-Conference on Systems, Signals & Devices*, 2012: IEEE, pp. 1-6.

[27] T. D. Barfoot, *State estimation for robotics*. Cambridge University Press, 2017.

[28] W. Wen, T. Pfeifer, X. Bai, and L.-T. Hsu, "Factor graph optimization for GNSS/INS integration: A comparison with the extended Kalman filter," *NAVIGATION: Journal of the Institute of Navigation,* vol. 68, no. 2, pp. 315-331, 2021.

[29] T. Pfeifer and P. Protzel, "Expectation-maximization for adaptive mixture models in graph optimization," in *2019 International Conference on Robotics and Automation (ICRA)*, 2019: IEEE, pp. 3151-3157.

[30] T. Pfeifer and P. Protzel, "Robust sensor fusion with self-tuning mixture models," in *2018 IEEE/RSJ International Conference on Intelligent Robots and Systems (IROS)*, 2018: IEEE, pp. 3678-3685.

[31] T. Pfeifer, S. Lange, and P. Protzel, "Dynamic Covariance Estimation—A parameter free approach to robust Sensor Fusion," in *2017 IEEE International Conference on Multisensor Fusion and Integration for Intelligent Systems (MFI)*, 2017: IEEE, pp. 359-365.

[32] W. Wen and L.-T. Hsu, "Towards robust GNSS positioning and Real-time kinematic using factor graph optimization," in *2021 IEEE International Conference on Robotics and Automation (ICRA)*, 2021: IEEE, pp. 5884-5890.

[33] T. Takasu and A. Yasuda, "Development of the low-cost RTK-GPS receiver with an open source program package RTKLIB," in *International symposium on GPS/GNSS*, 2009, vol. 1: International Convention Center Jeju Korea.
[34] T. Suzuki, "First place award winner of the smartphone decimeter challenge: global optimization of position and velocity by factor graph optimization," in *Proceedings of the 34th International Technical Meeting of the Satellite Division of The Institute of Navigation (ION GNSS+ 2021)*, 2021, pp. 2974-2985.
[35] T. Suzuki, "1st Place Winner of the Smartphone Decimeter Challenge: Two-Step Optimization of Velocity and Position Using Smartphone's Carrier Phase Observations," in *Proceedings of the 35th International Technical Meeting of the Satellite Division of The Institute of Navigation (ION GNSS+ 2022)*, 2022, pp. 2276-2286.
[36] N. Sünderhauf and P. Protzel, "Switchable constraints for robust pose graph SLAM," in *2012 IEEE/RSJ International Conference on Intelligent Robots and Systems*, 2012: IEEE, pp. 1879-1884.
[37] Y. Li *et al.*, "Toward Location-Enabled IoT (LE-IoT): IoT Positioning Techniques, Error Sources, and Error Mitigation," *IEEE Internet of Things Journal,* vol. 8, no. 6, pp. 4035-4062, 2021, doi: 10.1109/JIOT.2020.3019199.
[38] R. Sun *et al.*, "Improving GPS Code Phase Positioning Accuracy in Urban Environments Using Machine Learning," *IEEE Internet of Things Journal,* vol. 8, no. 8, pp. 7065-7078, 2021, doi: 10.1109/JIOT.2020.3037074.
[39] P. Kelly, M. Murphy, and N. Mutrie, "The health benefits of walking," in *Walking*, vol. 9: Emerald Publishing Limited, 2017, pp. 61-79.
[40] P. Biernacki, "Software Correction of Speed Measurement Determined by Phone GNSS Modules in Applications for Runners," *Sensors,* vol. 23, no. 5, p. 2678, 2023.
[41] V. Capuano, L. Xu, and J. Estrada Benavides, "Smartphone MEMS Accelerometer and Gyroscope Measurement Errors: Laboratory Testing and Analysis of the Effects on Positioning Performance," *Sensors,* vol. 23, no. 17, p. 7609, 2023.
[42] R. Chen, W. Chen, X. Chen, X. Zhang, and Y. Chen, "Sensing strides using EMG signal for pedestrian navigation," *GPS solutions,* vol. 15, pp. 161-170, 2011.
[43] M. Basso, A. Martinelli, S. Morosi, and F. Sera, "A real-time GNSS/PDR navigation system for mobile devices," *Remote Sensing,* vol. 13, no. 8, p. 1567, 2021.
[44] S. Beauregard and H. Haas, "Pedestrian dead reckoning: A basis for personal positioning," in *Proceedings of the 3rd Workshop on Positioning, Navigation and Communication*, 2006, pp. 27-35.
[45] U. Steinhoff and B. Schiele, "Dead reckoning from the pocket-an experimental study," in *2010 IEEE international conference on pervasive computing and communications (PerCom)*, 2010: IEEE, pp. 162-170.
[46] Q. Wang *et al.*, "Pedestrian Dead Reckoning Based on Walking Pattern Recognition and Online Magnetic Fingerprint Trajectory Calibration," *IEEE Internet of Things Journal,* vol. 8, no. 3, pp. 2011-2026, 2021, doi: 10.1109/JIOT.2020.3016146.
[47] D. Yan, C. Shi, T. Li, and Y. Li, "FlexPDR: Fully Flexible Pedestrian Dead Reckoning Using Online Multimode Recognition and Time-Series Decomposition," *IEEE Internet of Things Journal,* vol. 9, no. 16, pp. 15240-15254, 2022, doi: 10.1109/JIOT.2022.3147473.
[48] C. Chen, P. Zhao, C. X. Lu, W. Wang, A. Markham, and N. Trigoni, "Deep-Learning-Based Pedestrian Inertial Navigation: Methods, Data Set, and On-Device Inference," *IEEE Internet of Things Journal,* vol. 7, no. 5, pp. 4431-4441, 2020, doi: 10.1109/JIOT.2020.2966773.

[49] W. Chen, R. Chen, Y. Chen, H. Kuusniemi, and J. Wang, "An effective Pedestrian Dead Reckoning algorithm using a unified heading error model," in *IEEE/ION Position, Location and Navigation Symposium*, 4-6 May 2010 2010, pp. 340-347, doi: 10.1109/PLANS.2010.5507300.
[50] W. Kang and Y. Han, "SmartPDR: Smartphone-based pedestrian dead reckoning for indoor localization," *IEEE Sensors journal,* vol. 15, no. 5, pp. 2906-2916, 2014.
[51] J. Kuang, X. Niu, and X. Chen, "Robust pedestrian dead reckoning based on MEMS-IMU for smartphones," *Sensors,* vol. 18, no. 5, p. 1391, 2018.
[52] S. Y. Cho and C. G. Park, "Threshold-less zero-velocity detection algorithm for pedestrian dead reckoning," in *2019 European Navigation Conference (ENC)*, 2019: IEEE, pp. 1-5.
[53] F. Zhu, X. Tao, W. Liu, X. Shi, F. Wang, and X. Zhang, "Walker: Continuous and precise navigation by fusing GNSS and MEMS in smartphone chipsets for pedestrians," *Remote sensing,* vol. 11, no. 2, p. 139, 2019.
[54] J. Ye, Y. Li, H. Luo, J. Wang, W. Chen, and Q. Zhang, "Hybrid urban canyon pedestrian navigation scheme combined PDR, GNSS and beacon based on smartphone," *Remote Sensing,* vol. 11, no. 18, p. 2174, 2019.
[55] R. Harle, "A survey of indoor inertial positioning systems for pedestrians," *IEEE Communications Surveys & Tutorials,* vol. 15, no. 3, pp. 1281-1293, 2013.
[56] C. Wei *et al.*, "An integrated GPS and multi-sensor pedestrian positioning system for 3D urban navigation," in *2009 Joint Urban Remote Sensing Event*, 20-22 May 2009 2009, pp. 1-6, doi: 10.1109/URS.2009.5137690.
[57] A. Rehman, H. Shahid, M. A. Afzal, and H. M. A. Bhatti, "Accurate and Direct GNSS/PDR Integration Using Extended Kalman Filter for Pedestrian Smartphone Navigation," *Gyroscopy and Navigation,* vol. 11, no. 2, pp. 124-137, 2020/04/01 2020, doi: 10.1134/S2075108720020054.
[58] C. Jiang *et al.*, "Smartphone PDR/GNSS Integration via Factor Graph Optimization for Pedestrian Navigation," *IEEE Transactions on Instrumentation and Measurement,* vol. 71, pp. 1-12, 2022.
[59] A. Angrisano, M. Vultaggio, S. Gaglione, and N. Crocetto, "Pedestrian localization with PDR supplemented by GNSS," in *2019 European Navigation Conference (ENC)*, 2019: IEEE, pp. 1-6.
[60] T. Dózsa, J. Radó, J. Volk, Á. Kisari, A. Soumelidis, and P. Kovács, "Road abnormality detection using piezoresistive force sensors and adaptive signal models," *IEEE Transactions on Instrumentation and Measurement,* vol. 71, pp. 1-11, 2022.
[61] A. S. El-Wakeel, J. Li, A. Noureldin, H. S. Hassanein, and N. Zorba, "Towards a Practical Crowdsensing System for Road Surface Conditions Monitoring," *IEEE Internet of Things Journal,* vol. 5, no. 6, pp. 4672-4685, 2018, doi: 10.1109/JIOT.2018.2807408.
[62] X. Huang, D. Wen, J. Li, and R. Qin, "Multi-level monitoring of subtle urban changes for the megacities of China using high-resolution multi-view satellite imagery," *Remote sensing of environment,* vol. 196, pp. 56-75, 2017.
[63] T. W. HOUSE. "Fact Sheet: The Bipartisan Infrastructure Deal." https://www.whitehouse.gov/briefing-room/statements-releases/2021/11/06/fact-sheet-the-bipartisan-infrastructure-deal/#:~:text=The%20legislation%20will%20reauthorize%20surface,and%20support%20major%2C%20transformational%20projects. (accessed.
[64] M. o. T. o. t. P. s. R. o. China. "Notification of the Ministry of Transport on the Issuance of the '14th Five-Year' Highway Maintenance Management Development

Outline." https://xxgk.mot.gov.cn/2020/jigou/glj/202204/t20220426_3652905.html (accessed.
[65] B. V. o. N. Department for Transport. "Funding to fix equivalent of 10 million potholes allocated to local authorities." https://www.gov.uk/government/news/funding-to-fix-equivalent-of-10-million-potholes-allocated-to-local-authorities (accessed.
[66] H. D. o. H. K. S. A. Region. "Road Resurfacing Works Completed in Past 3 Years." https://www.hyd.gov.hk/en/our_services/road_resurfacing_works/works_completed.html (accessed.
[67] A. Gharaibeh *et al.*, "Smart cities: A survey on data management, security, and enabling technologies," *IEEE Communications Surveys & Tutorials,* vol. 19, no. 4, pp. 2456-2501, 2017.
[68] X. Bai, W. Wen, and L.-T. Hsu, "Degeneration-aware outlier mitigation for visual inertial integrated navigation system in urban canyons," *IEEE Transactions on Instrumentation and Measurement,* vol. 70, pp. 1-15, 2021.
[69] Q. Li and S. Ren, "A Real-Time Visual Inspection System for Discrete Surface Defects of Rail Heads," *IEEE Transactions on Instrumentation and Measurement,* vol. 61, no. 8, pp. 2189-2199, 2012, doi: 10.1109/TIM.2012.2184959.
[70] G. He, X. Yuan, Y. Zhuang, and H. Hu, "An integrated GNSS/LiDAR-SLAM pose estimation framework for large-scale map building in partially GNSS-denied environments," *IEEE Transactions on Instrumentation and Measurement,* vol. 70, pp. 1-9, 2020.
[71] H. Li, B. Tian, H. Shen, and J. Lu, "An intensity-augmented LiDAR-inertial SLAM for solid-state LiDARs in degenerated environments," *IEEE Transactions on Instrumentation and Measurement,* vol. 71, pp. 1-10, 2022.
[72] P. D. Groves, "Principles of GNSS, inertial, and multisensor integrated navigation systems, 2nd edition [Book review]," *IEEE Aerospace and Electronic Systems Magazine,* vol. 30, no. 2, pp. 26-27, 2015, doi: 10.1109/MAES.2014.14110.
[73] T. Takasu and A. Yasuda, "Development of the low-cost RTK-GPS receiver with an open source program package RTKLIB," in *International symposium on GPS/GNSS*, 2009, vol. 1: International Convention Center Jeju Korea Seogwipo-si, Korea, pp. 1-6.
[74] P. D. Groves, "Shadow Matching: A New GNSS Positioning Technique for Urban Canyons," *Journal of Navigation,* vol. 64, no. 3, pp. 417-430, 2011, doi: 10.1017/S0373463311000087.
[75] L.-T. Hsu, Y. Gu, and S. Kamijo, "3D building model-based pedestrian positioning method using GPS/GLONASS/QZSS and its reliability calculation," *GPS solutions,* vol. 20, no. 3, pp. 413-428, 2016.
[76] Y. Wada, L.-T. Hsu, Y. Gu, and S. Kamijo, "Optimization of 3D building models by GPS measurements," *GPS Solutions,* vol. 21, no. 1, pp. 65-78, 2017/01/01 2017, doi: 10.1007/s10291-015-0504-y.
[77] F. Marchal, J. Hackney, and K. W. Axhausen, "Efficient map matching of large global positioning system data sets: Tests on speed-monitoring experiment in Zürich," *Transportation Research Record,* vol. 1935, no. 1, pp. 93-100, 2005.
[78] C. Scott, "Improved GPS positioning for motor vehicles through map matching," in *Proceedings of the 7th International Technical Meeting of the Satellite Division of the Institute of Navigation (ION GPS 1994)*, 1994, pp. 1391-1400.
[79] F. Gustafsson *et al.*, "Particle filters for positioning, navigation, and tracking," *IEEE Transactions on signal processing,* vol. 50, no. 2, pp. 425-437, 2002.

[80] K. W. Lee, S. Wijesoma, and J. I. Guzmán, "A constrained SLAM approach to robust and accurate localisation of autonomous ground vehicles," *Robotics and Autonomous Systems,* vol. 55, no. 7, pp. 527-540, 2007.
[81] C. Fouque, P. Bonnifait, and D. Bétaille, "Enhancement of global vehicle localization using navigable road maps and dead-reckoning," in *2008 IEEE/ION Position, Location and Navigation Symposium*, 2008: IEEE, pp. 1286-1291.
[82] M. Haklay and P. Weber, "Openstreetmap: User-generated street maps," *IEEE Pervasive computing,* vol. 7, no. 4, pp. 12-18, 2008.
[83] M. Hentschel and B. Wagner, "Autonomous robot navigation based on openstreetmap geodata," in *13th International IEEE Conference on Intelligent Transportation Systems*, 2010: IEEE, pp. 1645-1650.
[84] K. Klipp, A. Kisand, J. Wortmann, and I. Radusch, "Multidimensional In-and outdoor pedestrian tracking using OpenStreetMap data," in *2021 International Conference on Indoor Positioning and Indoor Navigation (IPIN)*, 2021: IEEE, pp. 1-8.
[85] R. J. Lisle, "Google Earth: a new geological resource," *Geology today,* vol. 22, no. 1, pp. 29-32, 2006.
[86] Z. Hu, P. K. Munneke, S. Lhermitte, M. Dirscherl, C. Ji, and M. van den Broeke, "FABIAN: A daily product of Fractional Austral-summer Blue Ice over ANtarctica during 2000–2021 based on MODIS imagery using Google Earth Engine," *Remote Sensing of Environment,* vol. 280, p. 113202, 2022.
[87] S. Chen *et al.*, "Monitoring temperate forest degradation on Google Earth Engine using Landsat time series analysis," *Remote Sensing of Environment,* vol. 265, p. 112648, 2021.
[88] L. Parente, V. Mesquita, F. Miziara, L. Baumann, and L. Ferreira, "Assessing the pasturelands and livestock dynamics in Brazil, from 1985 to 2017: A novel approach based on high spatial resolution imagery and Google Earth Engine cloud computing," *Remote Sensing of Environment,* vol. 232, p. 111301, 2019.
[89] Y. Choi and A. Nieto, "Optimal haulage routing of off-road dump trucks in construction and mining sites using Google Earth and a modified least-cost path algorithm," *Automation in Construction,* vol. 20, no. 7, pp. 982-997, 2011.
[90] G. Pulighe, V. Baiocchi, and F. Lupia, "Horizontal accuracy assessment of very high resolution Google Earth images in the city of Rome, Italy," *International Journal of Digital Earth,* vol. 9, no. 4, pp. 342-362, 2016.
[91] X. Wang and F. Wang, "The Precision of Google Earth Map Analysis With the Coordinates of IGS Stations," *The International Archives of the Photogrammetry, Remote Sensing and Spatial Information Sciences,* vol. 42, pp. 1053-1056, 2020.
[92] J. Li and M. Wu, "The improvement of positioning accuracy with weighted least square based on SNR," in *2009 5th International Conference on Wireless Communications, Networking and Mobile Computing*, 2009: IEEE, pp. 1-4.
[93] L. Li, J. Zhong, and M. Zhao, "Doppler-aided GNSS position estimation with weighted least squares," *IEEE transactions on vehicular technology,* vol. 60, no. 8, pp. 3615-3624, 2011.
[94] M. S. Grewal, A. P. Andrews, and C. G. Bartone, "Kalman filtering," 2020.
[95] M. G. Petovello, K. O'Keefe, G. Lachapelle, and M. E. Cannon, "Consideration of time-correlated errors in a Kalman filter applicable to GNSS," *Journal of Geodesy,* vol. 83, pp. 51-56, 2009.
[96] F. S. T. Van Diggelen, *A-gps: Assisted gps, gnss, and sbas*. Artech house, 2009.
[97] G. Chen, *Approximate kalman filtering*. World scientific, 1993.
[98] P. Chao, Y. Xu, W. Hua, and X. Zhou, "A survey on map-matching algorithms," in *Databases Theory and Applications: 31st Australasian Database Conference, ADC*

2020, Melbourne, VIC, Australia, February 3–7, 2020, Proceedings 31, 2020: Springer, pp. 121-133.
[99] M. A. Quddus, W. Y. Ochieng, and R. B. Noland, "Current map-matching algorithms for transport applications: State-of-the art and future research directions," *Transportation research part c: Emerging technologies,* vol. 15, no. 5, pp. 312-328, 2007.
[100] M. Hashemi and H. A. Karimi, "A critical review of real-time map-matching algorithms: Current issues and future directions," *Computers, Environment and Urban Systems,* vol. 48, pp. 153-165, 2014.
[101] J. Kim, "Node based map matching algorithm for car navigation system," in *International symposium on automotive technology & automation (29th: 1996: Florence, Italy). Global deployment of advanced transportation telematics/ITS*, 1996.
[102] L. Li, M. Quddus, and L. Zhao, "High accuracy tightly-coupled integrity monitoring algorithm for map-matching," *Transportation Research Part C: Emerging Technologies,* vol. 36, pp. 13-26, 2013.
[103] L.-T. Hsu *et al.*, "Hong Kong UrbanNav: An open-source multisensory dataset for benchmarking urban navigation algorithms," *NAVIGATION: Journal of the Institute of Navigation,* vol. 70, no. 4, 2023.
[104] G. Falco, M. Pini, and G. Marucco, "Loose and tight GNSS/INS integrations: Comparison of performance assessed in real urban scenarios," *Sensors,* vol. 17, no. 2, p. 255, 2017.
[105] G. Falco, M. Campo-Cossío, and A. Puras, "MULTI-GNSS receivers/IMU system aimed at the design of a heading-constrained Tightly-Coupled algorithm," in *2013 International Conference on Localization and GNSS (ICL-GNSS)*, 25-27 June 2013 2013, pp. 1-6, doi: 10.1109/ICL-GNSS.2013.6577263.
[106] K.-W. Chiang, T. T. Duong, and J.-K. Liao, "The Performance Analysis of a Real-Time Integrated INS/GPS Vehicle Navigation System with Abnormal GPS Measurement Elimination," *Sensors,* vol. 13, no. 8, pp. 10599-10622, 2013. [Online]. Available: https://www.mdpi.com/1424-8220/13/8/10599.
[107] G. Gao and G. Lachapelle, "A novel architecture for ultra-tight HSGPS-INS integration," *Positioning,* vol. 1, no. 13, 2008.
[108] Q. Zhang, X. Niu, and C. Shi, "Impact assessment of various IMU error sources on the relative accuracy of the GNSS/INS systems," *IEEE Sensors Journal,* vol. 20, no. 9, pp. 5026-5038, 2020.
[109] W. Wen, T. Pfeifer, X. Bai, and L.-T. Hsu, "Factor graph optimization for GNSS/INS integration: A comparison with the extended Kalman filter," *NAVIGATION, Journal of the Institute of Navigation,* vol. 68, no. 2, pp. 315-331, 2021.
[110] H. Tang, T. Zhang, X. Niu, J. Fan, and J. Liu, "Impact of the earth rotation compensation on MEMS-IMU preintegration of factor graph optimization," *IEEE Sensors Journal,* vol. 22, no. 17, pp. 17194-17204, 2022.
[111] C. Chi, X. Zhang, J. Liu, Y. Sun, Z. Zhang, and X. Zhan, "Gici-lib: A gnss/ins/camera integrated navigation library," *IEEE Robotics and Automation Letters,* 2023.
[112] Y. Liu, S. Li, Q. Fu, Z. Liu, and Q. Zhou, "Analysis of Kalman filter innovation-based GNSS spoofing detection method for INS/GNSS integrated navigation system," *IEEE Sensors Journal,* vol. 19, no. 13, pp. 5167-5178, 2019.
[113] D. Wang, Y. Dong, Z. Li, Q. Li, and J. Wu, "Constrained MEMS-Based GNSS/INS Tightly Coupled System With Robust Kalman Filter for Accurate Land Vehicular Navigation," *IEEE Transactions on Instrumentation and Measurement,* vol. 69, no. 7, pp. 5138-5148, 2020, doi: 10.1109/TIM.2019.2955798.

[114] Y. Zhong, W. Wen, and L.-T. Hsu, "Trajectory smoothing using gnss/pdr integration via factor graph optimization in urban canyons," *IEEE Internet of Things Journal,* 2024.
[115] C. Taylor and J. Gross, "Factor Graphs for Navigation Applications: A Tutorial," *NAVIGATION: Journal of the Institute of Navigation,* vol. 71, no. 3, 2024.
[116] T. Pfeifer, P. Weissig, S. Lange, and P. Protzel, "Robust factor graph optimization-a comparison for sensor fusion applications," in *2016 IEEE 21st International Conference on Emerging Technologies and Factory Automation (ETFA)*, 2016: IEEE, pp. 1-4.
[117] X. Xia, L.-T. Hsu, and W. Wen, "Integrity-constrained factor graph optimization for GNSS positioning," in *2023 IEEE/ION Position, Location and Navigation Symposium (PLANS)*, 2023: IEEE, pp. 414-420.
[118] Y. Zhong, W. Wen, H.-F. Ng, X. Bai, and L.-T. Hsu, "Real-time factor graph optimization aided by graduated non-convexity based outlier mitigation for smartphone decimeter challenge," in *Proceedings of the 35th International Technical Meeting of the Satellite Division of The Institute of Navigation (ION GNSS+ 2022)*, 2022, pp. 2339-2348.
[119] W. Wen, G. Zhang, and L.-T. Hsu, "GNSS outlier mitigation via graduated non-convexity factor graph optimization," *IEEE Transactions on Vehicular Technology,* vol. 71, no. 1, pp. 297-310, 2021.
[120] M. Liu and G. Chang, "Numerically and statistically stable Kalman filter for INS/GNSS integration," *Proceedings of the Institution of Mechanical Engineers, Part G: Journal of Aerospace Engineering,* vol. 230, no. 2, pp. 321-332, 2016.
[121] Z. Berman, "Outliers rejection in Kalman filtering—Some new observations," in *2014 IEEE/ION Position, Location and Navigation Symposium-PLANS 2014*, 2014: IEEE, pp. 1008-1013.
[122] E. Navon and B.-Z. Bobrovsky, "An efficient outlier rejection technique for Kalman filters," *Signal Processing,* vol. 188, p. 108164, 2021.
[123] L.-T. Hsu, H. Tokura, N. Kubo, Y. Gu, and S. Kamijo, "Multiple faulty GNSS measurement exclusion based on consistency check in urban canyons," *IEEE Sensors Journal,* vol. 17, no. 6, pp. 1909-1917, 2017.
[124] J. Wang and J. Wang, "Mitigating the effect of multiple outliers on GNSS navigation with M-estimation schemes," in *IGNSS symposium*, 2007, pp. 4-6.
[125] J. A. Pozo-Pérez, D. Medina, I. Herrera-Pinzón, A. Heßelbarth, and R. Ziebold, "Robust outlier mitigation in multi-constellation GNSS positioning for waterborne applications," in *Proceedings of the 2017 International Technical Meeting of The Institute of Navigation*, 2017, pp. 1330-1343.
[126] X. Xia, W. Wen, and L.-T. Hsu, "Integrity-Constrained Factor Graph Optimization for GNSS Positioning in Urban Canyons," *NAVIGATION: Journal of the Institute of Navigation,* vol. 71, no. 3, 2024.
[127] A. V. Kanhere, S. Gupta, A. Shetty, and G. Gao, "Improving gnss positioning using neural-network-based corrections," *NAVIGATION: Journal of the Institute of Navigation,* vol. 69, no. 4, 2022.
[128] N. Al Bitar, A. Gavrilov, and W. Khalaf, "Artificial intelligence based methods for accuracy improvement of integrated navigation systems during GNSS signal outages: an analytical overview," *Gyroscopy and Navigation,* vol. 11, pp. 41-58, 2020.
[129] P. Xu *et al.*, "Differentiable factor graph optimization with intelligent covariance adaptation for accurate smartphone positioning," in *Proceedings of the 36th International Technical Meeting of the Satellite Division of The Institute of Navigation (ION GNSS+ 2023)*, 2023, pp. 2765-2773.

[130] P. Xu and L.-T. Hsu, "AutoW: Self-Supervision Learning for Weighting Estimation in GNSS Positioning," in *Proceedings of the 37th International Technical Meeting of the Satellite Division of The Institute of Navigation (ION GNSS+ 2024)*, 2024, pp. 2630-2644.
[131] H. Hartinger and F. K. Brunner, "Variances of GPS phase observations: the SIGMA-ε model," *GPS solutions,* vol. 2, pp. 35-43, 1999.
[132] T. Takasu, N. Kubo, and A. Yasuda, "Development, evaluation and application of RTKLIB: A program library for RTK-GPS," in *GPS/GNSS symposium*, 2007, pp. 213-218.
[133] L.-T. Hsu, Y. Gu, Y. Huang, and S. Kamijo, "Urban pedestrian navigation using smartphone-based dead reckoning and 3-D map-aided GNSS," *IEEE Sensors Journal,* vol. 16, no. 5, pp. 1281-1293, 2015.
[134] A. M. Herrera, H. F. Suhandri, E. Realini, M. Reguzzoni, and M. C. de Lacy, "goGPS: open-source MATLAB software," *Gps Solut,* vol. 20, no. 3, pp. 595-603, 2016.
[135] T. Takasu and A. Yasuda, "Development of the low-cost RTK-GPS receiver with an open source program package RTKLIB," in *International symposium on GPS/GNSS*, 2009: International Convention Center Jeju Korea, pp. 4-6.
[136] S. Malkos, "Google to Provide Raw GNSS Measurements: User Location Takes Center Stage in New Android OS," *GPS World,* vol. 27, no. 7, p. 36, 2016.
[137] H. Weinberg, "Using the ADXL202 in pedometer and personal navigation applications," *Analog Devices AN-602 application note,* vol. 2, no. 2, pp. 1-6, 2002.
[138] D. Kamisaka, S. Muramatsu, T. Iwamoto, and H. Yokoyama, "Design and implementation of pedestrian dead reckoning system on a mobile phone," *IEICE transactions on information and systems,* vol. 94, no. 6, pp. 1137-1146, 2011.
[139] H.-F. Ng, G. Zhang, and L.-T. Hsu, "A computation effective range-based 3D mapping aided GNSS with NLOS correction method," *The Journal of Navigation,* vol. 73, no. 6, pp. 1202-1222, 2020.
[140] S. P. Drake, "Converting GPS coordinates [phi, lambda, h] to navigation coordinates (ENU)," 2002.
[141] S. Agarwal and K. Mierle, "Ceres solver," 2012.
[142] J. J. Moré, "The Levenberg-Marquardt algorithm: implementation and theory," in *Numerical analysis*: Springer, 1978, pp. 105-116.
[143] J. Ortiz, M. Pupilli, S. Leutenegger, and A. J. Davison, "Bundle adjustment on a graph processor," in *Proceedings of the IEEE/CVF Conference on Computer Vision and Pattern Recognition*, 2020, pp. 2416-2425.
[144] T. Wübbena, F. Darugna, A. Ito, and J. Wübbena, "Geo++'s Experiments on Android GNSS Raw Data," in *Proceedings of the GNSS Raw Measurements Taskforce Workshop, GSA Headquarters*, 2018.
[145] F. Huang, W. Wen, J. Zhang, and L.-T. Hsu, "Point wise or feature wise? A benchmark comparison of publicly available LiDAR odometry algorithms in urban canyons," *IEEE Intelligent Transportation Systems Magazine,* vol. 14, no. 6, pp. 155-173, 2022.
[146] L. Zhang, H.-F. Ng, G. Zhang, and L.-T. Hsu, "3D Mapping Aided GNSS Positioning Using Doppler Frequency for Urban Areas," in *Proceedings of the 36th International Technical Meeting of the Satellite Division of The Institute of Navigation (ION GNSS+ 2023)*, 2023, pp. 2897-2905.
[147] T. Shan, B. Englot, D. Meyers, W. Wang, C. Ratti, and D. Rus, "LIO-SAM: Tightly-coupled Lidar Inertial Odometry via Smoothing and Mapping," *2020 IEEE/RSJ International Conference on Intelligent Robots and Systems (IROS),* pp. 5135-5142, 2020.

[148] W. Wen, T. Pfeifer, X. Bai, and L.-T. Hsu, "It is time for Factor Graph Optimization for GNSS/INS Integration: Comparison between FGO and EKF," *arXiv preprint arXiv:2004.10572,* 2020.
[149] P. Xie and M. G. Petovello, "Measuring GNSS multipath distributions in urban canyon environments," *IEEE Transactions on Instrumentation and Measurement,* vol. 64, no. 2, pp. 366-377, 2014.
[150] W. Wen and L.-T. Hsu, "Factor Graph Optimization for Tightly-Coupled GNSS Pseudorange/Doppler/Carrier Phase/INS Integration: Performance in Urban Canyons of Hong Kong," in *Proceedings of the 35th International Technical Meeting of the Satellite Division of The Institute of Navigation (ION GNSS+ 2022)*, 2022, pp. 2178-2189.
[151] S. Das, R. Watson, and J. Gross, "Review of Factor Graphs for Robust GNSS Applications," *arXiv preprint arXiv:2112.07794,* 2021.
[152] A. M. Herrera, H. F. Suhandri, E. Realini, M. Reguzzoni, and M. de Lacy, "goGPS: open-source MATLAB software," *GPS solutions,* vol. 20, no. 3, pp. 595-603, 2016.
[153] N. Sünderhauf, M. Obst, S. Lange, G. Wanielik, and P. Protzel, "Switchable constraints and incremental smoothing for online mitigation of non-line-of-sight and multipath effects," in *2013 IEEE Intelligent Vehicles Symposium (IV)*, 2013: IEEE, pp. 262-268.
[154] J. J. Moré, "The Levenberg-Marquardt algorithm: implementation and theory," in *Numerical Analysis: Proceedings of the Biennial Conference Held at Dundee, June 28–July 1, 1977*, 2006: Springer, pp. 105-116.
[155] L.-T. Hsu *et al.*, "UrbanNav: An open-sourced multisensory dataset for benchmarking positioning algorithms designed for urban areas," in *Proceedings of the 34th International Technical Meeting of the Satellite Division of The Institute of Navigation (ION GNSS+ 2021)*, 2021, pp. 226-256.
[156] H. F. Ng, G. Zhang, Y. Luo, and L. T. Hsu, "Urban positioning: 3D mapping-aided GNSS using dual-frequency pseudorange measurements from smartphones," *Navigation,* vol. 68, no. 4, pp. 727-749, 2021.
[157] T. Lupton and S. Sukkarieh, "Visual-Inertial-Aided Navigation for High-Dynamic Motion in Built Environments Without Initial Conditions," *IEEE Transactions on Robotics,* vol. 28, no. 1, pp. 61-76, 2012, doi: 10.1109/TRO.2011.2170332.
[158] C. Forster, L. Carlone, F. Dellaert, and D. Scaramuzza, "IMU Preintegration on Manifold for Efficient Visual-Inertial Maximum-a-Posteriori Estimation," in *Robotics: Science and Systems*, 2015.
[159] S. Agarwal and K. Mierle, "Ceres solver: Tutorial & reference," *Google Inc,* vol. 2, no. 72, p. 8, 2012.
[160] R. Hu, P. Xu, Y. Zhong, and W. Wen, "pyrtklib: An open-source package for tightly coupled deep learning and GNSS integration for positioning in urban canyons," *arXiv preprint arXiv:2409.12996,* 2024